Epistasis and pleiotropy in viral protein evolution

Timothy Yu

A dissertation
submitted in partial fulfillment of the
requirements for the degree of

Doctor of Philosophy

University of Washington
2025

Reading Committee:
Jesse D. Bloom, Chair
Frederick A. Matsen IV
Trevor Bedford

Program Authorized to Offer Degree:
Molecular and Cellular Biology

University of Washington

Abstract

Epistasis and pleiotropy in viral protein evolution

Timothy Yu

Chair of the Supervisory Committee:
Jesse D. Bloom
Fred Hutchinson Cancer Center

Viruses evolve under Darwinian selection, and forecasting their evolution requires understanding which mutations confer fitness advantages. Over the past decade, advances in high-throughput experiments have made it possible to measure the phenotypic effects of all mutations to key viral proteins. Yet we continue to fall short when predicting which viral mutations will rise in frequency.

The main problem is that the effect of a mutation is not fixed—it depends on the genetic background in which it occurs and on an immune context that is often unknown and dynamic. A mutation that is deleterious in one background may become tolerated in another. A mutation that benefits one phenotype but harms another can create conflicts that constrain selection. These phenomena, known as epistasis and pleiotropy, complicate efforts to make accurate viral forecasts.

In chapter 2, we examine how viral mutations combine to escape antibodies in human sera. We introduce a simple biophysical model that explains how the effect of a mutation on antibody escape depends on epistatic interactions with other mutations. We then show how these mutation effects can be inferred directly from deep mutational scanning datasets.

In chapter 3, we investigate how pleiotropy constrains viral protein evolution. We use deep mutational scanning to measure the effects of mutations to human influenza virus hemagglutinin on three phenotypes: cell entry, acid stability, and serum antibody neutralization. By quantifying mutation effects across multiple phenotypes, we identify viral mutations that are beneficial in one context but deleterious in another, revealing evolutionary trade-offs.

Finally, in chapter 4, we compare the effects of viral mutations to H3, H5, and H7 influenza virus hemagglutinin to explore how mutation effects differ across three sequentially divergent but structurally conserved proteins.

Contents

Acknowledgements

I loved my time as a graduate student. Evolution teaches us that outcomes are contingent. The path a lineage takes depends on the particular mutations that happened along the way. My own path has felt much the same. I am here because of a series of fortunate events—opportunities, mentors, friends, and family. Here, I want to try to acknowledge everyone who made this Wonderful life possible.

Joining Jesse Bloom's lab was the best decision I made in my scientific career. Jesse is so good at so many things. He can troubleshoot experiments, write software packages, and make the most technical concepts easy to understand. Jesse offered me a chance to cultivate my interests in deep mutational scanning and viral evolution in his lab. Not everything was smooth sailing, but I'll always remember Jesse's constant encouragement, the times he'd tell me to "embrace the complexity" in the face of an initially confusing piece of data, and the feelings of joy when that complexity turned out to be a meaningful scientific result. Jesse left me with habits that I will carry for the rest of my career. I promise I will never make a bar graph on a log-scale, keep track of all my plasmids in an organized system, and (try my best to) make modular git commits. I am a better scientist because of Jesse. Thank you for everything.

I could not have asked for a better group of labmates in the Bloom lab. To everyone, past and present, thank you for creating such a welcoming environment. I especially want to shout-out Andrea Loes and Frances Welsh, who taught me everything I know about influenza viruses, and Bernadeta Dadonaite and Caelan Radford, who introduced me to the wondrous world of lentiviruses. Brendan Larsen makes beautiful protein structure figures and helped me get started in ChimeraX. Will Hannon and Andrew Butler are computational wizards who guided me through conda nightmares and always left their office door open for thoughtful discussions. Caroline Kikawa has always been generous, whether it's with her reagents and scientific advice, or with a very particular Pokemon card (Crawdaunt). Jenny Ahn was a fantastic baymate and an even better friend; thank you for always being there to yap and do side quests like design virus-themed stickers or bike around Lake Washington. I am also grateful to Andrea Loes, Teagan McMahon, and Ruby San Pedro for keeping the lab running smoothly. Finally, I sincerely appreciate everyone in the lab who entertained my obsession with the roll combo deal at I Love Sushi and helped turn it into a weekly ritual. It was a privilege to do science alongside you all.

I have been very fortunate to have a committee of incredible and supportive individuals. I was lucky to be able to collaborate with Erick Matsen, one of the most rigorous and kind scientists that I know. To Alison Feder, Trevor Bedford, and Kelly Lee—thank you for your genuine interest in my work, for your suggestions that led to many of the ideas in this thesis, and for your unwavering patience throughout the years.

I am also thankful for my undergraduate mentors. I am particularly indebted to Guillaume Urtecho. Eight years ago, you took me—a clueless first-year—under your wing and gave me a dream opportunity. You taught me molecular biology techniques, encouraged me to learn how to code, and showed me how to write my first paper. When I was uncertain about my path, you were always there to listen. Your mentorship inspired me to pursue a PhD, and I am committed to passing this on to the next generation of scientists like you did for me. I am also grateful to Sri Kosuri, Thomas Vallim, Elizabeth Tarling, Galit Alter, and Jishnu Das, who all graciously invited me into their labs and supported my goals of pursuing a PhD and career in science.

I would not have made it through graduate school without the support of friends. I was lucky to meet Jessie Kulsuptrakul and Cara Chao during our first year in the MCB PhD program, and we've been on many adventures ever since. I want to thank Felix Chen, Michelle Nemeth, and Alfred Tan for the hundreds of rounds of 一百二十分 (the best trick-taking card game) that we played over the years. My crewmates, Roger Cheng and Andy Ha, joined me for countless reps on the basketball court in search of the One Clip. Old friends from college, Grace Bower and Jeremy Shek, still help me troubleshoot cloning issues and always welcomed me back for my annual pilgrimage to Southern California.

So much of who I am comes from my family. My parents, Jie Cheng and Zhengtian Yu, made many sacrifices to ensure I had the best education possible. My dad is an avid collector of books, and my interest in science began when I was a child browsing encyclopedias in his library. My mom has always encouraged me to be a better writer, a skill I used to overlook but have come to value more and more as a scientist. My brother, Felix Yu, is also a PhD candidate, the kind of brilliant that keeps me humble, and the best little brother I could ask for. Even though we are all thousands of miles apart, I have always felt your love and support. I am sorry I have been away for so long, and I cannot wait to be closer to you all soon.

Finally, my deepest gratitude goes to Winnie Liu. Above all things, I am thankful that we met and grew into each other's lives. You inspire me to aim for new heights and catch me every time I stumble. You have always been on my side, and I will always be on yours. This PhD would not have been possible without your companionship, and I'm excited for what comes next as we waddle into the future together.

Chapter 1

Introduction

Biologists have long been fascinated by evolution because it blends law and luck. Evolution proceeds by systematic selection for traits that improve fitness, while its ingredients are random mutations tossed in by chance. The remarkable outcome of this interplay is the extraordinary diversity of life on Earth. But why do we see *these* outcomes, and what paths did evolution never take?

In 1932, Sewall Wright introduced the fitness landscape, a metaphor for visualizing the relationship between an organism's genotype and its fitness [178]. Picture a mountain range, with peaks corresponding to genotypes of higher fitness and valleys to lower fitness. Wright envisioned populations climbing this terrain as mutations arise and selection nudges them uphill. While abstract, the fitness landscape has proven to be a useful framework for thinking about adaptation and the structure of sequence space, clarifying which evolutionary paths are accessible and which are not.

The fitness landscape invites a tempting question. If we can chart the landscape, or even just the neighborhood around a genotype, can we predict how evolution will play out? Early work that empirically measured fitness landscapes showed that adaptation often proceeds in single mutation steps and that only a small fraction of the many possible routes actually lead to higher fitness [102, 172]. Given the astronomical size of genotype space, this sparsity is encouraging for prediction. Yet these studies also found that landscapes are rugged: some genotypes are local peaks separated by valleys, where intermediate forms are less fit. Such topography can emerge when a mutation that is harmful on its own becomes helpful only alongside another. A classic example comes from the β-lactamase enzyme in bacteria [172]. One mutation enhances hydrolysis of the antibiotic, cefotaxime, but at the cost of thermodynamic stability. Another mutation improves stability, but at the cost of reduced hydrolysis. Separately, each mutation lowers overall fitness. But in combination, the pair raises fitness in the presence of cefotaxime. Therefore, to predict evolution, we must understand how mutations interact with one another (epistasis), which phenotypes each mutation perturbs (pleiotropy), and how those phenotypes together determine fitness.

In this thesis, we examine how epistasis and pleiotropy manifest in viral evolution. Viruses are an

ideal model for studying basic questions about evolutionary biology. Viral evolution is rapid: they mutate frequently because of error-prone polymerases, reach large population sizes, and their entry proteins are typically under fierce selection by immune pressure. Large-scale sequencing of viral isolates makes it possible to track the fate of mutations, enabling direct comparison between what unfolds in nature and what we observe in the laboratory. Additionally, viral evolution has been notoriously difficult to predict. If we could predict it, we could make better public health decisions like selecting matched vaccines, guiding surveillance efforts, and anticipating antiviral resistance before it spreads.

This chapter opens with a review of epistasis and pleiotropy that is tailored towards our study of viral protein evolution. We then introduce influenza viruses, the primary model in this thesis, and outline why they are well-suited for studying evolutionary constraints. Next, we describe deep mutational scanning, a high-throughput method for mapping local mutational effects. Finally, we preview how the work in this thesis builds on these foundations to clarify the roles that epistasis and pleiotropy play in shaping viral protein evolution.

1.1 Epistasis

The simplest definition of epistasis is a deviation from the expectation that mutational effects combine independently [154]. On an additive scale for the phenotype of interest, epistasis is present when:

$$\beta_{AB} \neq \beta_A + \beta_B \tag{1.1}$$

where β_A and β_B are the effects of single mutations A and B, and β_{AB} is the effect of the double mutant. This non-additivity introduces a layer of complexity that greatly challenges our ability to predict evolution.

Before proceeding, it's important to clarify what we mean by an "effect." We can define it in either reference-based or reference-free terms. Reference-based effects are relative to a chosen wildtype genotype (e.g., the change in a phenotype when introducing mutation A into the wildtype background). Reference-free effects describe a mutation's contribution independent of any particular genotype (e.g. the average change in a phenotype when introducing mutation A across backgrounds). Both have their place. Reference-based models make more sense when estimating mutational effects in the local neighborhood of a particular genotype, but they become intractable as the number of mutations away from the wildtype increases. Reference-free models do not suffer from this intractability and are better suited for analyzing the global genetic architecture, but they blur the effect of a mutation in a particular background [129, 122]. In this thesis, we analyze experimental data where genotypes are either dominated by single mutants or are, on average, 3-4 mutations away from a wildtype background. Therefore, we exclusively use reference-

based models, which we will review here.

1.1.1 Linear interaction model

Before we model epistasis, let's first consider a model that does not include epistasis. Let a variant v be represented by a binary vector $b^{(v)} \in \{0,1\}^M$, where $b_i^{(v)} = 1$ if variant v carries mutation i relative to wildtype and 0 otherwise. We assign each mutation an effect β_i, and we denote the wildtype baseline effect by β_0. For the phenotype p, the additive (no epistasis) model that relates genotype to phenotype is:

$$p_v = \beta_0 + \sum_{i=1}^{M} \beta_i \, b_i^{(v)} \tag{1.2}$$

Epistasis can be incorporated into Eq. 1.2 by adding interaction terms that capture the extra effect of carrying combinations of mutations beyond the sum of their individual effects:

$$p_v = \beta_0 + \sum_{i} \beta_i \, b_i^{(v)} + \sum_{i<j} \beta_{ij} \, b_i^{(v)} b_j^{(v)} + \sum_{i<j<k} \beta_{ijk} \, b_i^{(v)} b_j^{(v)} b_k^{(v)} + \cdots \tag{1.3}$$

For example, the pairwise interaction term β_{ij} quantifies how much the combination of mutations i and j deviates from their additive expectation $\beta_i + \beta_j$. Higher-order terms (e.g., β_{ijk}) quantify the remaining deviation that cannot be explained by any lower-order terms among those mutations.

The type of epistasis can be classified by these interaction terms. $\beta_{ij} > 0$ indicates positive epistasis, when the combination of mutations exceeds the additive expectation. $\beta_{ij} < 0$ indicates negative epistasis, when the combination falls short of the additive expectation. The most dramatic case is sign epistasis, where the presence of one mutation flips the sign of another mutation's net effect. Mathematically, this occurs when $(\beta_i)\left(\beta_i + \beta_{ij}\right) < 0$. In the more extreme case called reciprocal sign epistasis, both mutations flip each other's sign. Mathematically, this occurs when $(\beta_i)\left(\beta_i + \beta_{ij}\right) < 0$ and $\left(\beta_j\right)\left(\beta_j + \beta_{ij}\right) < 0$.

While these interaction terms are easy to interpret, their number explodes as the set of measured mutations grows. A typical viral protein is encoded by 500 amino acids. That means there are $500 \times 19 = 9500$ possible individual mutation effect terms. The number of possible pairwise interaction terms is $\binom{9500}{2}$, which is ~45 million, and the number of possible third-order terms is $\binom{9500}{3}$, which is ~1.4×10^{11}. Not only does it become computationally prohibitive to fit such a colossal parameter set, it is also experimentally infeasible to measure at scale, even with state-of-the-art high-throughput methods. In scenarios where it is possible to experimentally measure higher-order interactions (e.g. by targeting a limited subset of sites or mutations), interpretability can be improved by encouraging sparsity [112, 113, 126, 127]. For

example, interaction terms above a certain order may be ignored or regularization can be used to penalize small interaction terms towards 0.

1.1.2 Global epistasis model

How can we capture epistasis without an explosive set of parameters in Eq. 1.3? One solution is the global epistasis model [121]. The simplicity arises from an assumption that single mutations act additively on an underlying latent phenotype, and this latent phenotype is nonlinearly related to an observed phenotype. Therefore, this model contains the same number of mutation effect parameters as the additive (no epistasis) model, but can still capture the essence of context-dependent effects like saturation and diminishing returns within the nonlinearity that maps the latent to observed phenotype. The latent phenotype (ϕ_v) is expressed as:

$$\phi_v = \beta_0 + \sum_{i=1}^{M} \beta_i \, b_i^{(v)} \tag{1.4}$$

and the observed phenotype (p_v) is defined as:

$$p_v = g\left(\phi_v\right) \tag{1.5}$$

where $g(.)$ is typically a flexible, monotonic spline function that resembles a sigmoid. Note that the latent phenotype ϕ_v can also include pairwise terms. In practice, models like Eq. 1.3 without a nonlinearity can inflate the number of pairwise interactions, whereas models with a nonlinearity like Eq. 1.5 need far fewer, making the remaining pairwise effects more likely to be genuine [179].

Global epistasis models have proven useful for analyzing data from deep mutational scanning of viral entry proteins [179, 27, 62]. Their limitation, however, is interpretability of the latent phenotype. A model may fit the data well, but it is impossible to tell if the latent phenotype corresponds to a single trait (e.g., folding free energy) or to a mixture of traits [121].

1.2 Pleiotropy

Pleiotropy, as defined in this thesis, is the simple yet profound idea that a single mutation can affect multiple, distinct phenotypes [155]. Whereas epistasis concerns how a mutation's effect on a given phenotype depends on genetic background, pleiotropy concerns the range of distinct phenotypes that a single mutation can influence. How pleiotropy shapes adaptation has captivated evolutionary biologists for the past century. In 1930, Fisher introduced a helpful analogy for understanding the core problem [42, 168].

Picture a microscope that has several knobs that need to be tuned together for a sharp image. If there are only one or two knobs, there's a good chance that if you randomly turn each of the knobs it will improve focus. But as the number of knobs grows, blind tweaking is far less likely to succeed. This was the intuition behind Fisher's geometric model. The microscope is an organism, the knobs are phenotypes, and the random turns of each knob are the effects of a random mutation on each phenotype.

Based on Fisher's model, pleiotropy imposes a cost of complexity: as a mutation perturbs more independent phenotypes, the probability that it is beneficial declines and the rate of adaptation is expected to slow [119]. This constraint can explain why genomes appear modular [167]. By partitioning genes into functional modules that each affect a limited set of traits, organisms maximize their chances of overcoming potential harm from pleiotropy and mitigate the cost of complexity. But pleiotropy, irrespective of modularity, is always present—even the most specialized protein must both fold stably and perform its function (e.g., catalysis). Predicting evolution therefore requires understanding the spectrum of a mutation's effects across the phenotypes that it influences. The trouble is, we rarely know what or how many "knobs" a mutation actually turns. Unobserved phenotypes could introduce hidden trade-offs, making evolution difficult to anticipate.

1.2.1 Pleiotropic conflict

We say a mutation is under a pleiotropic conflict (also known as antagonistic pleiotropy) when it benefits one phenotype but impairs another, and the net effect is not favored by selection. The mutation discussed earlier that benefits antibiotic resistance but impairs β-lactamase stability is a good example of this [172]. An important question is: to what extent can epistasis alleviate a pleiotropic conflict? Or, in Wrightian terms, does another fitness peak exist, and if so, how distant is it in genotype space? If a pleiotropic mutation's deleterious effect can be alleviated (e.g., by a permissive mutation), then its beneficial effect can be favored by selection and the mutation could rise toward fixation. In the case of the antibiotic resistance mutation, there is another fitness peak and just one permissive mutation is required to reach it. In contrast, other work on the SARS-CoV-2 virus spike protein found that multiple permissive mutations are required to resolve a pleiotropic conflict between immune escape and receptor binding affinity [113]. These examples illustrate how the strength of pleiotropic conflicts can vary, but we are also limited by what we see. Certainly many mutations that have never appeared may be constrained by extremely strong pleiotropic conflicts.

Although pleiotropy is often perceived as a constraint on adaptive evolution, it is worth mentioning that pleiotropy can also be synergistic. Rare pleiotropic mutations that improve multiple phenotypes are the first to be selected in laboratory yeast experiments, before modular mutations that improve single phenotypes [80].

1.3 Influenza virus

Influenza viruses are part of the *Orthomyxoviridae* family and can be divided into four types: Influenza A, B, C, and D. Of these types, only A, B, and C are known to infect humans, and only A has caused human pandemics [165]. In this thesis, we focus exclusively on influenza A viruses, and we will simply refer to them as "influenza viruses" from now on.

1.3.1 Genetics

Influenza viruses are segmented negative-sense RNA viruses [165]. Their genome is ~13.5kb long and contains 8 segments: PB2, PB1, PA, HA, NP, NA, M, and NS. Segmentation is evolutionarily advantageous because it enables reassortment, a genetic recombination event unique to segmented RNA viruses in which co-infection of a host cell by two or more viruses can result in a shuffling of gene segments that produces progeny viruses with novel segment combinations. Genetically diverged HA and NA are classified into subtypes. At the time of writing, 19 HA and 11 NA subtypes have been identified [145, 73]. Two of these combinations, H1N1 and H3N2, currently circulate in humans.

1.3.2 Virion structure

Influenza virus particles are pleomorphic, appearing as filamentous or spherical particles [22]. However, lab-adapted strains are typically spherical [111]. Within the viral envelope, the 8 gene segments are packaged as separate viral ribonucleoprotein complexes (vRNPs), where each segment's RNA is wrapped by nucleoprotein (NP) and associated with an RNA-dependent RNA polymerase composed of PB2, PB1, and PA. The viral envelope is stabilized by the matrix protein (M1), while M2 (produced by alternative splicing) forms a proton ion channel. Finally, the particle is decorated with two surface proteins: hemagglutinin (HA), which mediates receptor binding and membrane fusion during viral entry, and neuraminidase (NA), which facilitates release of progeny viruses [14].

1.3.3 Replication cycle

Viral infection begins when HA binds a host receptor. However, the exact receptor specificity differs among influenza viruses. For the most part, influenza viruses bind sialic acid: human HAs prefer α2,6-linked sialic acids, while avian HAs prefer α2,3-linked sialic acids [107]. However, three HAs (H17, H18, and H19) instead bind major histocompatibility complex (MHC) class II and do not recognize sialic acid at all [75, 52, 73]. H2 posssesses dual specificity for sialic acid and MHC class II [74]. The host range of the virus largely depends on the receptor specficity of the HA.

Receptor bound viruses are internalized into the cell via receptor-mediated endocytosis, placing them into endosomes. The endosome gradually acidifies, and when it reaches a certain pH threshold, HA is triggered to destabilize into a conformation that brings the viral and cell membranes together [16, 147, 10]. The pH threshold varies among HAs. Human HAs tend to be more stable, with fusion pHs of 5.0-5.5, while avian HAs tend to be less stable, with fusion pHs of 5.5-6.0 [50, 136, 163]. After membrane fusion, the viral genetic material is released into the cytoplasm and trafficked into the nucleus via nuclear localization signals on the vRNPs [25].

In the nucleus, the virus must synthesize viral proteins to make new virions and viral RNA to package into those virions. The RNA-dependent RNA polymerase (RdRp) that is carried along the vRNPs performs these functions. To synthesize viral proteins, the RdRp transcribes the negative-sense vRNA into a positive-sense mRNA, performs cap snatching by stealing 5' caps from host mRNAs, and appends them to the viral mRNA so they can be exported out to the cytoplasm and translated. To synthesize the viral RNA, the RdRp transcribes the negative-sense vRNA into complementary RNA intermediates, which are then used as templates by RNA polymerase to synthesize more negative-sense vRNA. Following synthesis, HA, NA, and M2 are specifically trafficked to the cell membrane. When the packaged virions bud off from the cell membrane, HA expressed on the surface of the virions can re-bind to sialic acid present on the same infected cell, preventing the virus from propagating. NA solves this problem by cleaving sialic acid, enabling the virions to free themselves [14]. This process, from infection to new progeny, takes about 6 hours [5].

Note how the viral replication cycle demonstrates that viral proteins are pleiotropic. The HA must maintain its stability during the transmission event, evade the host immune system, bind the host receptor, and coordinate membrane fusion. Any mutation to HA that stands a chance of fixation cannot disrupt any of these phenotypes.

1.3.4 Antigenic shift and drift

Antigenic shifts are a consequence of reassortment, when a novel HA/NA combination is introduced into the human population [165]. The natural reservoir of influenza viruses is thought to be wild waterfowl, though they also circulate in poultry and pigs [117]. When an antigenic shift occurs, people typically have little or no immunity against the novel virus, leading to conditions ripe for a pandemic [84]. Somewhat auspiciously, there have been just four major influenza pandemics in the last century (1918, 1957, 1968, and 2009), indicating that there also exists several barriers to zoonotic transmission [117].

Antigenic drift, on the other hand, is the gradual accumulation of mutations in HA and NA. These two surface proteins are major targets of adaptive immunity and under strong selective pressure to escape antibodies. However, HA is the main target of antibodies and evolves more rapidly than NA [175]. Previ-

ous work has shown that the antigenic evolution of HA appears punctuated [148, 82], though the degree of antigenic stasis is debated [143]. Nonetheless, the HA of human H3N2 influenza virus fixes an average of 3-4 amino acid mutations each year [78, 148, 9, 125]. The consequence of this rapid evolution is that individuals are typically infected with influenza virus once every 5 years [135]. Therefore, annual vaccine updates are necessary to keep pace with these changes.

1.3.5 The forecasting problem

Seasonal influenza viruses causes an estimated 290,000 to 650,000 deaths each year [71]. Every six months, the World Health Organization makes a recommendation for which strains to include in the annual influenza vaccine. However, since vaccine development, manufacturing, and distribution are time consuming, the strains that are selected are a prediction of which strains will circulate at the time of administration [109]. Unfortunately, this prediction remains remarkably poor and as a result, the vaccine is only partially effective. The vaccine efficacy for the most recent influenza season was a meager 48% [139].

One reason why influenza virus evolution is difficult to forecast is because antibody responses vary across the human population, making it unclear how to define the shape of the selective pressure. Much work has revealed that individuals preferentially boost antibody responses against influenza strains that they likely encountered during childhood, a phenomenon known as immune imprinting [32, 46, 44, 94]. Furthermore, susceptibility to influenza viruses both within and across subtypes can differ remarkably between birth cohorts, groups of individuals assumed to share similar histories of imprinting and influenza exposure [63, 186, 96, 49, 99, 177, 2, 55, 48, 56, 3, 57]. While descriptive accounts of imprinting and cohort effects have grown in abundance, we lack a mechanistic model for how antibody specificities change over time in individuals and give rise to these population-level serological differences. However, recent advances in high-throughput sequencing-based assays now make it possible to measure the neutralizing titers of hundreds of diverse human sera against >100 circulating strains [101]. The neutralization measurements from these enormous datasets have been shown to correlate well with the growth rates of strains in nature. Therefore, these assays show promise as a powerful method for approximating the human neutralizing antibody landscape [78, 77].

Another reason why forecasting remains difficult is the variation introduced by epistasis and pleiotropy, the central focus of this thesis. These topics are nicely reviewed in [103]. The effect of an HA mutation on antibody escape or receptor binding can vary with genetic background [115, 31]. Much work has shown that mutations in HA that impair a phenotype can become tolerated in the presence of other permissive mutations that repair it [114, 184, 181, 179, 93, 161, 97, 88]. As a consequence, the general opinion so far is that the number of antigenic shapes HA can assume is probably infinite.

1.4 Deep mutational scanning

Deep mutational scanning is a high-throughput method for generating comprehensive genotype-to-phenotype maps [45]. The method involves generating a large library of protein variants, subjecting the library to a selective pressure that represents a phenotype of interest, and deep sequencing the library composition before and after selection to simultaneously quantify how each variant affects the phenotype. Here, we will briefly review how deep mutational scanning has been applied to study properties of viral entry proteins.

Some of the first deep mutational scans on viral proteins were performed on influenza HA [162, 185]. These initial scans relied on reverse genetics to produce libraries of viruses containing mutant HAs and the 7 other internal genes from the lab-adapted A/WSN/1933(H1N1) strain. Saturated mutagenized libraries generated by reverse genetics were instrumental in defining the mutational tolerance of HA [36, 91], how mutations to HA escape monoclonal antibodies [37, 38, 180] and polyclonal sera [90], and how antibody specificies against HA differ across age groups [174]. Combinatorial mutagenesis libraries generated by reverse genetics helped reveal the prevalence of epistasis in the HA receptor binding pocket [184, 181, 179]. However, one limitation of these experiments is a biosafety concern since these are replication-competent mutant viruses.

A class of deep mutational scans that is far safer relies on yeast display. In these experiments, a library of mutant peptides is expressed on the surface of yeast. Most prominently, saturated mutagenized yeast display libraries of the SARS-CoV-2 receptor binding domain (RBD) have been used to reveal mutational constraints on RBD folding and receptor binding [153], how mutations to the RBD escape monoclonal antibodies [150, 151, 17] and polyclonal sera [59, 58], and epistatic shifts [152]. Combinatorial yeast display libraries of the RBD also revealed the role of epistasis in RBD receptor binding [112] and antibody binding [113]. However, the limitation of yeast display is the size of the peptide that can be displayed. This is why these experiments have been limited to the RBD, as the full SARS-CoV-2 spike protein or HA are too large. Additionally, these experiments are limited to measuring mutation effects on biochemical phenotypes: it is possible to measure how mutations affect antibody binding, but not neutralization.

The final class of deep mutational scans that we will describe is based on lentiviral pseudotyping [27]. The technical innovation here is conditionally replicative lentiviral particles that can only undergo a single cycle of infection can be pseudotyped with mutant viral entry proteins. Therefore, the advantages of these virus libraries are that they are safe, can in principle accomodate any viral entry protein, and can be used to study how mutations affect infection rather than biochemical phenotypes. So far, these libraries have been used to study the functional and antigenic effects of mutations to a diverse set of viral entry proteins including SARS-CoV-2 Spike, HIV envelope, nipah glycoprotein, lassa glycoprotein, rabies glycoprotein,

chikungunya virus entry protein, and influenza hemagglutinin [27, 133, 86, 19, 1, 72, 26]. The work in this thesis also used this pseudovirus deep mutational scanning platform.

1.5 Overview of the thesis

The goal of this thesis is to build upon our understanding of how epistasis and pleiotropy shape viral protein evolution. In **chapter 2**, we tackle the problem of predicting how a viral entry protein with arbitrary mutation combinations will be neutralized by human sera. We introduce a biologically interpretable extension of the global epistasis model in Eq. 1.4 and Eq. 1.5 that is inspired by the concept of antibody epitopes. The parameters in this model quantify how each viral mutation affects the antibody activity against each epitope targeted by antibodies in the sera, and we show how these parameters can be inferred from deep mutational scanning data.

In **chapter 3**, we perform pseudovirus deep mutational scanning experiments to discover pleiotropic conflicts in influenza HA evolution. In contrast to prior deep mutational scans, we measured how mutations affect multiple phenotypes: cell entry, acid stability, and serum antibody neutralization. In this way, we were able to show how HA suffers from the cost of complexity and that the strength of pleiotropic conflicts can vary across phenotypes. Specifically, we provide evidence that deleterious cell entry effects can be easily alleviated via epistasis, while deleterious acid stability effects may be more difficult to resolve.

Finally, in **chapter 4**, we compare pseudovirus deep mutational scanning datasets to investigate how mutation effects on cell entry differ across three divergent influenza HAs: human H3, avian H5, and avian H7. These HAs share just ~40% amino acid sequence identity, but their structures are remarkably conserved. We find that, despite sharing extremely similar structures, these HAs have dramatically different mutational constraints.

Chapter 2

A biophysical model of viral escape from polyclonal antibodies

A version of this chapter is published as:

> Timothy C. Yu*, Zorian T. Thornton*, William W. Hannon, William S. DeWitt, Caelan E. Radford, Frederick A. Matsen IV, Jesse D. Bloom, **A biophysical model of viral escape from polyclonal antibodies**, *Virus Evolution*, 2022

2.1 Abstract

A challenge in studying viral immune escape is determining how mutations combine to escape polyclonal antibodies, which can potentially target multiple distinct viral epitopes. Here we introduce a biophysical model of this process that partitions the total polyclonal antibody activity by epitope, and then quantifies how each viral mutation affects the antibody activity against each epitope. We develop software that can use deep mutational scanning data to infer these properties for polyclonal antibody mixtures. We validate this software using a computationally simulated deep mutational scanning experiment, and demonstrate that it enables the prediction of escape by arbitrary combinations of mutations. The software described in this paper is available at https://jbloomlab.github.io/polyclonal.

2.2 Introduction

Many viruses evolve antigenically to escape polyclonal antibodies elicited by vaccination or prior infection [148, 66, 9, 39]. Neutralization assays are the gold standard for experimentally assessing if a new viral variant has mutations that erode antibody immunity. However, neutralization assays require generating the actual viral variant(s) for individual testing, and can therefore only be effectively applied retrospectively to a modest number of viral variants of interest [34]. For this reason, neutralization assays have difficulty keeping pace with identification of vast numbers of emerging viral variants by genomic epidemiology

[41, 134, 166], and so it would be useful to have a method for accurately predicting the antigenic phenotype of viral variants with arbitrary combinations of mutations.

Unfortunately, predicting how a polyclonal serum will neutralize a new viral variant remains a challenge. Deep mutational scanning can systematically measure how large libraries of viral protein variants affect antibody neutralization or binding [35, 90, 180, 58, 59]. However, although such high-throughput experimental methods can assess the effects of all single mutants to some viral proteins, the number of possible multiply mutated variants far exceeds the limits of these experiments. Therefore, a variety of computational approaches have been developed that attempt to predict escape by new viral variants. These approaches include basic transformations of deep mutational scanning data [61], models that integrate antigenic data with phylogenetic [116] or sequence data [156, 64], and neural networks that can be trained using deep mutational scanning data [157] or sequence data alone [67, 159].

Here we introduce a new model of viral polyclonal antibody escape that has several advantages over existing computational approaches. Our model is interpretable in terms of underlying biophysical parameters, can be directly fit to experimental deep mutational scanning data, and can predict how new viral variants will be neutralized by the polyclonal sera used to generate the experimental data. We implement our model in a software package and validate it on simulated experimental data. Finally, we demonstrate how the parameters of the model provide quantitative intuition for how mutations combine to escape antibodies that target distinct viral epitopes.

2.3 Results

2.3.1 The concept of antibody epitopes

Our approach is inspired by the idea that viral antigens can be partitioned into distinct epitopes. This idea can be traced back over four decades to classic experiments on influenza, which tested viral mutants against large panels of monoclonal antibodies [87, 187, 171]. Viral escape mutants were first selected using individual antibodies, and then tested against other antibodies in the panel. A pattern that emerged from these experiments was that groups of antibodies were escaped by similar viral mutants (**Figure 2.1**). Antibodies that share common escape mutants were inferred to recognize a common epitope on the viral protein. For instance, in **Figure 2.1** antibodies 2 to 5 recognize a similar epitope since they are escaped by many of the same viral mutants.

Based on these studies, the H3 influenza hemagglutinin was divided into five distinct epitopes [176, 146]. This type of coarse epitope map also provided a straightforward way to conceptualize viral escape from polyclonal serum. Unlike monoclonal antibodies, polyclonal serum can contain multiple antibod-

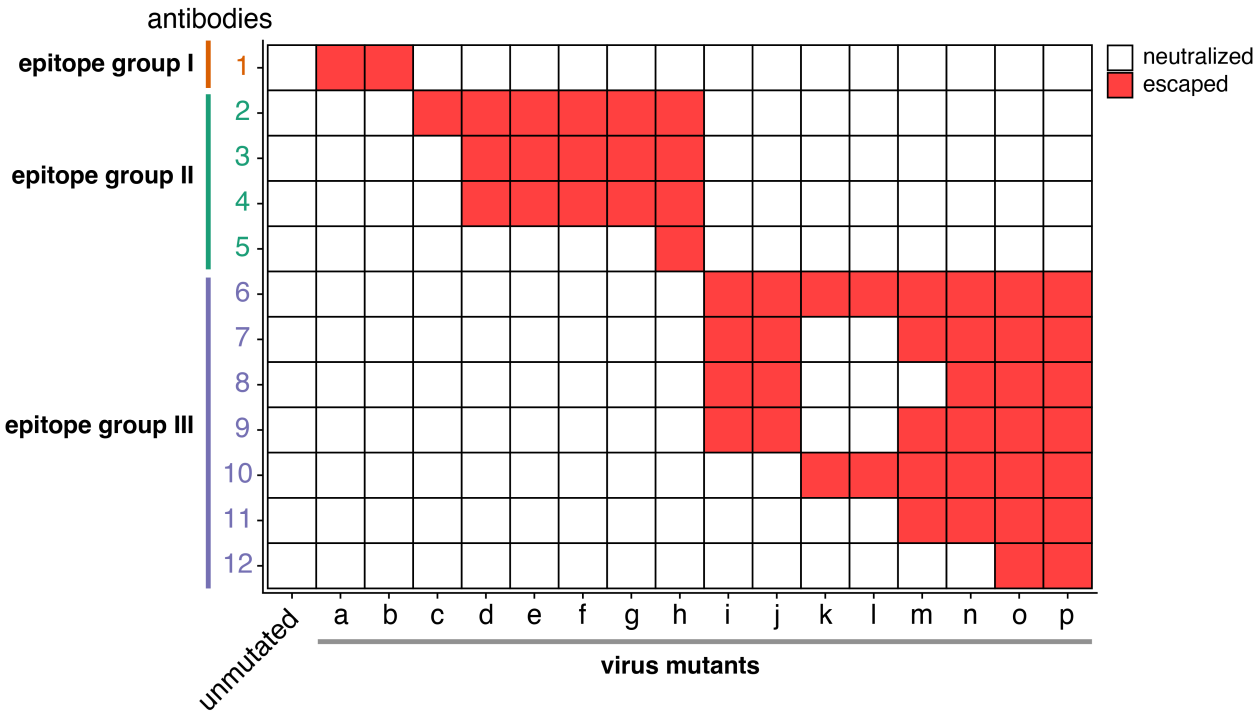

Figure 2.1: **Antibodies can be grouped into epitopes based on whether they share viral escape mutants.** Heatmap displaying classic experimental data extracted from Webster and Laver [171]. Influenza virus mutants (a-p) were selected using individual antibodies from a large panel of monoclonal antibodies. Each viral mutant was then tested to see if it was neutralized (white) or escaped (red) by the other antibodies in the panel. Antibodies were then grouped into epitopes based on their shared escape mutants.

ies, each recognizing discrete epitopes. As such, any variant that fully escapes polyclonal serum would need to escape antibodies binding at multiple epitopes.

The concept of dividing viral antigens into distinct epitopes has proven to be very useful and continues to be applied to new viruses such as SARS-CoV-2 [8, 128, 17]. However, grouping antibodies by epitopes is a simplifying approximation, as two antibodies targeting a similar epitope may be escaped by slightly different mutations, and some antibodies may bind idiosyncratic regions outside or between major epitopes [37, 128, 60, 59, 149]. For instance, in **Figure 2.1** antibodies 6 and 12 are grouped into the same epitope even though some viral mutants only escape one of these two antibodies. Nonetheless, the concept of epitopes provides a valuable way to interpret polyclonal antibody escape and forms the basis of the quantitative approach we take here.

2.3.2 An epitope-based model of viral escape from multiple antibodies

Given the concept of epitopes described above, consider viral escape from multiple antibodies. For simplicity, consider a hypothetical polyclonal mixture of just two antibodies (1 and 2) that bind distinct epitopes on a viral antigen. The functional activities of these two antibodies in the polyclonal mixture can differ due to antibody-intrinsic factors (e.g., binding affinity and neutralization potency) and extrinsic factors (e.g., antibody concentration). In our hypothetical antibody mixture, we assume antibody 1 has a higher functional activity than antibody 2.

To understand how mutations affect viral escape from this hypothetical two-antibody mixture, consider the viral variants in **Figure 2.2**. In the first variant, a single mutation escapes antibody 1, while leaving antibody 2 binding intact. Since antibody 1 has a higher functional activity, losing its contribution causes marked escape from the overall antibody mixture (**Figure 2.2A**). However, a viral variant with a single mutation that escapes antibody 2 but leaves antibody 1 binding intact has little escape from the overall antibody mixture, since the more active antibody 1 can still bind (**Figure 2.2B**).

Importantly, this framework makes distinct predictions about the effects of multiple mutations depending on whether they are in the same or different epitopes. Imagine if the viral variant has two mutations in antibody 1's epitope. If one of the mutations is already sufficient to mostly escape binding by antibody 1, then the second mutation will have a largely redundant effect (**Figure 2.2C**). It follows that multiple escape mutations in the same epitope will have diminishing returns—even when all antibody 1 molecules are unbound, antibody 2 can still bind. However, the situation is very different if the viral variant gains mutations in the epitopes of both antibody 1 and antibody 2. Since both antibodies are escaped, the polyclonal mixture will have no activity (**Figure 2.2D**). Note that the principles described above can be readily extended to mixtures of antibodies that target more than two distinct epitopes.

The simple hypothetical example described above is mirrored in real-world data by Kuzmina et al. [85] on SARS-CoV-2 escape from neutralization by polyclonal serum pooled from vaccinated individuals (**Figure 2.3**). The K417N mutation, which is located in the subdominant class 1 epitope [60] of the SARS-CoV-2 receptor binding domain (RBD) has little effect on polyclonal antibody escape. But E484K, which is located in the immunodominant class 2 epitope [60], causes a substantial drop in polyclonal antibody neutralization. But while K417N has no effect on its own, combining K417N with E484K causes a larger drop in neutralization than E484K alone, presumably due to escape from two distinct groups of antibodies in the sera targeting each epitope (**Figure 2.3**).

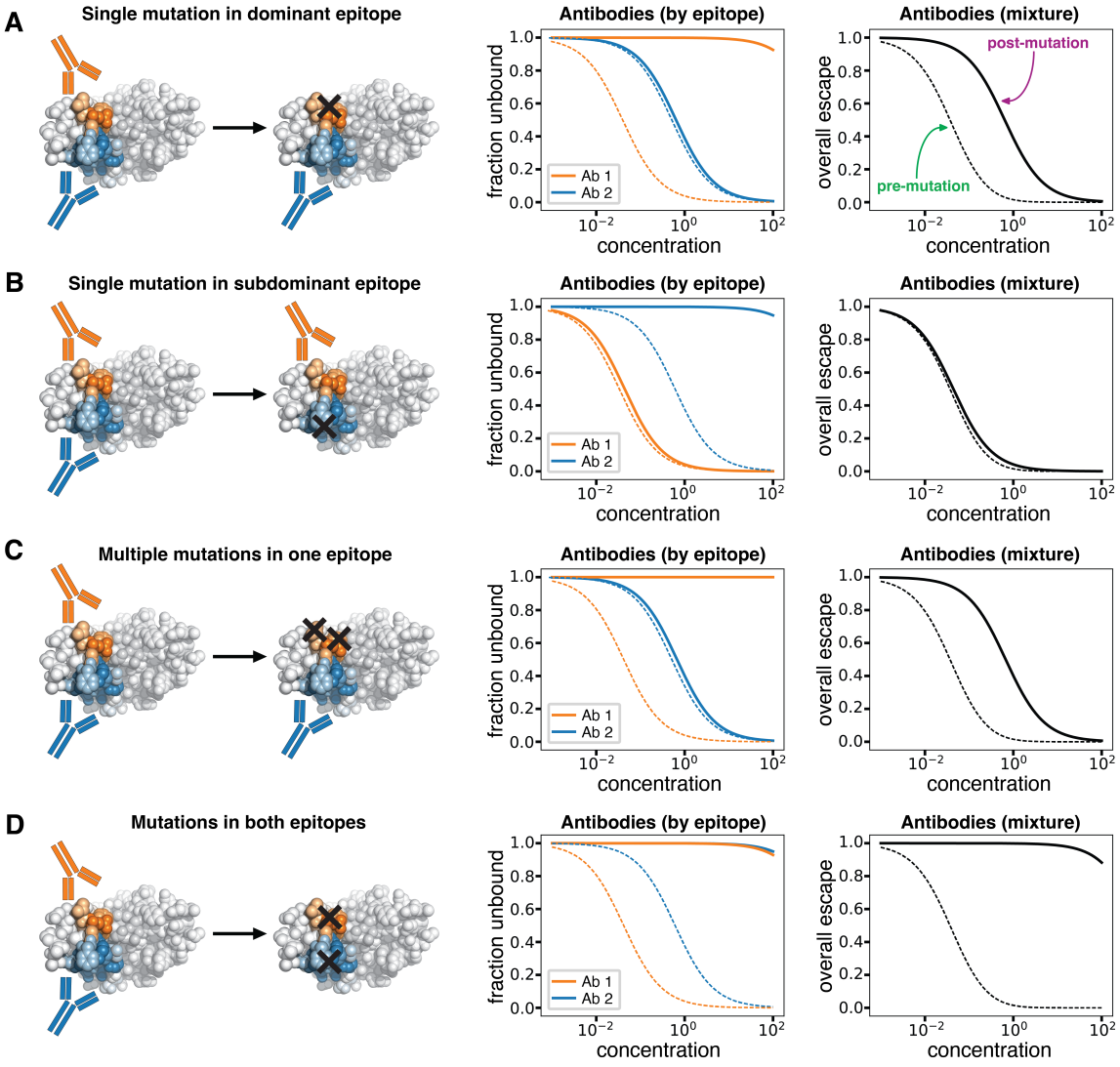

Figure 2.2: **Viral escape from a hypothetical mixture of antibodies targeting two different epitopes.** A) A single mutation in the dominant (orange) epitope substantially decreases but does not eliminate binding by the antibody mixture. B) A single mutation in the subdominant epitope (blue) has minimal effect on binding by the overall antibody mixture since binding of antibodies to the dominant epitope is unaffected. C) Multiple mutations in the dominant epitope have an effect that is no greater than a single mutation in this epitope since the remaining binding is due to antibodies targeting the subdominant epitope. D) Mutations in both epitopes completely escape binding by the antibody mixture. For each row, the plots show the fraction of antigens unbound by antibody as a function of antibody concentration. The left plot shows the fraction unbound for individual epitopes, and the right shows the overall fraction unbound. The dashed lines indicate binding to the unmutated antigen, while solid lines indicate binding to the mutated antigen.

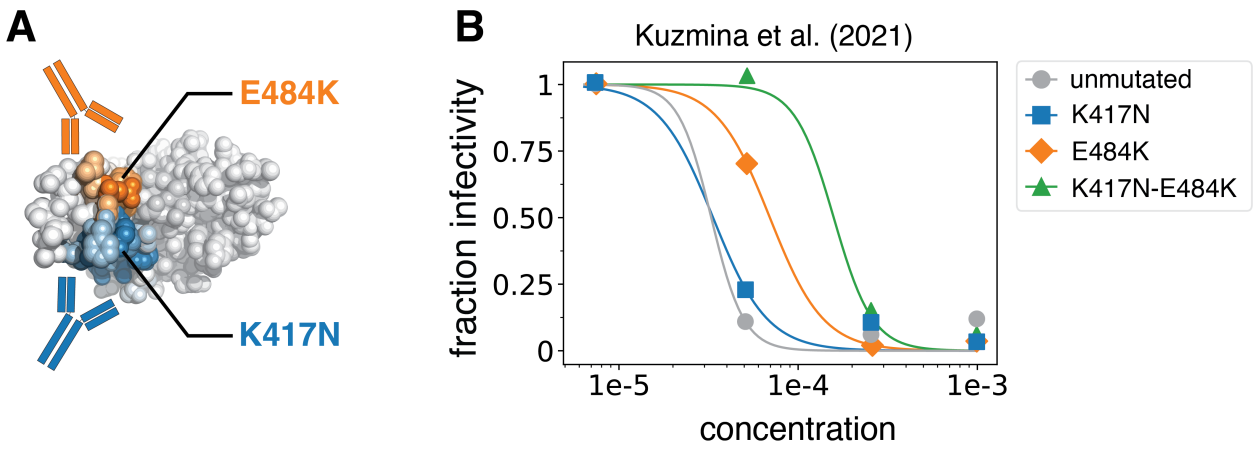

Figure 2.3: **Mutations at multiple epitopes have a synergistic effect on viral escape in real experimental data.** A) Structure of the SARS-CoV-2 RBD highlighting locations of the K417N and E484K mutations in the class 1 and 2 epitopes, respectively. B) Neutralization of unmutated SARS-CoV-2 spike, the K417N and E484K single mutants, and the double mutant against pooled serum from vaccinated individuals. Note how K417N alone has little effect on neutralization, but does cause substantial additional escape in the background of E484K. Experimental data was taken from Kuzmina et al. [85] and replotted here.

2.3.3 Biophysical modeling of polyclonal antibody escape

Here we formalize the epitope-based model of polyclonal antibody escape described above in terms of experimental measurables and relevant biophysical quantities. First, let $p(v, c)$ be the fraction of viral variant v that escapes a mixture of polyclonal antibodies at concentration c. The quantity $p(v, c)$ is an experimental measurable, for instance from a neutralization assay. Additionally, suppose the antibodies can bind to one of E epitopes on the viral antigen. Let $U_e(v, c)$ be the fraction of variant v that have an unbound epitope e when the antibody mixture is at concentration c. Assuming antibodies bind independently without competition, we can express $p(v, c)$ as:

$$p(v, c) = \prod_{e=1}^{E} U_e(v, c)$$

Note that relaxing the assumption that antibodies bind independently without competition to each epitope has little effect on $p(v, c)$ (see **Appendix**). Note also that this model simplifies escape to be the state where no antibodies are bound to a single idealized antigen, although in reality multiple antigens decorate each virion.

Next, we can define $U_e(v, c)$ in terms of underlying biophysical properties. Again assuming that there is no competition among antibodies binding to different epitopes, that antibodies to each epitope

are completely neutralizing, and that the antibody binding to a given epitope e can be described by a Hill curve with coefficient of one, then $U_e(v, c)$ is given by a Hill equation [40]

$$U_e(v,c) = \frac{1}{1 + \frac{cf_e}{K_{d,e}(v)}} = \frac{1}{1 + cf_e \exp\left(\frac{-\Delta G_e(v)}{RT}\right)} = \frac{1}{1 + c\exp(-\phi_e(v))}$$

where $-\phi_e(v)$ represents the functional activity of antibodies to epitope e against variant v. Note that $\phi_e(v)$ depends on both antibody-intrinsic factors (i.e., affinity as quantified by the free energy of binding $\Delta G_e(v)$ and extrinsic factors (i.e., relative fraction f_e of antibodies in the mix that bind epitope e). The overall functional activity directed to an epitope is a combination of these intrinsic and extrinsic factors, and can be expressed as

$$\phi_e(v) = \frac{\Delta G_e(v)}{RT} - \ln(f_e)$$

Note that RT is the product of the molar gas constant and the temperature, and

$$K_{d,e}(v) = \exp\left(\frac{\Delta G_e(v)}{RT}\right)$$

is the dissociation constant. For simplicity, we consider each $\phi_e(v)$ to be independent, so antibody binding at one epitope does not affect the affinity of antibodies binding at another epitope. Furthermore, we group together all antibodies targeting a given epitope and let $\phi_e(v)$ be their effective activity, simplifying the fact that each of these antibodies can have different activities and affinities. More positive values of $-\phi_e(v)$ indicate that antibodies that bind epitope e have a higher functional activity against variant v.

Lastly, we can write $\phi_e(v)$ in terms of the contributions of specific mutations. To do this, assume that mutations have additive effects on the free energy of binding for antibodies targeting any given epitope e [120, 121]. In this way, we assume that antigenic epistasis arises via the nonlinear Hill function that relates $\phi_e(v)$ to $U_e(v, c)$ and the product over $U_e(v, c)$ across epitopes. Specifically, let $a_{wt,e}$ be the functional activity of antibodies that bind epitope e on the unmutated viral antigen, with larger values of $a_{wt,e}$ indicating stronger antibody activity targeting this epitope. Let $\beta_{m,e}$ be the extent to which mutation m reduces antibody binding or neutralization at epitope e, with larger values of $\beta_{m,e}$ corresponding to a larger contribution to antibody escape. So, $\phi_e(v)$ can also be written as

$$\phi_e(v) = -a_{wt,e} + \sum_{m=1}^{M} \beta_{m,e} b(v)_m$$

where $b(v)_m$ is one if variant v has mutation m and 0 otherwise, and m ranges over all M possible mutations. Taken together, the above equations relate the pre-mutation functional activity of antibodies at each epitope ($a_{wt,e}$) and the antibody escape effects of individual mutations at each epitope ($\beta_{m,e}$) to the experimentally measured fraction $p(v, c)$ of variants v that escape an antibody mixture at concentration c.

2.3.4 Fitting biophysical models to deep mutational scanning data

We reasoned that the parameters of our biophysical model could be learned from experiments that measure $p(v, c)$ for a large number of variants, containing most possible single mutants and a sizable number of multiple mutants [45, 79]. These rich genotype-phenotype measurements can be obtained by viral deep mutational scanning. Briefly, viral deep mutational scanning involves generating a large library of viral or viral protein variants, incubating this library with antibodies or sera, and using deep sequencing to identify which variants successfully escape binding or neutralization [35, 90, 180, 58, 59]. While previous studies have been restricted to variants that predominantly contain single amino acid mutations, recent advances enable combinations of mutations to be assayed as well [29]. Although only an infinitesimal fraction of all combinations of mutations can be assayed, this approach does measure $p(v, c)$ for each mutation in many different backgrounds, which should be sufficient for revealing the epitopes targeted by polyclonal antibody mixtures and their associated escape mutations.

To fit our biophysical model using deep mutational scanning data, we created a Python software package named *polyclonal* that uses gradient-based optimization to fit the model to a large set of viral variants v and their corresponding experimentally measured escape values, $p(v, c)$. This software package estimates the $a_{wt,e}$ and $\beta_{m,e}$ parameters that best predict the measured $p(v, c)$ under tunable and biologically motivated constraints. These constraints are key to ensuring the inference of biologically accurate epitopes. We typically enforce a sparsity constraint that encourages most $\beta_{m,e}$ values to be close to 0, as most mutations to a viral antigen should not mediate antibody escape. Similarly, the $a_{wt,e}$ values are penalized to be close to 0 unless there is clear evidence for the contrary. We also usually enforce an evenness constraint, as most mutations to a site that mediates antibody escape at a specific epitope tend to have similar effects (or $\beta_{m,e}$'s). The software itself is available at `https://github.com/jbloomlab/polyclonal` and detailed documentation is at `https://jbloomlab.github.io/polyclonal`. The software also provides methods to visualize the resulting mutation-level escape values in interactive plots as described in the documentation.

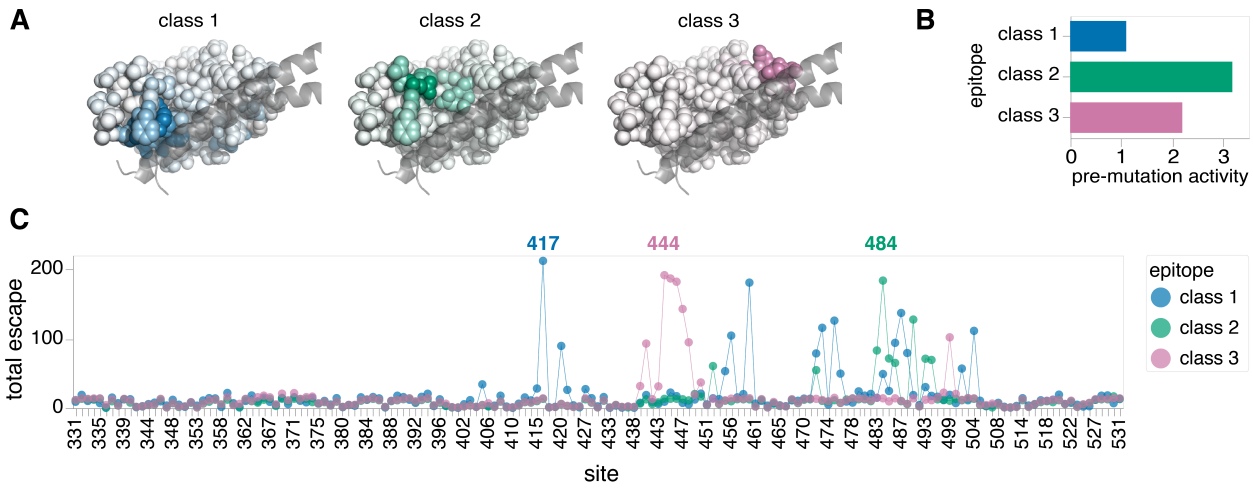

Figure 2.4: **A hypothetical polyclonal antibody mixture targeting the SARS-CoV-2 RBD.** A) Structures of the SARS-CoV-2 RBD in complex with key helices of ACE2. RBD sites are colored to indicate the extent to which they mediate escape from antibodies targeting each epitope in the hypothetical polyclonal mixture. B) Pre-mutation functional activities of antibodies ($a_{wt,e}$) for each epitope in the mixture. Note the class 2 epitope is immunodominant, whereas the class 1 epitope is subdominant. C) Sum of positive mutation escape effects ($\beta_{m,e}$) at each RBD site for each epitope. An interactive version of a heatmap showing all $\beta_{m,e}$ values is available at https://jbloomlab.github.io/polyclonal/visualize_RBD.html.

2.3.5 Validation with computationally simulated deep mutational scanning data

To validate the performance of our software, we simulated a hypothetical polyclonal antibody mixture that contains antibodies targeting three major neutralizing epitopes (class 1, 2, and 3) on the SARS-CoV-2 RBD (**Figure 2.4A**) [8, 60]. We assigned each epitope a different pre-mutation functional activity ($a_{wt,e}$) based on the order of typical neutralizing activities against these epitopes in actual human polyclonal serum (class 2 > class 3 > class 1) [60] (**Figure 2.4B**). Next, we assigned $\beta_{m,e}$ values using prior deep mutational scanning studies [150, 151] that measured the effects of all single RBD mutations on escape from prototypical monoclonal antibodies targeting each epitope (**Figure 2.4C**). Specifically, we used LY-CoV016 (etesevimab) for the prototype class 1 antibody, LY-CoV555 (bamlanivimab) for class 2, and REGN10987 (imdevimab) for class 3 [150, 151]. Note the site of greatest total escape (the sum of positive $\beta_{m,e}$ values at a site) is 417 for class 1, 484 for class 2, and 444 for class 3.

Based on this hypothetical polyclonal antibody mixture, we computationally simulated a realistic deep mutational scanning dataset containing 30,000 RBD variants. These variants contained an average of two amino acid mutations, with the number of mutations per variant following a Poisson distribution

(**Figure 2.7A**). These variants also only contained mutations at sites found to be functionally tolerated in prior deep mutational scanning, and these sites were well-represented in the simulated dataset (**Figure 2.7B**). We then calculated the true $p(v, c)$ for each variant using our biophysical model with the $a_{wt,e}$ and $\beta_{m,e}$ defined above. We did this for three concentrations of the hypothetical serum that represent the IC97.5, IC99.9, and IC99.998 against the unmutated RBD (**Figure 2.7C**). Lastly, we added gaussian noise, $N(0, 0.05)$, into the $p(v, c)$ measurements and then truncated the noisy values to be between 0 and 1 to reflect experimental errors and built in a 1% probability of adding or subtracting a mutation from a variant to portray sequencing errors.

We found that polyclonal could successfully infer the underlying properties of our hypothetical polyclonal antibody mixture when fit to the noisy, simulated deep mutational scanning dataset. The predicted $a_{wt,e}$ values were nearly identical to the true $a_{wt,e}$ values (**Figure 2.5A**), suggesting that we can deconvolve the dominance hierarchy of epitopes targeted by a polyclonal antibody mixture. Furthermore, the predicted $\beta_{m,e}$ values strongly correlated with the true $\beta_{m,e}$ values (**Figure 2.5B**, R^2=0.63 for class 1, R^2=0.91 for class 2, R^2=0.85 for class 3), indicating we can learn the effects of mutations on antibody escape at each epitope. Note the lower correlation for the class 1 epitope can be attributed to its relative subdominance. As shown in (**Figure 2.2B**), mutations to a subdominant epitope manifest little effect on the functional activity of the overall antibody mixture when the immunodominant epitopes remain unaffected, and so only have measurable effects in the subset of mutants with mutations in more dominant epitopes. Nonetheless, our approach can still learn these subdominant effects reasonably well. Taken together, these results demonstrate that noisy $p(v, c)$'s measured by deep mutational scanning can be modeled to reveal fine details of polyclonal antibody mixes: the extent to which antibodies target specific epitopes on a viral antigen and the extent to which mutations escape antibodies to each epitope.

We used the fit biophysical model to predict the extent to which variants that were not seen in our experiments will escape the same polyclonal antibody mixture. To do this, we simulated an independent deep mutational scanning dataset, grounded in the same true $a_{wt,e}$ and $\beta_{m,e}$ values, but with a higher number of mutations (three) on average per variant (**Figure 2.7A**). We found that our fit model could predict the IC90 (the concentration required for $p(v, c) = 0.1$) of each variant in the independent dataset with high accuracy (**Figure 2.5C**, R2=0.98). Ultimately, *polyclonal* can be applied to make predictions over all variants with mutations that were observed by deep mutational scanning.

2.3.6 Model fitting is dependent on experimental design

We next sought to clarify the experimental conditions for deep mutational scanning that lead to accurate model fitting with polyclonal. To that end, we systematically explored the impact of three important experimental conditions on model fitting through simulation (see **Methods**).

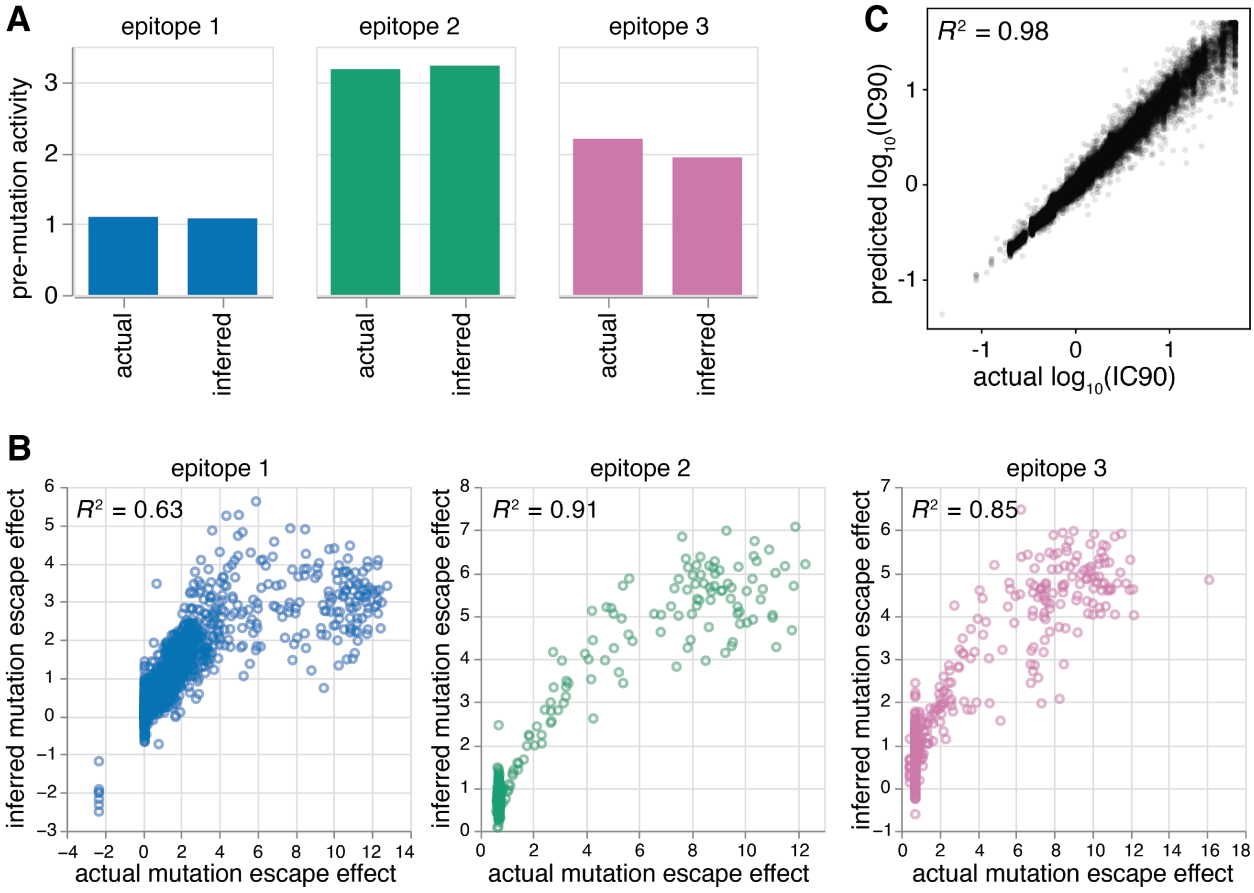

Figure 2.5: **Model validation using a computationally simulated deep mutational scanning dataset.** A) Pre-mutation functional activities of antibodies ($a_{wt,e}$) inferred by the fit model match the actual $a_{wt,e}$ for each epitope. B) Mutation escape effects ($\beta_{m,e}$) inferred by the fit model strongly correlate with the actual $\beta_{m,e}$ for each epitope used in the simulation. Mutation escape effects for the immunodominant class 2 epitope are most correlated, while escape effects for the subdominant class 1 epitope are least correlated. C) The IC90's predicted by the fit model strongly correlate with the actual IC90's of an independently simulated dataset with a higher mutation rate (three mutations on average per variant).

We first examined the effect of library mutation rate, an important consideration for library design because variants containing multiple mutations are key to revealing epitopes. If a library only contained variants with single mutations, it should not be possible to detect the presence of subdominant epitopes, due to the phenomenon in **Figure 2.2B**. Indeed, we found that a library containing 30,000 variants with an average of one mutation could only infer the $\beta_{m,e}$ values for immunodominant class 2 epitope (**Figure 2.6A**), highlighting the need for including multiply mutated variants. On the other hand, a library containing 30,000 variants with two mutations on average was sufficient for inferring the $\beta_{m,e}$ values at all three epitopes, but the accuracy improved as the mutation rate increased (**Figure 2.6A**), consistent with our expectation that greater coverage of variants with multiple epitope mutations is helpful. Note that these simulations do not capture the real-world fact that variants will be increasingly less likely to be functional as they accumulate more mutations.

Next, we investigated the effect of library size, another important library design consideration. If there are too few variants in the library, mutations may not be observed in enough backgrounds to be able to deconvolve their effects on different epitopes. Above we showed that a simulated library with 30,000 variants with three mutations on average could accurately infer the $\beta_{m,e}$ values at all three epitopes. Therefore, we set out to determine the minimum number of variants, with three mutations on average, required to accurately infer the $\beta_{m,e}$ values at all three epitopes. We found that at least 20,000 functional variants were required to accurately infer the $\beta_{m,e}$ values at each epitope (**Figure 2.6B**). We also noticed the $\beta_{m,e}$ values of immunodominant epitopes can be inferred with fewer variants (**Figure 2.6B**), consistent with the idea that effects of mutations at subdominant epitopes can only be observed in the backgrounds where the immunodominant epitope is already mutated.

Lastly, we explored the effect of antibody concentration, an important consideration for deep mutational scanning selections. If the concentration is too high, all variants will be neutralized. If the concentration is too low, there will be little measurable effect from the mutations. To test the effect of different concentrations, we again used the simulated library containing 30,000 variants with three mutations on average. First, we tested if data collected at a single concentration was sufficient. We found that a single concentration of IC99.9 against the unmutated RBD was most effective at inferring the $\beta_{m,e}$ values for each epitope, but there does indeed exist a fine balance (**Figure 2.6C**). Particularly for the subdominant class 1 epitope, the accuracy is lower when the concentration is too low or too high. We then tested if model fitting could be improved by including additional concentrations flanking the IC99.9, spanning the IC91.443 to IC99.998. Indeed, we found that the accuracy increases as the number of concentrations measured increases (**Figure 2.6D**), consistent with our expectation that obtaining more data points along the binding curve is helpful for quantifying the effects of mutations.

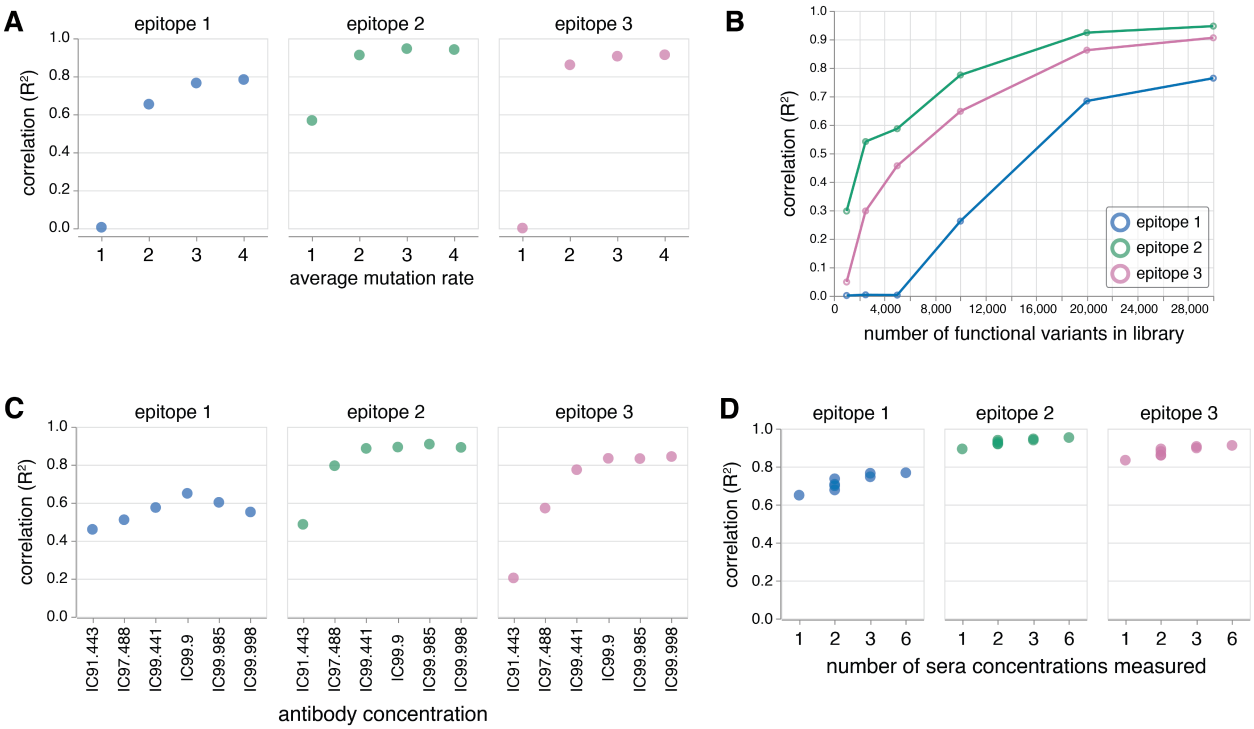

Figure 2.6: **Model fitting on simulated dataset depends on experimental design.** A) Correlation between inferred and actual mutation escape effects ($\beta_{m,e}$) improves as the average number of mutations per variant (assuming a Poisson distribution) in the library increases. In particular, the subdominant epitopes (epitopes 1 and 3) can only be accurately fit in libraries with mutation rates higher than one. B) Correlation between inferred and actual mutation escape effects ($\beta_{m,e}$) improves as the number of functional variants in the library increases. C) Correlation between inferred and actual mutation escape effects ($\beta_{m,e}$) depends on the concentration of the antibody mixture. D) Correlation between inferred and actual mutation escape effects ($\beta_{m,e}$) improves as the number of antibody concentrations measured and used to fit the model increases. For details on concentrations used, see: https://jbloomlab.github.io/polyclonal/concentration_set.html.

2.4 Discussion

We have described a biophysical model of viral escape from polyclonal antibodies. Notably, this model is composed of easily interpretable parameters that capture the interactions between antibodies and the viral epitopes they bind. In addition, we developed a software package that can infer these parameters using deep mutational scanning data. Using a simulated deep mutational scanning dataset, we demonstrated that this approach can infer true parameters from noisy experiments if the deep mutational scanning experiment is appropriately designed.

There are several limitations to our approach. Grouping antibodies by discrete epitopes is an approximation because each antibody is unique, however, decades of experimental work has shown that an epitope-based representation offers a useful way to interpret viral escape. Our model also does not explicitly consider the fact that there are multiple antigens per virion, and instead models escape as simply being the state where no antibodies bind a single idealized antigen. Additionally, our model assumes a specific shape of antigenic epistasis: mutations have additive effects on binding affinity at each epitope, but can manifest non-linear effects on the overall measured phenotype (e.g., neutralization) due to both the non-linear Hill curves that relate binding affinity to total fraction bound at an epitope and the product of these fractions across epitopes. Note that the single-epitope version of our model is similar to the global epistasis models that have proven so useful for interpreting some other types of deep mutational scanning data [121, 158], while the multi-epitope version resembles a fuzzy logic model of multiple biophysical traits [169]. Our model also assumes that antibody binding to one epitope does not influence the affinity of antibodies to other epitopes, and that the Hill curves have a coefficient of one. It is possible that these assumptions could be relaxed in elaborated versions of our model. We expect that these assumptions will hold reasonably well for viral variants with modest numbers of mutations, but may not extrapolate accurately to variants with dozens of mutations relative to the parental strain used for the deep mutational scanning experiment.

Despite these limitations, our model not only predicts the escape potential of viral variants with arbitrary combinations of mutations that are observed in a simulated deep mutational scanning library—it also clarifies how escape mutations combine to determine the magnitude of viral escape. While this manuscript was under review, our model was successfully applied to real deep mutational scanning data measuring escape of SARS-CoV-2 spike variants from monoclonal antibodies, yielding predictions that strongly correlated with neutralization assays [29]. While this paper only considers simulated data, we envision that our model can be further applied to appropriately designed deep mutational scanning experiments to address two main questions: (1) delineating the epitopes targeted by polyclonal serum, and (2) predicting the antigenic properties of new variants with arbitrary combinations of mutations.

2.5 Supplementary Material

2.5.1 Appendix

We have described a biophysical model that assumes a polyclonal antibody mixture can be divided into independent groups of antibodies that bind to distinct epitopes without competition. Here we interrogate the validity of this assumption, being cognizant of the observation that realistic viral epitopes are often overlapping and therefore not distinct. To do this, we draw from statistical mechanics principles to compare the antibody escape fractions predicted by our independent epitope model and an identically formulated model that instead assumes all epitopes are overlapping.

Monoclonal antibody case

Before considering the polyclonal antibody case, we first consider the case of a monoclonal antibody that binds a viral antigen. Here, the viral protein can exist in two microstates: bound or unbound by the antibody. The Boltzmann weight is 1 for the unbound state and $\frac{c}{K_d}$ for the bound state, where c is the antibody concentration and K_d is the dissociation constant of antibody-antigen binding. These weights can be derived using the steady-state approximation [40]. We can then define the partition function Ξ as

$$\Xi = \sum_i Z_i = Z_{\text{unbound}} + Z_{\text{bound}}$$

where Z_i represents the Boltzmann weights of the i microstates. Given this, the probability of a viral antigen being unbound is

$$p_{\text{unbound}} = \frac{Z_{\text{unbound}}}{\Xi} = \frac{1}{1 + \frac{c}{K_d}}$$

Polyclonal antibody case

For a polyclonal antibody mixture, we modify c to represent the concentration of the polyclonal antibody mixture. We assume that the polyclonal antibody mixture contains antibodies that bind one of E epitopes. As follows, the Boltzmann weight of the state where epitope e is bound is modified to $\frac{cf_e}{K_{d,e}}$, where f_e represents the fraction of antibodies in the mixture that target epitope e, and $K_{d,e}$ is the dissociation constant of antibodies binding to epitope e.

Two distinct epitopes In a polyclonal antibody mixture, new microstates exist where multiple epitopes are bound by antibodies. For example, we can consider a viral antigen that contains two distinct

epitopes (1 and 2) that are targeted by polyclonal antibodies. In addition to the microstates where a single epitope is bound, we now require an additional microstate where both epitopes are bound. The Boltzmann weight for this new microstate is

$$Z_{12,\text{bound}} = \left(\frac{cf_1}{K_{d,1}}\right)\left(\frac{cf_2}{K_{d,2}}\right)$$

We can then rewrite the partition function Ξ as

$$\Xi = \sum_i Z_i = Z_{\text{unbound}} + Z_{1,\text{bound}} + Z_{2,\text{bound}} + Z_{12,\text{bound}}$$

and the probability of a viral antigen being unbound is

$$\begin{aligned} p_{\text{unbound}} = \frac{Z_{\text{unbound}}}{\Xi} &= \frac{1}{1 + \frac{cf_1}{K_{d,1}} + \frac{cf_2}{K_{d,2}} + \left(\frac{cf_1}{K_{d,1}}\right)\left(\frac{cf_2}{K_{d,2}}\right)} \\ &= \left(\frac{1}{1 + \frac{cf_1}{K_{d,1}}}\right)\left(\frac{1}{1 + \frac{cf_2}{K_{d,2}}}\right) \end{aligned}$$

Note that this is the biophysical model that is described in the main text.

Two overlapping epitopes In the previous section, the two epitopes were distinct and there was no competition amongst antibodies. However, if the epitopes are overlapping and there is competition, then the microstate where both epitopes are bound ($Z_{12,\text{bound}}$) can no longer exist. In this case, the probability of a viral antigen being unbound is

$$p_{\text{unbound}} = \frac{Z_{\text{unbound}}}{\Xi} = \frac{1}{1 + \frac{cf_1}{K_{d,1}} + \frac{cf_2}{K_{d,2}}}$$

Extending beyond two epitopes The same logic applies to viral antigens with more than two epitopes targeted by antibodies. For example, we can write p_{unbound} for the case of three distinct epitopes as

$$p_{\text{unbound}} = \frac{Z_{\text{unbound}}}{\Xi} = \left(\frac{1}{1 + \frac{cf_1}{K_{d,1}}}\right)\left(\frac{1}{1 + \frac{cf_2}{K_{d,2}}}\right)\left(\frac{1}{1 + \frac{cf_3}{K_{d,3}}}\right)$$

and the case of three overlapping epitopes as

$$p_{\text{unbound}} = \frac{Z_{\text{unbound}}}{\Xi} = \frac{1}{1 + \frac{cf_1}{K_{d,1}} + \frac{cf_2}{K_{d,2}} + \frac{cf_3}{K_{d,3}}}$$

Overall, we found that the predicted p_{unbound} does not differ by much between the independent and overlapping epitope models under realistic c's, f's, and K_d's. However, the predicted p_{unbound} becomes more discordant between the two models as the number of epitopes increases, given the number of microstates with multiply bound epitopes increases. In practice, we only fit models to a handful of epitopes and not all of them will overlap. As such, we maintain that the independent epitope assumption is appropriate. To interactively explore how p_{unbound} differs between the two models, see https://jbloomlab.github.io/polyclonal/partition_function.html.

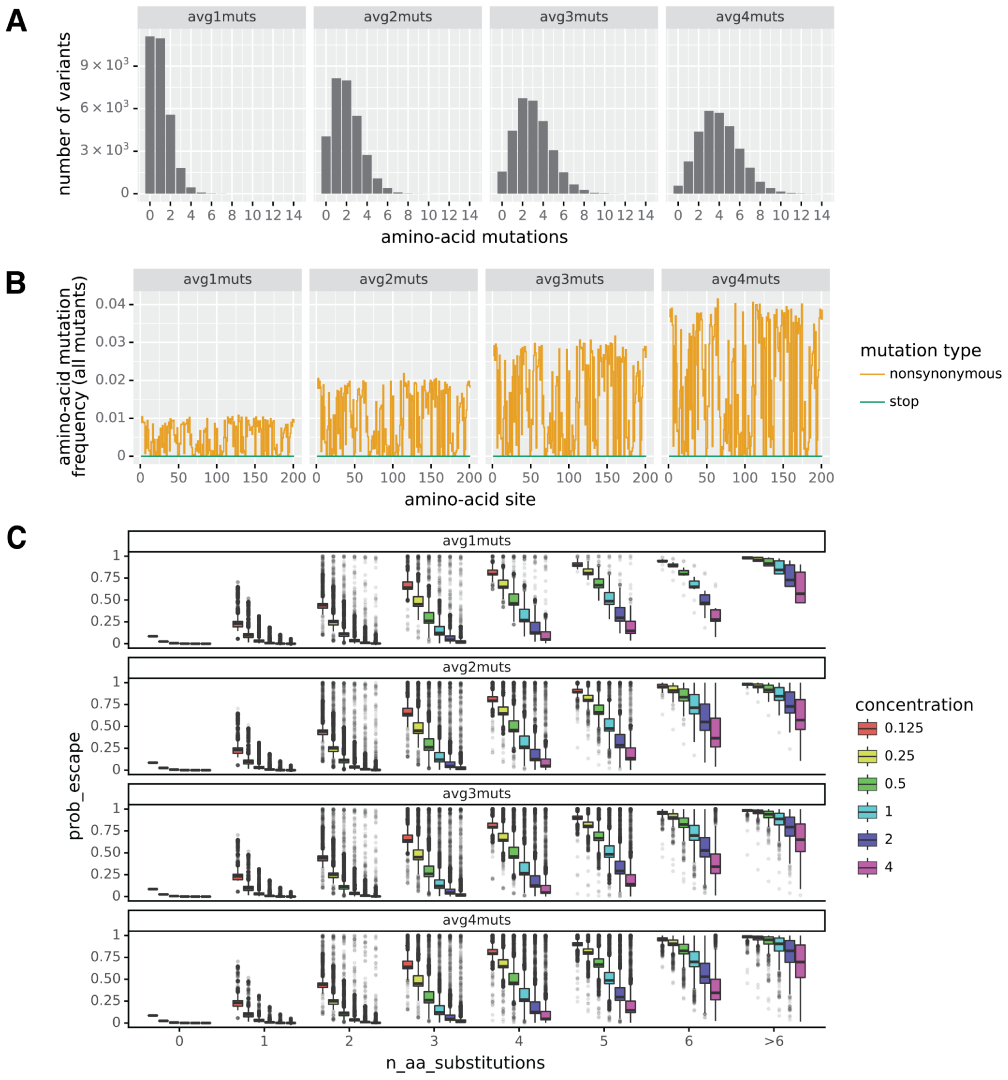

Figure 2.7: **RBD dataset simulation details.** A) Distribution of the number of amino-acid mutations per variant in each simulated library. B) Frequency of mutations at each site on the RBD in each simulated library. C) Distribution of antibody escape fractions, $p(v, c)$, in each simulated library across six concentrations.

2.6 Methods

Model fitting

Our goal is to estimate the biophysical model parameters that best predict the deep mutational scanning escape measurements under biologically motivated constraints. We defined a loss function that is robust to outliers

$$L = \sum_{v,c} h_{\delta_{\text{loss}}} \left[p(v,c) - \hat{p}(v,c) \right]$$

where $p(v,c)$ is the actual antibody escape fraction for variant v at concentration c, $\hat{p}(v,c)$ is the predicted antibody escape fraction for variant v at concentration c, and $h_{\delta_{\text{loss}}}(x)$ is a scaled Pseudo-Huber function, defined as

$$h_{\delta_{\text{loss}}}(x) = \frac{\delta^2 \left(\sqrt{1 + (x/\delta)^2} - 1 \right)}{\delta}$$

where δ is a parameter that indicates when the loss transitions from being quadratic (L2-like) to linear (L1-like). Note that the loss is mostly L2-like when x, the residual, is small. However, the loss transitions to become more L1-like when x is large, making it more robust to outliers. A default loss = 0.01 was used in all fit models. To minimize this loss function, we use the gradient-based L-BFGS-B method implemented in `scipy.optimize.minimize`.

Regularization

Additionally, we implemented penalty terms to regularize the parameters to behave under biologically motivated constraints. We regularize the escape values ($\beta_{m,e}$) using a Pseudo-Huber function, based on the notion that most mutations should not mediate escape.

$$R_{\text{escape}} = \lambda_{\text{escape}} \sum_{m,e} h_{\delta_{\text{escape}}} \left(\beta_{m,e} \right)$$

where λ_{escape} is the strength of the regularization and δ_{escape} is the Pseudo-Huber delta parameter. For all fit models, the default parameters λ_{escape} = 0.02 and δ_{escape} = 0.1 were used.

We also regularize the variance of escape values $\beta_{m,e}$ at each site, based on the notion that mutations at a site involved in escape will exhibit similar effects.

$$R_{\text{spread}} = \lambda_{\text{spread}} \sum_{e,i} \frac{1}{M_i} \sum_{m \in i} \left(\beta_{m,e} - \frac{1}{M_i} \sum_{m' \in i} \beta_{m',e} \right)^2$$

where λ_{spread} is the strength of the regularization, i ranges over all sites, M_i is the number of mutations at site i, and $m \in i$ indicates all mutations at site i. For all models fit, the default parameter $\lambda_{\text{spread}} = 0.25$ was used.

Lastly, we regularize the pre-mutation functional activities ($a_{wt,e}$) using a Pseudo-Huber function as these should be less positive (or even negative) unless there is clear evidence to the contrary.

$$R_{\text{activity}} = \lambda_{\text{activity}} \sum_{e} h_{\delta_{\text{activity}}} \left(a_{wt,e} \right) \quad \text{if } a_{wt,e} \geq 0$$

where $\lambda_{\text{activity}}$ is the strength of the regularization, δ_{activity} is the Pseudo-Huber delta parameter, and $R_{\text{activity}} = 0$ when $a_{wt,e} < 0$. For all models fit, the default parameters $\lambda_{\text{activity}} = 1.0$ and $\delta_{\text{activity}} = 0.1$ were used.

For more information on these penalties and model fitting, see https://jbloomlab.github.io/polyclonal/optimization.html.

Determining number of epitopes

Fitting the model requires specifying the number of epitopes *a priori*. However, it is not possible to know the number of epitopes that are targeted by antibodies in polyclonal serum in practice. Our approach to resolving this is similar to the "elbow method" commonly used to determine the optimal number of clusters in k-means clustering. We start by fitting a model with one epitope and iteratively fit models with an increasing number of epitopes. At some point, the N-th epitope becomes redundant. This is evidenced by a highly negative $a_{wt,e}$ value (i.e., if antibodies existed against this epitope, they are never bound) and all near-zero $\beta_{m,e}$ values, indicating that the previous fit model, containing N - 1 epitopes, is the one that best describes the polyclonal mixture. To view how this approach was applied to the simulated RBD example, see https://jbloomlab.github.io/polyclonal/specify_epitopes.html.

Experimental design simulation

We computationally simulated deep mutational scanning libraries based on the hypothetical polyclonal antibody mixture shown in **Figure 2.4**. All libraries contained 30,000 variants, but differed by their mutation rate with variants containing an average of one, two, three, or four mutations. Furthermore, the number of mutations per variant in each library followed a Poisson distribution. Variant escape was

also simulated under six concentrations in each library. These concentrations represented the IC91.443, IC97.488, IC99.441, IC99.9, IC99.985, and IC99.998 against the unmutated RBD antigen. For more details on how these experiments were simulated, see https://jbloomlab.github.io/polyclonal/simulate_RBD.html.

To make comparisons about model fitting, models were fit with identical parameters except for the experimental variable of interest: library mutation rate, library size, and antibody concentration.

To determine the impact of library mutation rate, models were fit to simulated datasets for libraries containing one, two, three, or four mutations on average. All datasets contained 30,000 variants and were measured at three different concentrations.

To determine the impact of library size, models were fit to simulated datasets containing different-sized subsets of variants that were randomly sampled from a library containing an average of three mutations per variant and measured at three different concentrations.

To determine the impact of antibody concentration, models were fit to simulated datasets to a library measured at one or multiple antibody concentrations. This library contained 30,000 variants and three mutations on average per variant. For more information, see https://jbloomlab.github.io/polyclonal/expt_design.html.

Code availability

Software source code, along with code and data that reproduce the figures (except **Figure 2.3**), are available at https://github.com/jbloomlab/polyclonal. Code and data for reproducing the neutralization curves in **Figure 2.3** are available at https://github.com/jbloomlab/polyclonal-paper. Software documentation is available at https://jbloomlab.github.io/polyclonal.

Acknowledgements

This work was supported in part by the NIH/NIAID under contract 75N93021C00015 (to JDB), grants R01AI141707 and R01AI165821 (to JDB), and grant F31AI150163 (to WSD). The work was also supported by the NIH/NIGMS CMB Training Grant (T32 GM007270) to TCY and the NSF Graduate Research Fellowship (DGE-2140004) to TCY. JDB and FAM are Investigators of the Howard Hughes Medical Institute.

Chapter 3

Pleiotropic mutational effects on function and stability constrain the antigenic evolution of influenza hemagglutinin

A version of this chapter is published as:

> Timothy C. Yu, Caroline Kikawa, Bernadeta Dadonaite, Andrea N. Loes, Janet A. Englund, Jesse D. Bloom, **Pleiotropic mutational effects on function and stability constrain the antigenic evolution of influenza hemagglutinin**, *Nature Ecology & Evolution*, 2025

3.1 Abstract

The evolution of human influenza virus hemagglutinin (HA) involves simultaneous selection to acquire antigenic mutations that escape population immunity while preserving protein function and stability. Epistasis shapes this evolution, as an antigenic mutation that is deleterious in one genetic background may become tolerated in another. However, the extent to which epistasis can alleviate pleiotropic conflicts between immune escape and protein function/stability is unclear. Here, we measure how all amino acid mutations in the HA of a recent human H3N2 influenza strain affect its cell entry function, acid stability, and neutralization by human serum antibodies. We find that epistasis has entrenched certain mutations so that reverting to the ancestral amino acid identity in earlier strains is no longer tolerated. Epistasis has also enabled the emergence of antigenic mutations that were detrimental to HA's cell entry function in earlier strains. However, epistasis appears insufficient to overcome the pleiotropic costs of antigenic mutations that impair HA's stability, explaining why some mutations that strongly escape human antibodies never fix in nature. Our results refine our understanding of the mutational constraints that shape recent H3N2 influenza evolution: epistasis can enable antigenic change, but pleiotropic effects can restrict its trajectory.

3.2 Introduction

The evolution of human influenza viruses is shaped by selection from population immunity. This immune pressure is especially apparent in the evolution of the viral hemagglutinin (HA) protein, which is the major target of neutralizing antibodies [23, 84]. Due largely to antibody-mediated immune pressure, the HA of human H3N2 influenza virus fixes an average of 3-4 amino acid substitutions per year [78, 148, 9, 125, 43].

However, HA's antigenic evolution is constrained by its essential role in viral fitness, as it binds to the host cell receptor (sialic acid) and mediates fusion of the viral and cell membranes. Many mutations impair these functions, yet human influenza viruses have demonstrated—both in the laboratory and in nature—the ability to rapidly adapt in the face of these constraints [114, 184, 181, 179, 93, 161, 97, 88]. Prior work has revealed that epistatic interactions among mutations in HA play a role in facilitating these adaptations. For example, mutations that impair receptor binding can become tolerated in the presence of other mutations that help restore binding [114, 184, 181, 179, 93, 161, 97], while mutations that enhance receptor binding can help buffer the effects of deleterious mutations [88].

Although epistasis among mutations affecting receptor binding is an established mechanism for resolving constraints on HA evolution, it is less clear how epistasis involving other molecular phenotypes shapes evolution. Many studies have used deep mutational scanning to measure the effects of HA mutations at scale, but these measurements have been typically limited to a single phenotype: cell entry or viral replication in cell culture [184, 181, 179, 174, 162, 36, 91, 185]. One phenotype with poorly understood evolutionary constraints is HA acid stability. As influenza virions are internalized into acidifying endosomes, HA undergoes a pH-triggered destabilization from its metastable pre-fusion form to a conformation that is primed for mediating membrane fusion [147]. While the structural transitions of this conformational change have been characterized in exquisite [10], we lack a complete understanding of how mutations to human H3N2 influenza HA affect acid stability, whether these effects impose pleiotropic costs on antigenic evolution, and whether such costs can be alleviated through epistasis.

Here, we used pseudovirus deep mutational scanning [29, 26] to measure how all amino acid mutations in the HA of a recent human H3N2 influenza strain affect cell entry, acid stability, and neutralization by human serum antibodies. By comparing these data to amino acid frequencies at each HA site observed in natural viral evolution, we assessed the extent to which epistasis modulates mutation effects on cell entry and acid stability, and whether pleiotropic costs on these phenotypes could be alleviated to enable antigenic mutations to fix. The effects of many mutations on cell entry have changed over time—and epistatic interactions enabled an antigenic mutation that was highly deleterious to cell entry in 2009 to eventually fix in 2022. However, the effects of mutations on acid stability show little evidence of epista-

sis, and several antigenic mutations that pleiotropically reduce acid stability have never fixed. Our results indicate that epistasis plays a central role in driving HA evolution, but its contribution to overcoming pleiotropic costs depends on the underlying molecular phenotype.

3.3 Results

3.3.1 Pseudovirus deep mutational scanning of HA from a recent human H3N2 strain

To measure the effects of mutations to HA on different key molecular phenotypes in high-throughput, we used a recently developed pseudovirus deep mutational scanning approach [29, 26]. In brief, we generated genotype-phenotype linked pseudovirus libraries where each virion encodes a mutant HA gene in its genome that matches the HA protein expressed on its surface (**Figure 3.5A-B**). Each mutant HA is coupled to a unique nucleotide barcode, forming variants whose phenotypic effects can be measured in a single multiplexed experiment via short-read sequencing of the barcodes (**Figure 3.1A**). These pseudoviruses also express the matched H3N2 neuraminidase (NA) on their surfaces, but this NA is supplied from a separate plasmid and not encoded in the pseudovirus genome. Importantly, these pseudoviruses encode no viral genes other than HA and can only undergo a single round of cell entry. These pseudoviruses are therefore not infectious agents capable of causing disease and so provide a safe way to study HA mutations at biosafety-level 2.

We created duplicate libraries in the background of the HA from A/Massachusetts/18/2022 (MA22), which was the H3N2 strain included in the 2024-2025 seasonal influenza vaccine [47]. These libraries were designed to contain every possible amino acid mutation in the HA ectodomain (H3 numbering: 1 to 504) for a total of 504 x 19 = 9576 mutations. The final libraries contained 64,032 and 70,581 barcoded HA variants that covered 98.7% and 99.0% of all possible mutations, respectively (**Figure 3.5C**). Most variants contained a single HA mutation (65%), while others contained zero (15%) or multiple mutations (20%) (**Figure 3.5D**). To extract information from the multiply mutated variants, we used global epistasis models [121, 189] to disentangle the effects of individual mutations on measured phenotypes (**Methods**).

3.3.2 Mutation effects on HA-mediated cell entry

We quantified the effects of HA mutations on pseudovirus entry into MDCK-SIAT1 cells [106], which express high levels of the a2-6-linked sialic acids preferred by human influenza HAs (**Figure 3.1A-B**, **Figure 3.6**, and interactive heatmaps at https://dms-vep.org/Flu_H3_Massachusetts2022_DMS/cell_entry.html). A negative effect indicates the mutation impairs cell entry, potentially via one

or a combination of reasons such as impaired receptor binding, fusion competency, HA folding, or HA expression. The measurements of mutation effects were highly correlated between the two independent replicate libraries (r = 0.95, **Figure 3.7A**). We validated the deep mutational scanning measurements of mutation effects on cell entry for 15 mutations with a range of effects on cell entry using conditionally replicative influenza viruses that lack the PB1 gene (**Figure 3.8A-B**) [68, 37]. The titers of the conditionally replicative influenza virions were highly correlated with the cell entry effects obtained by deep mutational scanning (r = 0.88, **Figure 3.8C**).

The deep mutational scanning showed that the receptor binding pocket is heavily constrained overall (**Figure 3.1C**), but that the distribution of cell entry effects varies across its different structural regions (**Figure 3.14**). Some areas, like the base of the receptor binding pocket, are highly constrained, while others, like the 150-loop, are more tolerant of mutations (**Figure 3.1D**, **Figure 3.6**). These measurements of the tolerance of different regions to mutations with respect to their effects on cell entry correlate with the variability of different sites in HA during the natural evolution of human H3N2 since 1968 (compare mutation effects and entropy among natural sequences in **Figure 3.1D**). For example, the 150-loop has seen substantial divergence during H3N2 HA's natural evolution, whereas the base of the receptor-binding pocket remains highly conserved, with only a single substitution at site 195 (Y to F) occurring in the early 2020s.

Many mutations within classically defined antigenic regions (epitopes A-E) [171, 146] tend to be well tolerated for HA's cell entry function (**Figure 3.1E**). However, epitopes that partially overlap with the receptor binding pocket (epitopes A, B, and D) are more constrained. Of these, epitope B is the most constrained yet exhibits the highest variability among natural human H3N2 influenza sequences (**Figure 3.1E**). This discrepancy likely reflects the immunodominance of epitope B with respect to antibody neutralization in the human population, which imposes strong positive selection for mutations at sites within the region [15, 131, 21]. Therefore, variability observed in natural sequences depends on both the extent of immune pressure at a site as well as constraints on HA function.

The deep mutational scanning also showed that nearly all mutations to the highly conserved fusion loop at sites 330-350 are strongly deleterious to cell entry (**Figure 3.1F**, **Figure 3.6**), consistent with the region's key role in mediating membrane fusion and also with prior deep mutational scanning on HAs from other viral subtypes [162, 36, 91, 185, 26, 180]. Taken together, we have measured the effects of nearly all mutations to a recent H3N2 HA on cell entry; these measurements help explain the functional constraints on receptor binding, the general plasticity of antigenic regions, and the mutational constraint of the fusion loop.

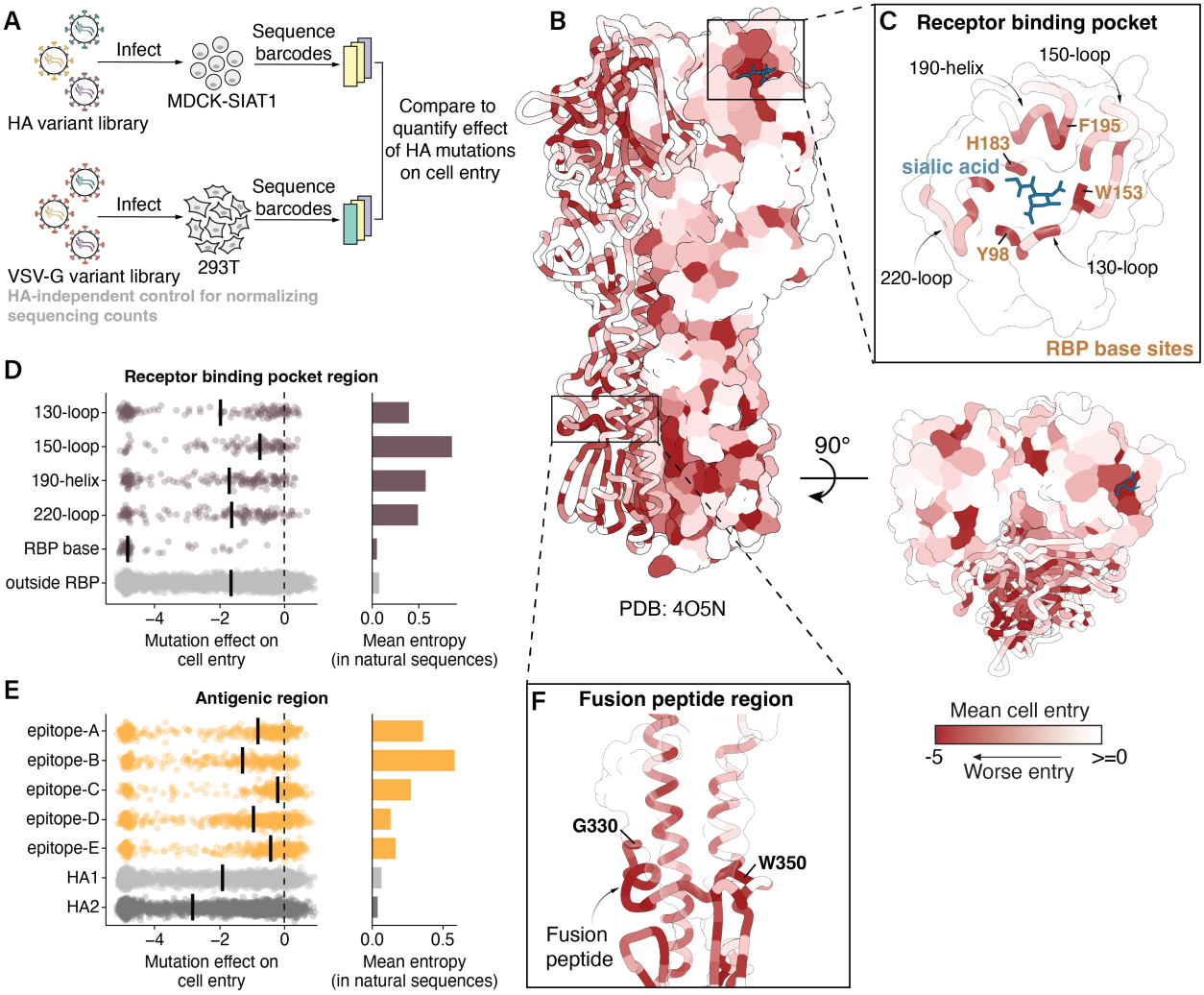

Figure 3.1: **Mutation effects on HA-mediated cell entry.** See full caption on next page.

Mutation effects on HA-mediated cell entry. A) To measure how all HA mutations affect cell entry, we create libraries of barcoded pseudoviruses expressing different HA mutants on their surface (**Figure 3.5**). We use deep sequencing to quantify the ability of each HA mutant to enter cells, normalizing the sequencing counts to a copy of the pseudovirus library where all virions express VSV-G and so do not rely on HA for cell entry. The effect of each mutation is quantified as the log2 of its frequency relative to unmutated variants in the HA condition relative to the VSV-G condition, so negative values indicate impaired cell entry. The mutation effects we report are the median of four measurements, two technical replicates for each of two independently generated biological replicate libraries (**Figure 3.7A**). B) Mean effect of mutations at each site on cell entry mapped onto the HA structure (Protein Data Bank 4O5N) viewed from the side or top, with darker red indicating worse cell entry. See **Figure 3.6** for a heatmap of all mutation effects. C) Zoomed in version of the structure showing the receptor binding pocket. Distribution of mutation effects on cell entry in D) receptor binding pocket regions and E) antigenic regions, with the median effect in each region indicated with a solid black line. The mean Shannon entropy of all sites in each region across a subsampled tree of natural human H3N2 evolution since 1968 is shown on the right. F) Zoomed in version of structure showing sites that make up the fusion peptide and periphery.

3.3.3 Mutation effects on HA acid stability

We next used deep mutational scanning to measure the effects of mutations on HA's acid stability (**Figure 3.2A-B**, **Figure 3.9**, and interactive heatmaps at https://dms-vep.org/Flu_H3_Massachusetts2022_DMS/acid_stability.html). A negative effect indicates the mutation makes the HA less stable (more susceptible to inactivation at acidic pH). Again, we obtained highly correlated measurements between library replicates (r = 0.9, **Figure 3.7B**). Note we could only measure effects on stability of mutations that retained at least some minimal cell entry function (**Figure 3.7C**). We validated the deep mutational scanning measurements of stability effects for a subset of mutations with varying effects using conditionally replicative influenza virions; the effects measured in the deep mutational scanning concord well with those measured in the validation assays using influenza virions (**Figure 3.4D**). Importantly, the effects of mutations on acid stability are not strongly correlated with the effects of mutations on cell entry, indicating these assays capture distinct molecular phenotypes (**Figure 3.3D**). The phenotypes are distinct for several reasons. First, comparison of natural influenza strains shows that HAs can have acid stabilities that span an appreciable range (e.g., fusion pH of 5.0-5.5 in human seasonal strains vs. fusion pH of 5.6-6.0 in avian influenza strains [163, 136, 50]) but still effectively mediate entry in cells in the lab, demonstrating that a range of stabilities are compatible with entry into cell lines even if evolutionary selection for transmissibility in actual human or avian hosts favors a tighter stability range. Second, many mutations that impair cell entry disrupt HA folding, receptor binding, or fusion-mediating conformational changes in a manner that is unrelated to acid stability.

Most mutations that affect acid stability destabilize HA (**Figure 3.2B**, **Figure 3.9**). The mutations that most strongly affect stability tend to occur in structural regions that participate in the irreversible HA conformational changes that occur during membrane fusion (**Figure 3.2C**) [10]. During this process, the HA1 protomers dilate and eventually dissociate [10, 53, 76, 132]. Mutations at sites 165, 167, 205, and the 220-loop located in the trimer interface are often destabilizing, likely because they weaken interactions among neighboring monomers (**Figure 3.2D**). Notably, site 165 carries a high-mannose N-linked glycan that packs against the 220-loop of a neighboring monomer [124] and all mutations to sites 165 or 167 destabilize except T167S, the one mutation that preserves the glycan (**Figure 3.2E**). Positively charged arginine residues at sites 220 and 229 are thought to stabilize this region via electrostatic interactions [104], and indeed mutations at these sites destabilize HA (**Figure 3.9**).

As HA1 dissociates, the HA1-HA2 interface undergoes conformational changes that are largely driven by intramonomer interactions. Consistent with prior work [132], a tetrad salt bridge involving sites 89, 109, 269 of HA1 and 396 of HA2 is important for HA stability (**Figure 3.2F**, **Figure 3.9**). Mutations at site 269 that preserved the net charge did not affect stability, but substituting an opposing charged residue was destabilizing (**Figure 3.2G**, **Figure 3.9**). Interestingly, charge-preserving mutations to K or H at site

R109 were destabilizing, albeit less so than mutation to an oppositely charged E, suggesting the longer R109 side chain may also play a role in stability.

At acidic pH, the short α-helix, interhelical loop, and long α-helix of HA2 form an extended coil (**Figure 3.2C**) [10, 18]. In the prefusion conformation, these regions feature some of the largest structural differences between influenza subtypes [51]. The H3/H4/H14 clade-specific G at site 404 in the interhelical loop creates a unique sharp turn that is stabilized in part by a clade-specific S at site 107 [51]. As expected, mutations at these sites and in the interacting periphery tend to destabilize HA, indicating the fragile yet essential balance governing this region (**Figure 3.2H**, **Figure 3.9**). In summary, we have produced a comprehensive high-throughput map of mutation effects on H3 acid stability; this map provides insight into the structural principles governing H3 HA stability and its conformational transitions.

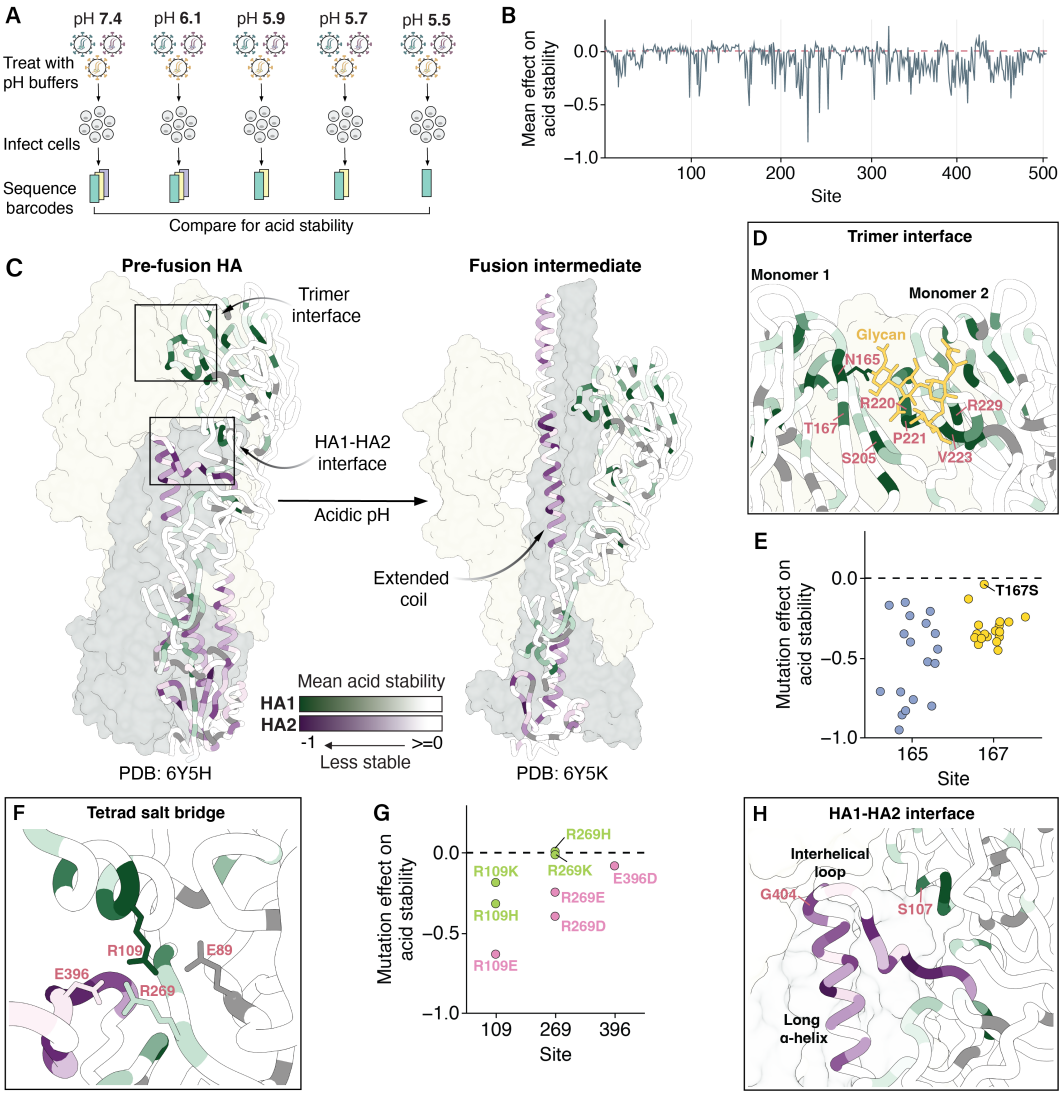

Figure 3.2: **Mutation effects on HA acid stability.** See full caption on next page.

Mutation effects on HA acid stability. A) We incubated pseudovirus HA variants in different acidic pH buffers prior to infection and sequenced the pseudovirus barcodes within cells after infection. To quantify mutation effects on acid stability, we compared these barcode counts to those of pseudoviruses treated with neutral pH media, which served as an infection baseline. The mutation effects we report are the median of two biological replicates (**Figure 3.7B**). B) Mean effect of mutations at each site on acid stability. Negative values indicate sites where mutations decrease stability (e.g., lead to viral inactivation at a higher pH). See **Figure 3.9** for a heatmap of all mutation effects. C) Mean effect of mutations at each site on acid stability mapped onto the structures of pre-fusion (Protein Data Bank 6Y5H) and fusion intermediate (Protein Data Bank 6Y5K) HAs, with darker shades of green and purple indicating greater destabilizing mutation effects in HA1 and HA2, respectively. Dark gray indicates sites where no mutation effects on acid stability were measured due to all mutations at these sites strongly impairing cell entry. D) Zoomed in view of the trimer interface, with the same color scale used in C. E) Mutation effects on acid stability at sites 165 and 167. F) Zoomed in view of sites that participate in a tetrad salt bridge, with the same color scale used in C. G) Mutation effects of charged amino acids at sites that participate in the tetrad salt bridge. H) Zoomed in view of the HA1-HA2 interface, with the same color scale used in C.

3.3.4 Mutations exhibit phenotype-specific entrenchment

Having characterized the effects of mutations to HA on cell entry and acid stability in the background of a recent H3N2 HA, we next explored whether these effects have changed over the last few decades of evolution. To do this, we retraced mutations that swept to fixation in the past (**Figure 3.3A**). During a sweep at a site, both the ancestral amino acid and the descendant amino acid are expected to be functionally tolerated. However, over time the descendant strains may lose tolerance for the ancestral amino acid due to other mutations that become contingent on the current amino acid, a form of epistasis called entrenchment [182, 140, 130].

The effects of many mutations on cell entry in the receptor binding pocket have become entrenched over time (**Figure 3.3B**). For instance, a mutation at site 195 from Y to F emerged in 2020 and swept to fixation among human H3N2 strains, but the reversion F195Y in the MA22 background is highly deleterious to cell entry, indicating the mutation of site 195 from Y to F has become entrenched (**Figure 3.3B**). Y195F was recently shown to be a permissive mutation that enabled the fixation of Y159N and T160I (**Figure 3.10**), which confer antigenic benefits and expand receptor specificity in the presence of 195F but impair receptor binding when paired with 195Y [97, 174, 13]. As the MA22 HA contains 159N and 160I, the reversion F195Y is no longer accessible. Similarly, the G186D mutation emerged in 2020 and subsequently swept to fixation; the reversion D186G in the MA22 background is highly deleterious to cell entry, indicating that G186D has become entrenched (**Figure 3.3B**). This observation is also consistent with recent work that found G186D epistatically interacts with D190N, and the pair co-evolved together to preserve receptor binding [93]. We validated that conditionally replicative influenza virions encoding MA22 HA with reversions to each of these entrenched mutations (reversions D186G, S193F, F195Y, and D225N) had over 100-fold decreased titers relative to virions encoding the unmutated MA22 HA (**Figure 3.8B**). Collectively, these results along with prior work [184, 181, 179, 97], highlight the existence of extensive epistasis with respect to the effects of mutations within the HA receptor binding pocket on cell entry. This epistasis restricts access to ancestral amino acids and simultaneously opens new evolutionary paths for antigenic change (e.g., 159N, G186D). However, not all mutations become entrenched, since reversions to ancestral amino acids are observed in HA evolution. Therefore, analysis of entrenchment reveals which reversions are currently accessible or constrained.

In contrast to the extensive epistatic entrenchment involving mutations in the receptor-binding pocket with respect to cell entry, we saw little evidence of entrenchment with respect to cell entry involving mutations in other regions of HA. Nearly all reversions to ancestral amino acids at sites outside of the receptor binding pocket are well tolerated with respect to cell entry with the single exception of T248N (**Figure 3.3B**). Interestingly, the N248T mutation that fixed in the 1980s created an N-linked glycan at N246 that has been maintained ever since. T248S (which is the only mutation that retains this glycan) is

noticeably more tolerated than other mutations at sites 246 and 248 (**Figure 3.6**), indicating the glycan is now entrenched. In H3N2 HA evolution, glycosylation near the receptor binding pocket can shield epitopes from antibodies, but often imposes a fitness cost [30]. Therefore, the N248T mutation—which is located near the receptor binding pocket—was likely selected by antigenic pressure, and mutations that compensated for or became dependent on the glycan led to its entrenchment.

Strikingly, the effects of mutations on acid stability have not become entrenched in any region of HA. Reversions to ancestral amino acids at sites inside and outside of the receptor binding pocket remain well tolerated with respect to acid stability with the single exception of the mildly destabilizing reversion A163V (**Figure 3.3B**). Sites where many mutations destabilize HA tend to have conserved amino-acid identities across all natural human H3N2 sequences, which further suggests constraints on acid stability may be constant across genetic backgrounds (**Figure 3.11A**). At the destabilizing sites that do show variation among natural sequences (e.g., sites 219 and 223), the natural mutations are exclusively the particular amino-acid changes that do not affect stability (**Figure 3.11B-D**). Therefore, it appears that while epistasis commonly shifts the effects of HA mutations on cell entry to entrench mutations, such epistatic processes are much rarer with respect to the phenotype of HA acid stability.

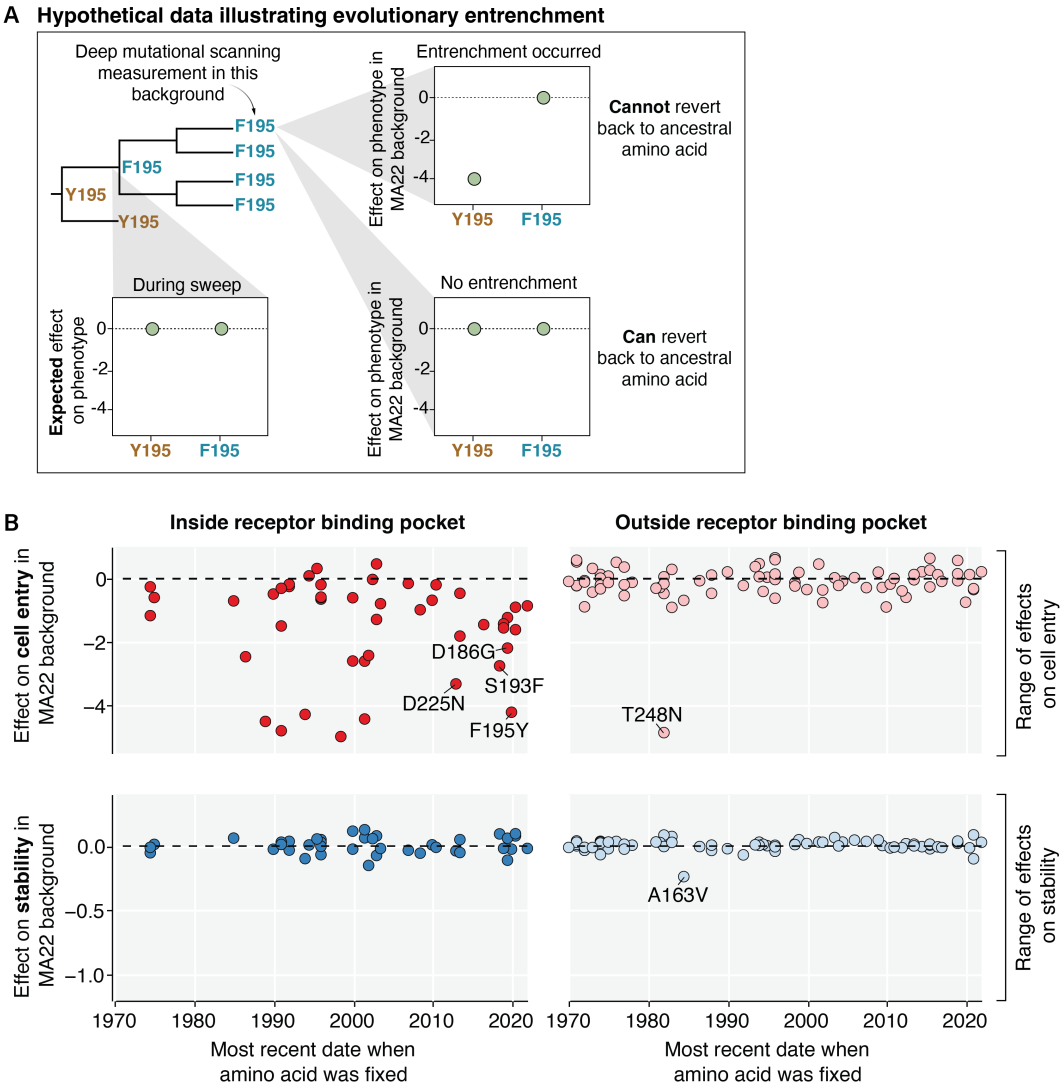

Figure 3.3: **Mutations exhibit phenotype-specific epistatic entrenchment.** See full caption on next page.

Mutations exhibit phenotype-specific epistatic entrenchment. A) Hypothetical data illustrating entrenchment of a mutation via epistasis. The phylogenetic tree shows a sweep of F replacing Y at site 195. During the sweep, both F and Y are expected to be tolerated. However, the effect of reverting to the ancestral amino acid (Y) may change over time due to entrenchment. The HA used for deep mutational scanning contains the current amino acid (F) at site 195. If entrenchment occurred, then reverting to the ancestral amino-acid Y195 will be deleterious in the recent genetic background used for deep mutational scanning. In the absence of entrenchment, Y195 remains tolerated in newer genetic backgrounds. B) Actual experimental data showing the effects of reversions to all ancestral amino acids that were previously fixed in human H3N2 strains since 1968 on HA-mediated cell entry (top row) or HA acid stability (bottom row) as measured in the deep mutational scanning on the MA22 HA. Mutations are placed on the x-axis by the most recent date that the ancestral amino acid was fixed, and the panel columns indicate whether the mutation is at a site inside (left column) or outside (right column) of the receptor binding pocket. The range of the y-axis for each phenotype is set to span the range of effects of all mutations to HA (not just those that fixed during natural H3N2 evolution) in the deep mutational scanning. There is extensive epistatic entrenchment of mutations in the receptor binding pocket with respect to cell entry, but no substantial entrenchment of mutations with respect to stability. To mouseover the individual mutations, see https://dms-vep.org/Flu_H3_Massachusetts2022_DMS/entrenchment.html for an interactive version of this plot.

3.3.5 Epistasis can alleviate the effects of antigenic mutations that impair cell entry but not stability

Phenotypes like cell entry and acid stability help determine which HA mutations are tolerated, but immune pressure largely drives positive selection for mutations in HA during the evolution of human influenza viruses. To define this immune pressure on the MA22 HA, we used deep mutational scanning to measure how HA mutations affected neutralization by human sera collected in 2023 from four children born between 2009 and 2021 (**Figure 3.4A**, **Figure 3.12A-D**, and interactive heatmaps at https://dms-vep.org/Flu_H3_Massachusetts2022_DMS/sera_neutralization.html). We used children sera since children may play an especially important role in driving influenza evolution [174, 135]. The deep mutational scanning measurements are quantified such that a positive effect indicates the mutation confers viral escape from serum neutralization, whereas a negative effect indicates the mutation sensitizes the virus to neutralization by the serum. To complement these results, we also used a sequencing-based method [78, 101] to measure neutralization titers for each sera against 78 H3N2 strains that either circulated in humans or were included in vaccines between 2012 and 2023.

Our deep mutational scan revealed mutations at site K140 in the MA22 HA increase sensitivity to neutralization (**Figure 3.4A**, note the negative escape at site 140). Site 140 is in epitope A of HA, and changed from an I to K in 2022 (**Figure 3.4B**). The fact that many mutations to site 140, including the reversion K140I, are sensitizing (**Figure 3.12C**) suggests that sera contain neutralizing antibodies targeting the ancestral amino-acid identity of I140 that were escaped by the I140K mutation in 2022; the MA22 reversion K140I restores neutralization by these antibodies. We validated that conditionally replicative influenza virions with the MA22 HA carrying a K140I reversion increased sensitivity to neutralization in two of the three sera predicted to contain 140I-specific antibodies by the deep mutational scanning (**Figure 3.4C**, **Figure 3.13A-B**). For those sera, neutralization of historic and vaccine strains differing by up to 34 amino acids from MA22 could also be explained by site 140, though we cannot rule out the influence of other historical mutations (**Figure 3.13C**). Taken together, these results indicate 140I-specific antibodies contribute substantially to the neutralizing antibody activity of sera from some individuals, and suggest that the I140K mutation that fixed in 2022 was likely selected by this immune pressure.

Given that changing site 140 from I to K causes such an appreciable reduction in antibody neutralization for some sera, why did this mutation not spread widely in human H3N2 influenza until 2022 (**Figure 3.4B**)? At least part of the answer appears to be that the I140K mutation was highly deleterious for the cell entry function of HAs from older strains: for instance, I140K causes a nearly 40-fold drop in the titers of conditionally replicative influenza virions encoding the HA from the older A/Perth/16/2009 (H3N2) strain, whereas interchanging I and K at site 140 in the MA22 HA has little impact on the titers (**Fig-**

ure 3.4D). These observations suggest I140K was evolutionarily inaccessible in 2009 due to its strongly negative effect on HA's cell entry function, and could not be positively selected until a permissive HA genetic background emerged. This finding parallels the recent demonstration by Lei et al.[93] that G186D and D190N, two mutations that co-evolved together in 2020, are individually deleterious to receptor binding but together restore this function and lead to escape from human sera. Collectively, these results indicate that epistasis can alleviate pleiotropic constraints on cell entry function and facilitate antigenic evolution.

We next examined whether we could identify pleiotropic constraints on other mutations that affect serum neutralization of the MA22 HA. Mutations at a variety of HA sites reduce serum neutralization, including sites 145, 165, 189, 205, 220, and 229 (**Figure 3.4A**, note positive escape at these sites). In the absence of other constraints, one might expect recent evolution to select for neutralization escape mutations at these sites. In some cases, this is occurring: S145N and K189R are single nucleotide accessible mutations from MA22 that cause sera escape in the deep mutational scanning (**Figure 3.4E**, **Figure 3.13D**) and both have been increasing in frequency among human H3N2 sequences since 2024 (**Figure 3.4B**). However, some of the sites that strongly escape sera neutralization show no variation over decades of H3N2 HA evolution. For instance, mutations at sites 165, 205, 220, and 229 cause strong serum escape in the deep mutational scanning (**Figure 3.4A,E**) and in validation assays with conditionally replicative influenza virions (**Figure 3.4F**), but these sites have not changed during natural HA evolution (**Figure 3.4B**). This disparity between the abundance of single nucleotide accessible escape mutations identified by deep mutational scanning and their absence in natural human H3N2 sequences suggests pleiotropic constraints could be constraining evolution at these sites. Notably, many of the escape mutations at these sites destabilize HA in our deep mutational scanning (**Figure 3.4E**), even if they are not directly deleterious for HA-mediated cell entry. For instance, the serum escape mutations N165H, S205Y, R220T, and R229I are all roughly neutral with respect to HA-mediated cell entry (**Figure 3.8B**), yet mutations at these sites strongly destabilize HA, making it more sensitive to acid inactivation (**Figure 3.8D**) while conferring escape from sera in independent neutralization assays. Therefore, the effects of mutations on HA's acid stability may impose a strong pleiotropic constraint on its evolution, even when these mutations have no apparent effect on HA-mediated cell entry.

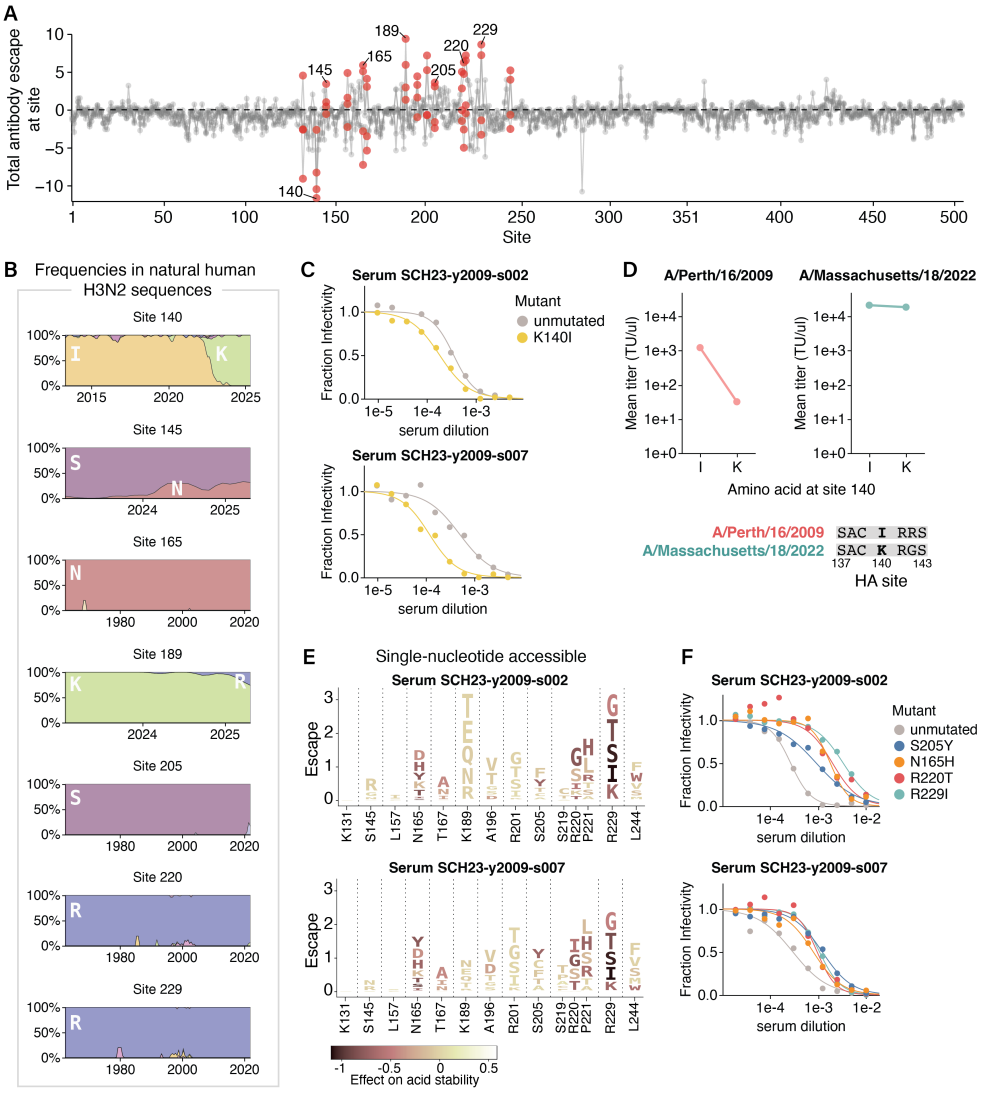

Figure 3.4: **During H3N2 evolution, epistasis alleviates the effects of antigenic mutations that impair cell entry but not stability.** See full caption on next page.

During H3N2 evolution, epistasis alleviates the effects of antigenic mutations that impair cell entry but not stability. A) Sum of mutation effects at each site in the MA22 HA on escape from four human sera collected in 2023. Key sites of escape or sensitization included in logoplots are colored red, and sites where escape mutants were validated in independent neutralization assays are labeled with text. See **Figure 3.12** for data for individual sera. B) Frequencies of amino acids observed in natural human H3N2 HA sequences over time (x-axis indicates year) for several key sites. Note the x-axis range varies as some subplots show changes in recent evolution, while others show conservation across decades of evolution. C) Neutralization by two human sera of conditionally replicative influenza virions with MA22 HA with or without the mutation K140I. Each point is the mean of two technical replicates. D) Titers of conditionally replicative influenza virions with HA from either A/Perth/16/2009 or MA22 with either an I or a K amino acid at site 140. Each point is the mean of four titer measurements, two technical replicates from the same virion rescue stock and two biological replicate stocks rescued from independent plasmid preparations. E) Logoplots displaying amino-acid mutations to the MA22 HA that are accessible by single nucleotide changes. The height of each letter is proportional to the escape from the indicated serum as measured by deep mutational scanning. Each mutation is colored by its effect on HA acid stability as measured in the deep mutational scanning, with darker colors indicating decreased stability. F) Neutralization of conditionally replicative MA22 virus with destabilizing mutations by the two sera in E. Each point is the mean of two technical replicates.

3.4 Discussion

The extent to which pleiotropic conflicts constrain evolution of H3N2 HA has remained unclear. Here, we measured the effects of all amino acid mutations to a recent H3 HA on cell entry, acid stability, and neutralization by serum antibodies. Interpreting these effects in the context of HA's natural evolution reveals that recent H3N2 evolution has alleviated constraints on cell entry through epistasis, but some antigenic mutations with no effect on cell entry remain highly constrained because they pleiotropically decrease acid stability.

Other studies have reported epistatic entrenchment to be common with respect to the impact of HA mutations within the receptor binding pocket on viral replication [184, 181, 179, 93, 97]. Our work also finds that HA mutations in the receptor binding pocket have become entrenched with respect to their effects on cell entry, but this pattern is observed much less often for HA mutations outside of the receptor binding pocket. Furthermore, epistatic entrenchment with respect to acid stability is absent across the entire HA during the timeframe we analyzed, demonstrating how epistasis can be phenotype-specific. Why might mutation effects on acid stability be less prone to shift due to epistasis? A variety of studies have found that mutations to proteins often have roughly additive effects on stability [173, 191], and epistasis at the level of function tends to arise from the non-linear relationship between stability and function rather than underlying epistasis in the effects of mutations on stability [54, 12]. In contrast, the receptor binding pocket involves a network of amino acid residues positioned so that their side chains interact with sialic acid via hydrogen bonds and other non-covalent contacts. Mutations at one site can alter these interactions in ways that modify the effects of changes at interacting sites [184, 181, 179, 93, 161, 97], providing a structural basis for extensive epistasis with respect to cell entry. In a more abstract view, acid stability could represent a single underlying "global" biophysical property that is less influenced by epistasis [121, 110], whereas cell entry is a higher order phenotype that involves several underlying properties (e.g., receptor-binding, protein stability, and membrane fusion). There is evidence for other proteins that mutations often have additive effects on underlying biophysical properties, and epistasis in higher-order phenotypes often arises simply from their non-linear dependence on underlying molecular properties [121, 138, 137, 110].

Our deep mutational scanning shows that there are sites outside classically defined antigenic regions where mutations strongly escape serum antibody neutralization but also destabilize HA (e.g. sites 165, 205, 220, and 229). Interestingly, these sites are highly conserved and located in the trimer interface. While non-neutralizing anti-H3 and neutralizing anti-H7 antibodies targeting this region have been described [192, 164, 170, 7], to our knowledge, humans have not been shown to possess neutralizing anti-H3 trimer interface antibodies. While it is unclear how these mutations reduce serum antibody neutralization, we

speculate there are two possible mechanisms. These mutations could abrogate binding of antibodies that directly target the trimer interface, nearby epitopes, or across protomers [70]. Alternatively, the destabilizing effect could accelerate membrane fusion, a previously reported strategy for antibody escape [20]. In any case, our work suggests antibodies targeting these sites may be particularly difficult to escape due to strong pleiotropic constraints on destabilizing mutations during HA evolution.

Overall, our study highlights how mutations to HA often have pleiotropic effects. The extent to which pleiotropic constraints can be alleviated by epistasis differs across phenotypes: for example, constraints on cell entry appear more readily alleviated than constraints on acid stability in recent H3N2 influenza HA evolution. Whether these constraints similarly shape the evolution of other H3N2 strains and influenza subtypes remains to be determined. A deeper understanding of how pleiotropy and epistasis shape HA evolution will be useful for forecasting viral evolution and designing therapeutics that are resistant to viral escape.

3.5 Supplementary Material

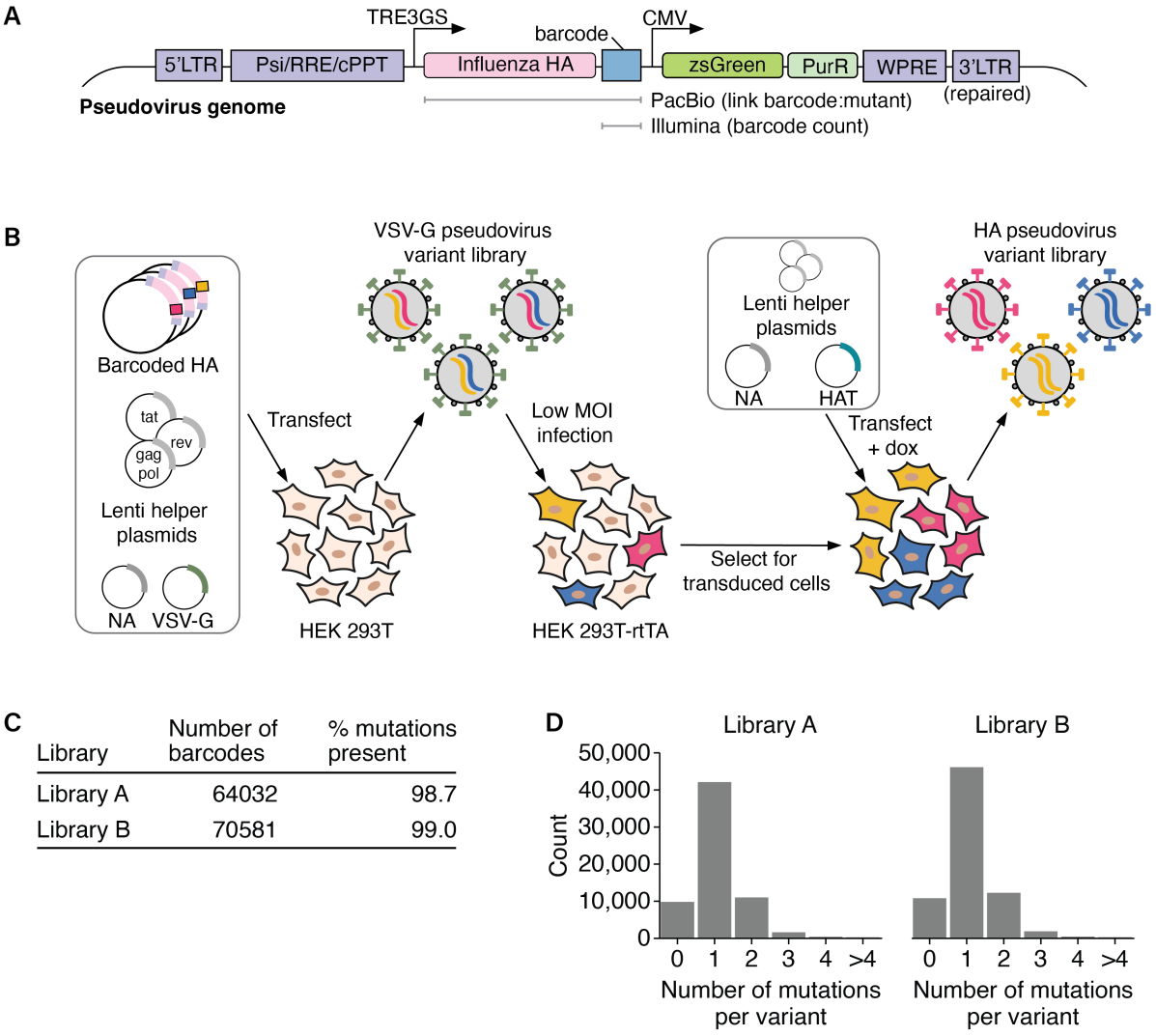

Figure 3.5: **Pseudovirus deep mutational scanning of influenza hemagglutinin.** See full caption on next page.

Pseudovirus deep mutational scanning of influenza hemagglutinin. A) Diagram of the lentiviral genome used to produce genotype-phenotype-linked pseudovirus libraries for deep mutational scanning. The genome is flanked by long terminal repeat (LTR) sequences, with the typical 3' LTR deletion repaired so the lentiviral genome can be transcribed after integration. A zsGreen reporter and a puromycin resistance marker are constitutively expressed from a CMV promoter. Expression of the HA gene is regulated by a doxycycline inducible TRE3GS promoter. PacBio sequencing is performed to map each barcode to an HA mutant. Then, effects of HA mutations can be quantified by Illumina sequencing the barcodes. B) Schematic of the "two-step" method for generating genotype-phenotype-linked pseudovirus libraries described in Dadonaite et al. [29, 26]. In the first step, a plasmid library encoding the lentiviral genomes with the HA mutants is co-transfected into HEK293T cells alongside three lentiviral helper plasmids (tat, rev, gagpol), a plasmid expressing a strain-matched neuraminidase (NA), and a plasmid expressing the glycoprotein from vesicular stomatitis virus (VSV-G). This results in pseudoviruses that encode HA mutants within their genomes but express VSV-G and NA on their surfaces. The NA ensures HA expression does not prevent virions from detaching from producing cells. These VSV-G pseudotyped viruses are transduced into a HEK293T-rtTA cell line at low MOI to ensure most infected cells integrate a single lentiviral genome, and puromycin is used to select for integrated cells. In the second step, helper plasmids, a plasmid expressing NA, and a plasmid expressing the HA-activating human airway trypsin-like (HAT) protease are co-transfected into the integrated cells. Doxycycline is added at this step to induce HA expression. This results in genotype-phenotype-linked HA-pseudotyped pseudoviruses. These pseudoviruses can undergo a single round of cell entry, but are not fully infectious agents as they do not encode the genes needed to undergo multiple rounds of replication. C) Number of barcodes and mutation coverage in the two pseudovirus library replicates. In this table, "% mutations present" indicates the percentage of all HA ectodomain amino-acid mutations found in at least one of the barcoded variants. D) Distribution of the number of HA amino-acid mutations per variant in the two pseudovirus library replicates. Most variants contain a single mutation.

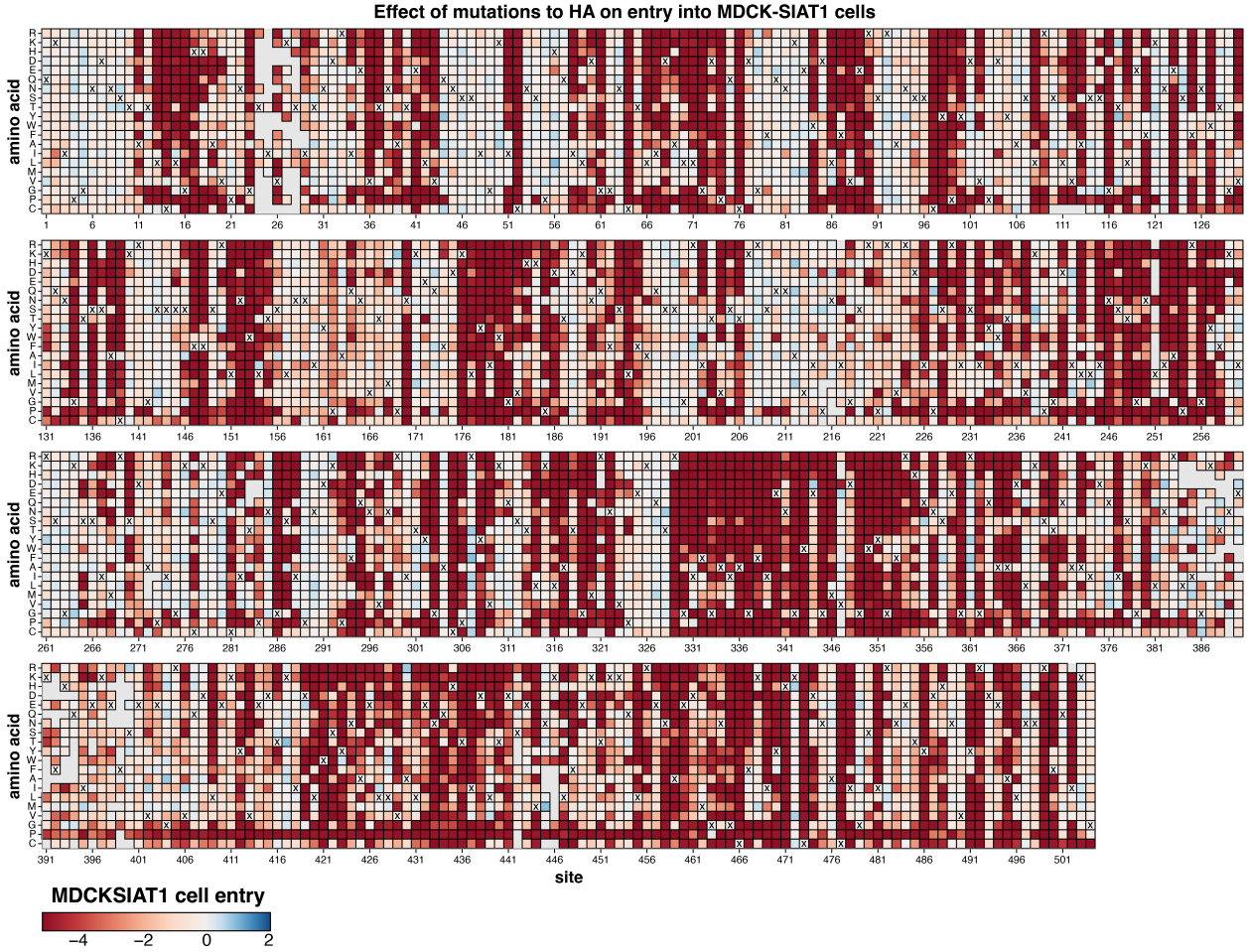

Figure 3.6: **Mutation effects on HA-mediated cell entry.** Each tile represents a mutation at an HA site, colored by the effect of that mutation on entry into MDCK-SIAT1 cells. Red indicates impaired entry, white indicates no effect, and blue indicates improved entry. To visualize these mutation effects in the context of the HA structure, see **Figure 3.1B**. Tiles with an 'X' denote the amino acid identity in the unmutated MA22 strain. Empty gray tiles indicate mutations that were either missing from the library or lacked a reliable cell entry measurement. See https://dms-vep.org/Flu_H3_Massachusetts2022_DMS/cell_entry.html for an interactive version of this heatmap.

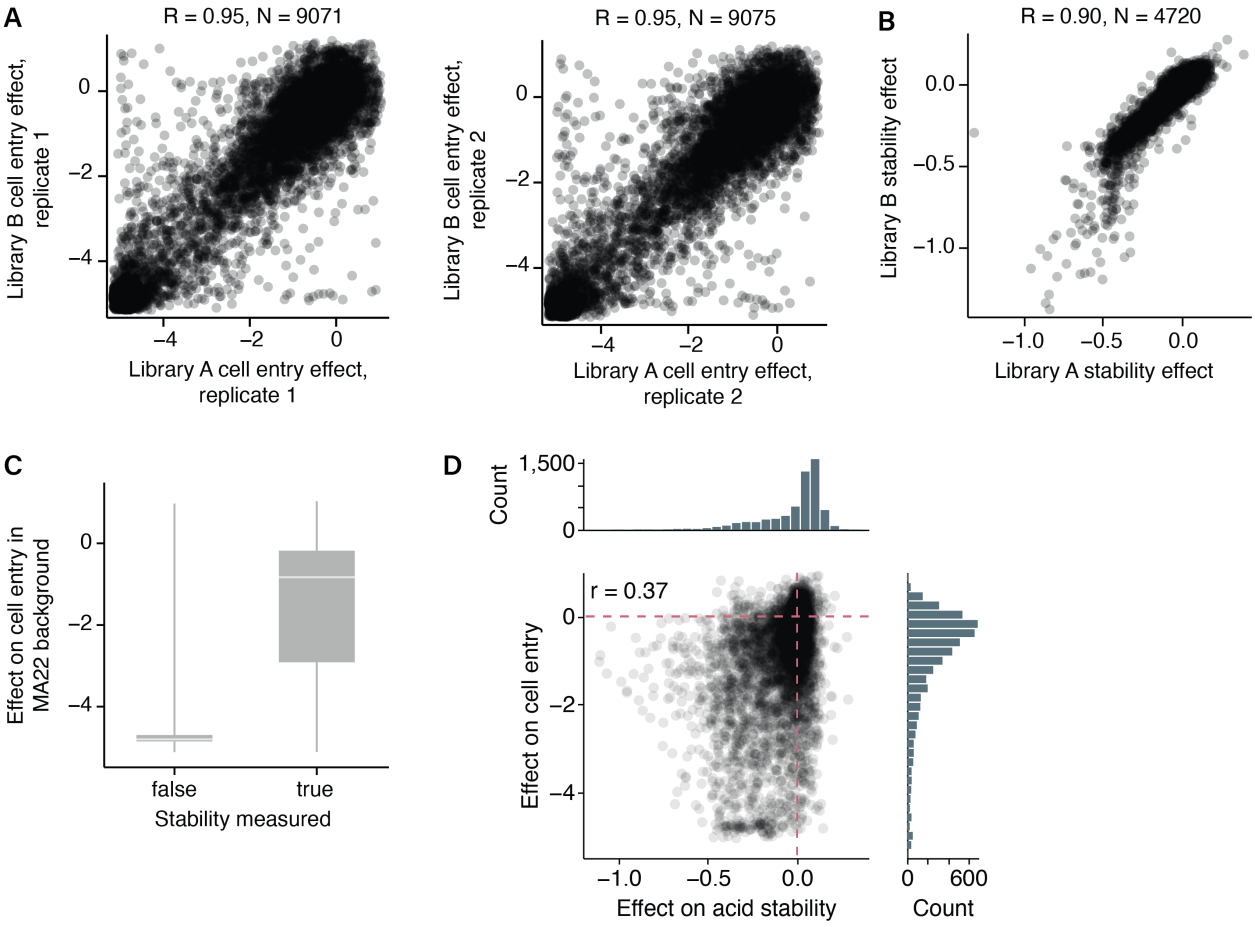

Figure 3.7: **Correlations of mutation effects measured by deep mutational scanning.** A) Correlation of the effects of HA mutations on cell entry between the two pseudovirus library replicates. Each point represents the effect of a different mutation as measured in each replicate. Two technical replicates were performed for each of the two libraries, and the two panels show correlations between the two independent libraries for each technical replicate. Throughout this paper, we report the median effect of mutations across the four replicates. B) Correlation of the effects of HA mutations on acid stability between the two pseudovirus library replicates. Note that there are fewer mutations with measured effects on stability because we can only measure stability for mutations with at least some cell entry. C) Most mutations for which it was not possible to make measurements of acid stability correspondingly have very poor cell entry. The center line shows the median effect on cell entry, the box indicates the interquartile range, and the whiskers extend 1.5 x interquartile range beyond the first and third quartiles. D) Correlation between effects of mutations on cell entry and effects of mutations on acid stability. These effects of mutations on these two phenotypes are only weakly correlated.

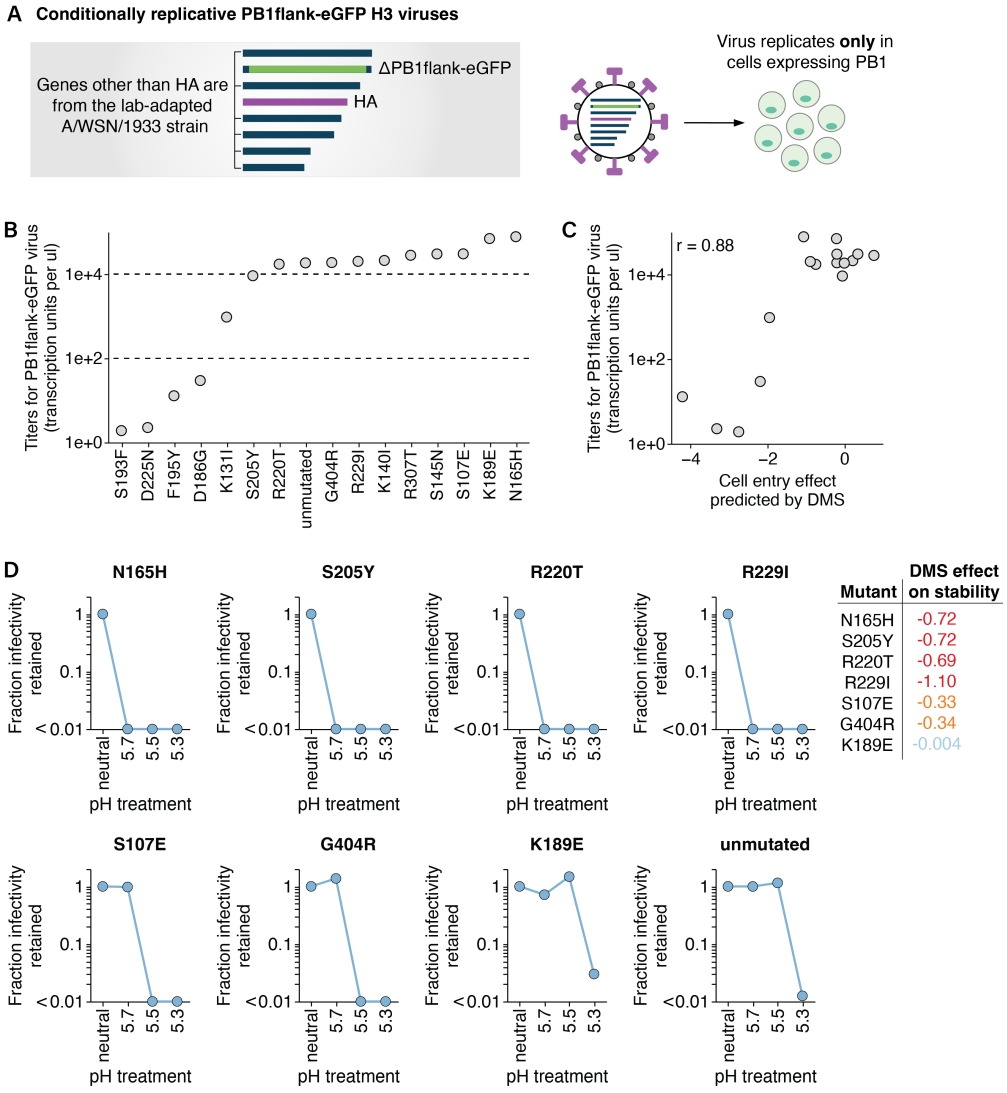

Figure 3.8: **Validation of mutation effects on cell entry and acid stability with conditionally replicative influenza virions.** See full caption on next page.

Validation of mutation effects on cell entry and acid stability with conditionally replicative influenza virions. A) Diagram of a conditionally replicative PB1flank-eGFP influenza virus genome. The PB1 gene is replaced with an eGFP and the remaining segments besides HA are derived from a lab-adapted A/WSN/1933 strain. These viruses can be rescued by reverse genetics, can only replicate in cells that express PB1, and are safe to use at biosafety-level 2. B) Titers of conditionally replicative virions carrying single amino acid mutations in the MA22 HA that were present in the supernatant after virus production by reverse genetics. Each point in the plot is the mean of four titer measurements, two technical replicates from the same virion rescue stock and two biological replicate stocks rescued from independent plasmid preparations. C) Correlation between the titers of conditionally replicative virions carrying single amino acid mutations to the MA22 HA (shown in B) and the effects of those mutations on cell entry measured by deep mutational scanning. D) The fraction infectivity retained after treating conditionally replicative virions with the indicated MA22 HA mutations with either neutral media or acidic pH buffers. The fractions are normalized to the infectivity in the neutral condition. Each point is the mean of two technical replicates performed on different days. The effect of each mutant on acid stability measured by deep mutational scanning is included on the right, and generally tracks with the pH sensitivity measured in the validation assay.

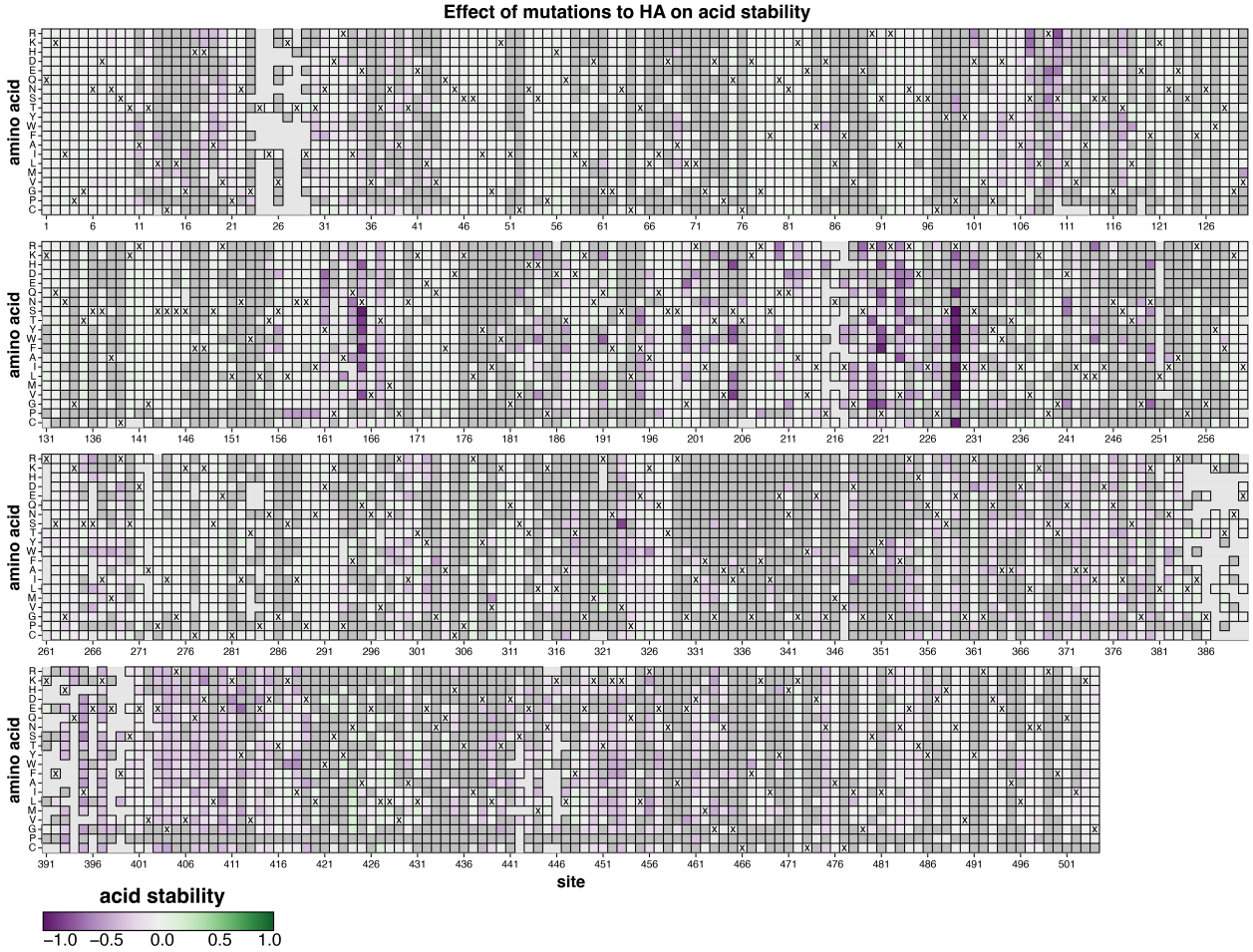

Figure 3.9: **Mutation effects on HA acid stability.** Each tile represents a mutation at an HA site, colored by the effect of that mutation on HA acid stability. Purple indicates decreased stability, white indicates no effect, and green indicates increased stability. To visualize these mutation effects in the context of the HA structure, see **Figure 3.2C**. Tiles with an 'X' denote the amino acid identity in the unmutated MA22 strain. Dark gray tiles indicate mutations that are too deleterious for cell entry to reliably measure their effect on acid stability, while light gray tiles indicate mutations that were missing (not measured) in the library. See https://dms-vep.org/Flu_H3_Massachusetts2022_DMS/acid_stability.html for an interactive version of this heatmap.

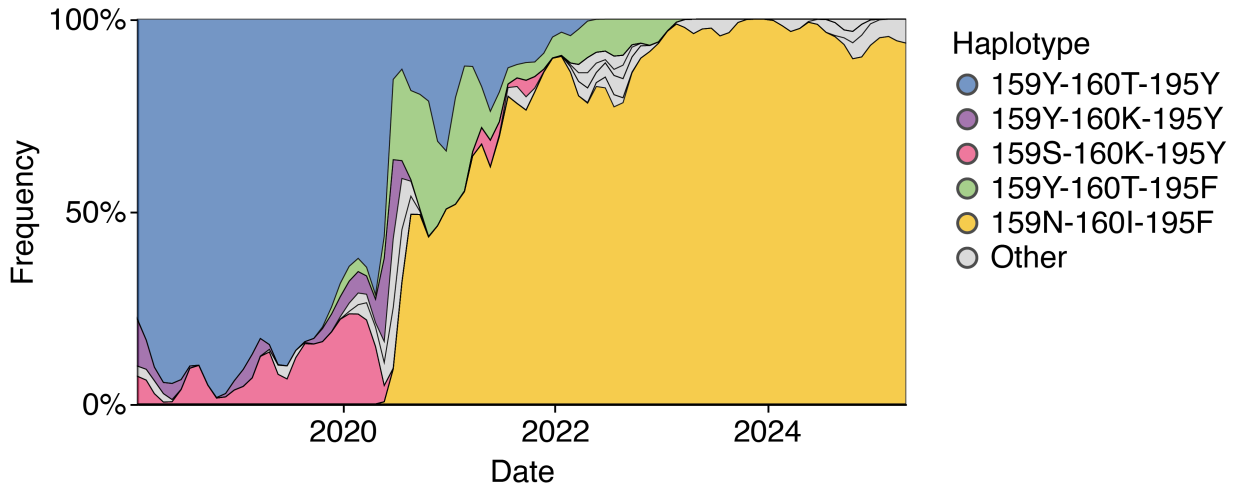

Figure 3.10: **Evolutionary dynamics at sites 159, 160, and 195 in human H3N2 HA.** Muller diagram showing all combinations of amino acids observed at sites 159, 160, and 195 since 2018 in the evolution of the HA from human H3N2 influenza. Haplotypes that reach a frequency >20% at some timepoint are colored according to the key, while other haplotypes are colored gray. Y159N and T160I only arise to fixation in the background of 195F, and this triple mutant lineage (yellow) eventually outcompetes the lineage containing 195F alone (light green).

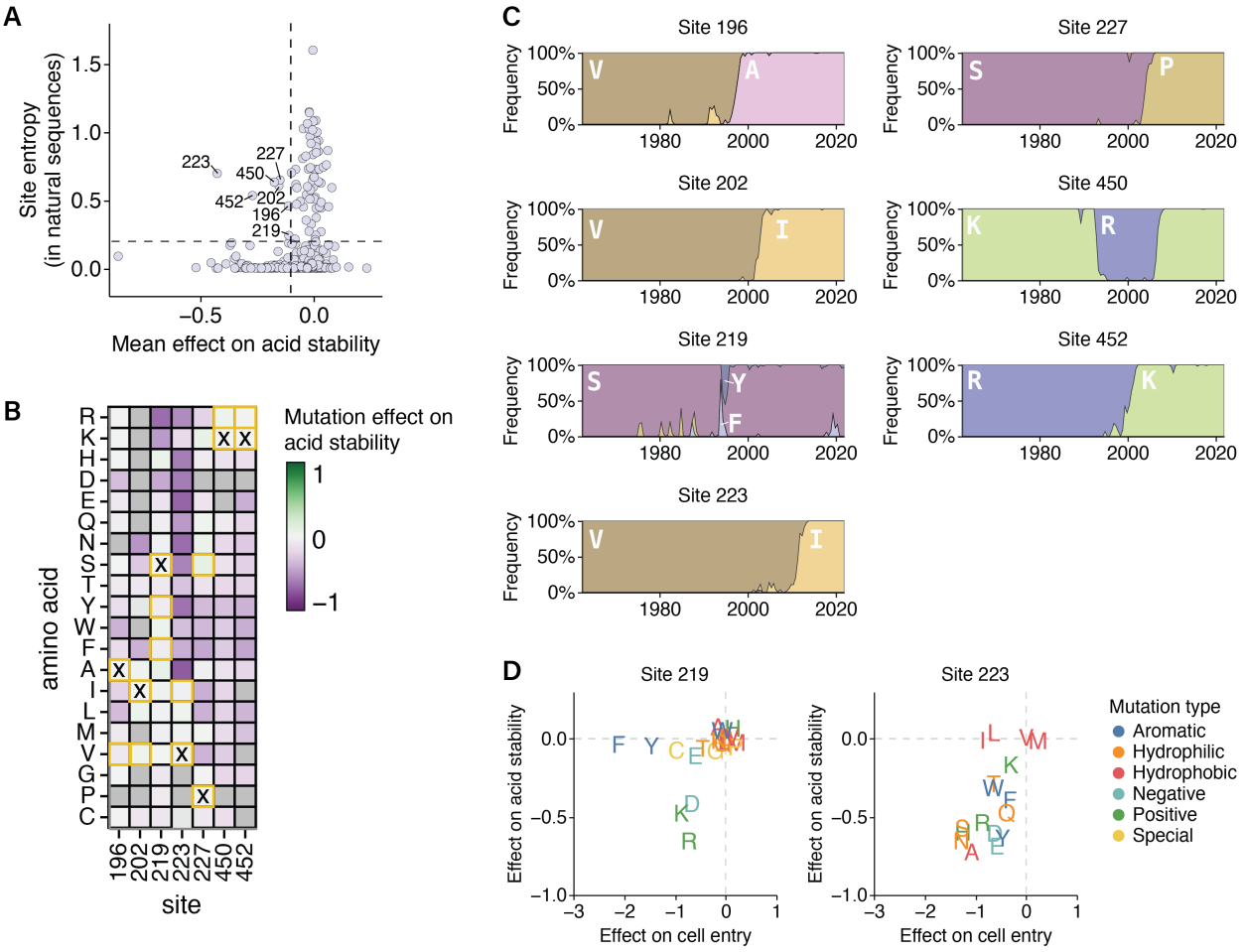

Figure 3.11: **Conservation at HA sites with destabilizing mutations.** A) Correlation between the Shannon entropy at each HA site in an alignment from a subsampled tree of natural human H3N2 evolution since 1968 and the mean effect on acid stability of all mutations at each HA site as measured by deep mutational scanning. Most sites with many mutations that destabilize HA are strongly conserved, with exceptions labeled. B) Heatmap of all mutation effects on acid stability at sites labeled in A. The 'X' indicates the amino acid in the unmutated MA22 HA, and squares boxed in yellow indicate amino acids that increased in frequency during natural evolution. At sites with many destabilizing mutations, natural evolution exclusively samples only the (relatively rare) amino-acid identities that do not destabilize HA. C) Frequencies over time (the x-axis indicates year) of amino acids observed in natural human H3N2 sequences at the sites labeled in A. D) Correlation between mutation effects on acid stability and cell entry at sites 219 and 223. Mutations are colored by biochemical group.

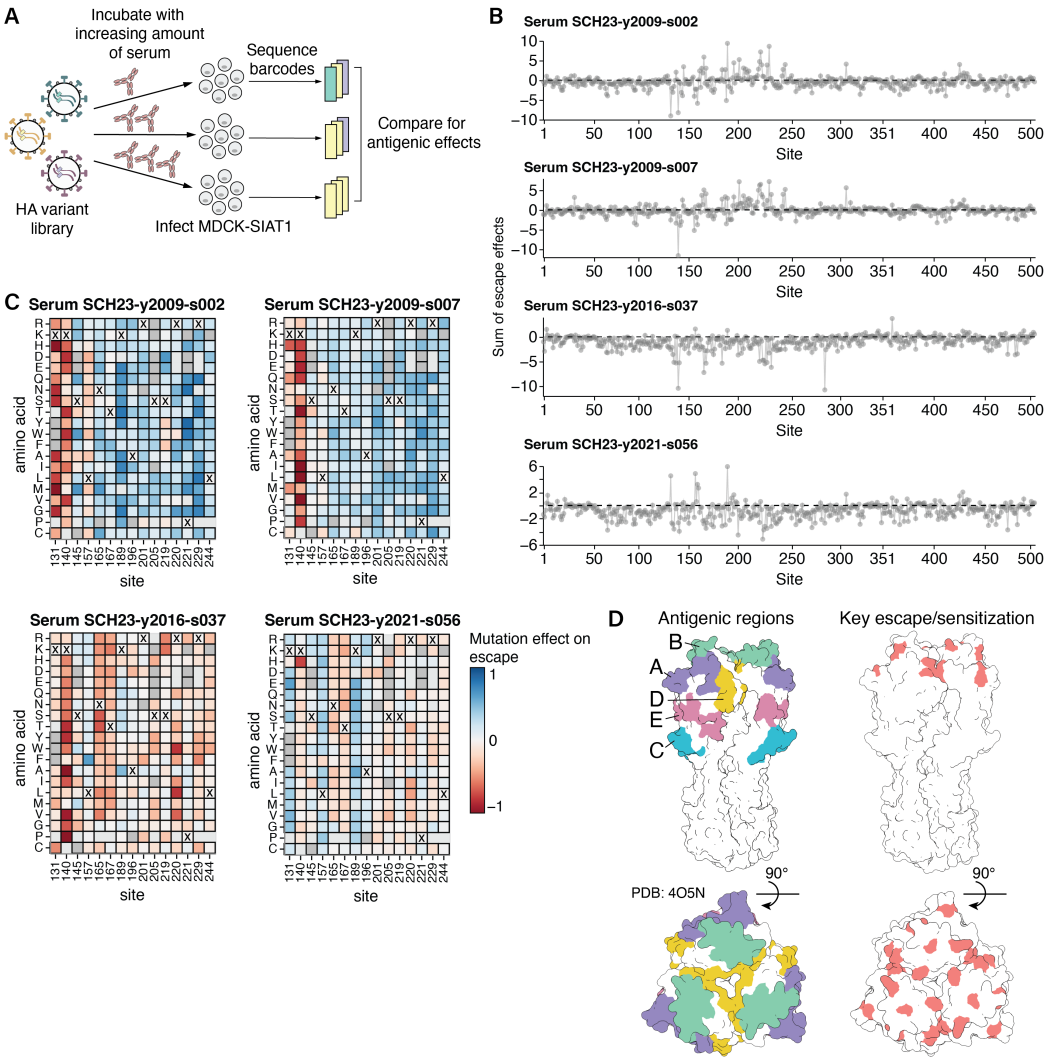

Figure 3.12: **Mapping the effects of HA mutations on neutralization by human sera using deep mutational scanning.** See full caption on next page.

Mapping the effects of HA mutations on neutralization by human sera using deep mutational scanning. A) We incubated the pseudovirus HA library with increasing concentrations of serum, then infected MDCK-SIAT1 cells and sequenced the barcodes of pseudoviruses that were still able to enter cells after serum treatment. To quantify mutation effects on antigenicity, we compared these barcode counts to those of pseudoviruses that were not incubated with serum, which served as an infection baseline; a neutralization standard is used to convert these counts into fraction infectivity at each serum concentration (**Methods**) [29, 26]. The mutation effects we report are the median of two biological replicates. B) The sum of mutation effects on escape at each site in HA for four human sera. **Figure 3.4A** shows these four plots overlaid. See https://dms-vep.org/Flu_H3_Massachusetts2022_DMS/sera_neutralization.html for a version of these lineplots that is interactive, along with interactive heatmaps that show how individual mutations affect sera neutralization. C) Mutation-level escape and sensitization at key sites that are highlighted in **Figure 3.4A** for the four sera. The X's indicate the amino acid in the unmutated MA22 strain. Tiles that are more blue indicate mutations that escape sera, while tiles that are more red indicate mutations that have a sensitizing effect. D) HA structures (Protein Data Bank 4O5N) showing antigenic regions and locations of key sites of escape or sensitization that are highlighted in **Figure 3.4A**.

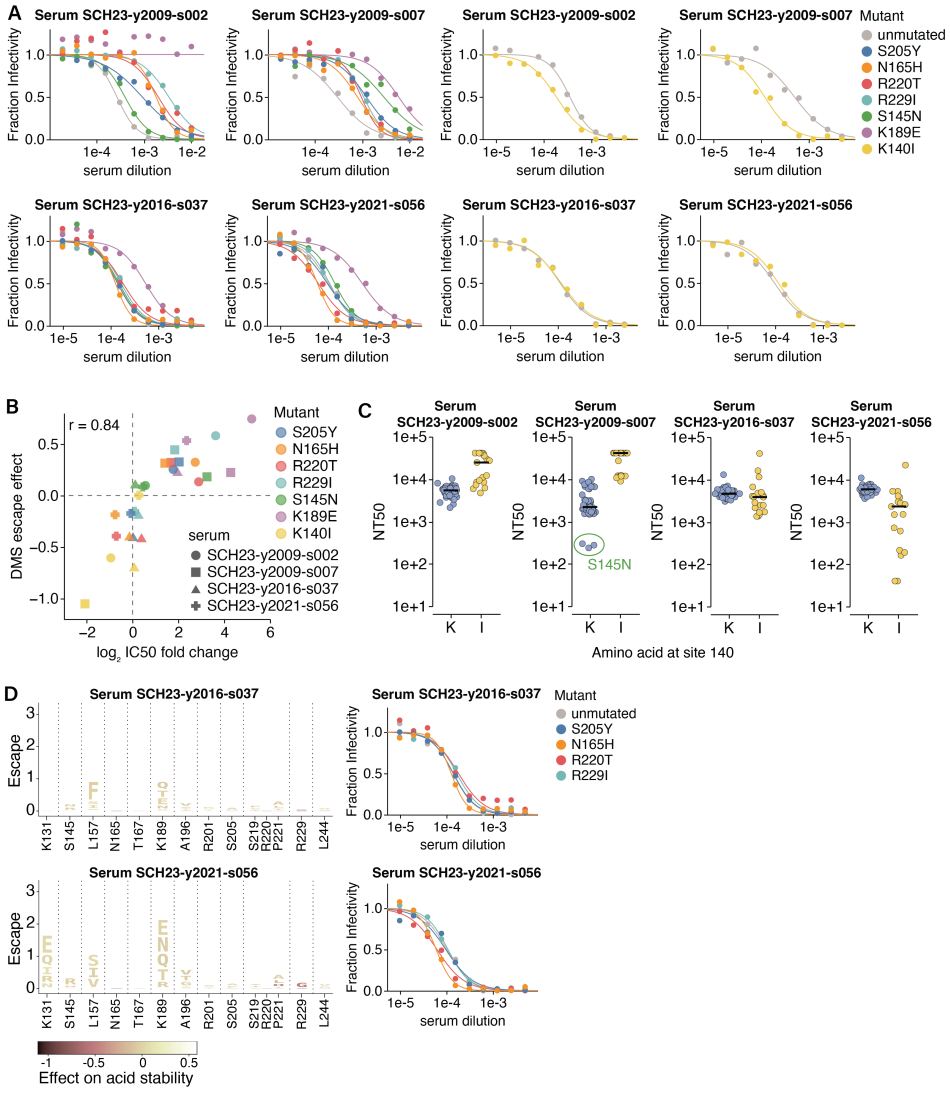

Figure 3.13: **Validation of mutation effects on serum neutralization with conditionally replicative influenza virions.** See full caption on next page.

Validation of mutation effects on serum neutralization with conditionally replicative influenza virions. A) Neutralization of conditionally replicative influenza virions with the MA22 HA carrying the indicated mutations (S205Y, N165H, R220T, R229I, S145N, K189E, and K140I) by four human sera collected in 2023. Each point is the mean of two technical replicates. A subset of these curves are shown in **Figure 3.4C**, **Figure 3.4F**, and **Figure 3.13D**. B) Correlation between the antigenic effect of mutations measured by deep mutational scanning and the change in IC50 measured by the independent neutralization assay in A. C) Neutralization for 78 vaccine or circulating H3N2 strains between 2012 and 2023 by the four sera, as measured in Kikawa et al. [78]. The points are the median of two or three barcoded replicates and are stratified by whether or not the strain includes a K or I at site 140. The black line indicates the median NT50. Two of the sera have higher titers against strains with 140I, consistent with K140I being a sensitizing mutation for these sera. There are three recent strains that contain S145N that escape SCH23-y2009-s007, consistent with this being an escape mutation from this sera. D) Logoplots displaying single nucleotide accessible mutations from MA22 HA with positive escape at the key sites highlighted red in **Figure 3.4A** for two sera. The height of each letter is proportional to the escape from the indicated serum as measured by deep mutational scanning. Each mutation is colored by its effect on HA acid stability as measured in the deep mutational scanning, with darker colors indicating decreased stability. The logoplots and neutralization curves for the other two sera mapped by deep mutational scanning are shown in **Figure 3.4E** and **Figure 3.4F**. In the neutralization curves, each point is the mean of two technical replicates.

Receptor binding pocket region	Sites
130-loop	128, 130, 131, 133-138
150-loop	155-160
190-helix	186, 189-194, 196-198
220-loop	221-228
Base	98, 153, 183, 195
Other	145
Antigenic region	
Epitope A	122-146
Epitope B	155-160, 186-198
Epitope C	44-54, 273-280
Epitope D	166-181, 201-219
Epitope E	62-65, 78-94, 260-265

Figure 3.14: **Sites within receptor binding pocket and antigenic regions.**

3.6 Methods

Cell lines and media

The following cell lines were used: 293T (ATCC, CRL-3216), 293T-rtTA (from Dadonaite et al. [29]), 293T-CMV-PB1 (from Bloom et al. [11]), MDCK-SIAT1 (HPA Cultures, 05071502), MDCK-SIAT1-CMV-PB1 (from Bloom et al. [11]), and MDCK-SIAT1-CMV-PB1-TMPRSS2 (from Lee et al. [91]).

All cell lines were maintained in D10 media (Dulbecco's Modified Eagle Medium supplemented with 10% heat-inactivated fetal bovine serum, 2 mM l-glutamine, 100 U/mL penicillin, and 100 µg/mL streptomycin). To suppress rtTA activation, 293T-rtTA cells were grown in tet-free D10, which is made with tetracycline-negative fetal bovine serum (Gemini Bio, Ref. No. 100-800) instead. For virus rescue and infection with HA expressing pseudovirus libraries and conditionally replicative influenza viruses, we used Influenza Growth Media (IGM, Opti-MEM supplemented with 0.01% heat-inactivated fetal bovine serum, 0.3% bovine serum albumin, 100 µg/mL of calcium chloride, 100 U/mL penicillin, and 100 µg/mL streptomycin) or Neutralization Assay Media (NAM, Medium-199 supplemented with 0.01% heat-inactivated fetal bovine serum, 0.3% bovine serum albumin, 100 µg/mL calcium chloride, 100 U/mL penicillin, 100 µg/mL streptomycin, and 25 mM HEPES).

Plasmids and primers

Plasmid maps can be found at: https://github.com/dms-vep/Flu_H3_Massachusetts2022_DMS/tree/main/data/supplemental_data/plasmids
Primer sequences can be found at: https://github.com/dms-vep/Flu_H3_Massachusetts2022_DMS/tree/main/data/supplemental_data/primers

Human sera

Human sera samples were obtained from Seattle Children's Hospital during routine blood draws from children receiving medical care in December 2023. This was approved by the Seattle Children's Hospital Institutional Review Board with a waiver of consent. Sera samples were treated with receptor-destroying enzyme (RDE) and heat-inactivated to remove non-specific inhibitors prior to use in deep mutational scanning library selections and neutralization assays. RDE was prepared by resuspending one vial of lyophilized RDE II (Seikan) in 20 mL PBS and filtering through a 0.22 µM filter. Sera and RDE were combined at a 1:3 sera to RDE ratio, incubated at 37°C for 2.5 hours, and then incubated at 55°C for 30 minutes [90]. RDE-treated sera were stored at -80C until further use.

Design of deep mutational scanning libraries

We used a lentiviral backbone that is schematized in **Figure 3.5A** [29]. The libraries were designed in the background of the A/Massachusetts/18/2022 HA, which was the 2024-2025 cell-based vaccine strain. The HA gene was codon-optimized via the GenSmart codon optimization tool offered by GenScript, as we found this codon optimization increases viral titers. The plasmid map for the lentiviral backbone with codon-optimized HA sequence is at: https://github.com/dms-vep/Flu_H3_Massachusetts2022_DMS/blob/main/data/supplemental_data/plasmids/4570_pH2rU3_ForInd_Massachusetts2022HA_GenscriptV1_T7_CMV_ZsGT2APurR.gb. We aimed to include all single amino acid mutations in the HA ectodomain (H3 numbering: 1-504). 20 stop codons located at alternating positions from the start of the ectodomain were also included as negative controls for cell entry measurements. We ordered a site-saturation variant library with these specifications from Twist Biosciences. The final Twist quality control report for the library is at: https://github.com/dms-vep/Flu_H3_Massachusetts2022_DMS/blob/main/data/supplemental_data/Final_QC_Twist_VariantProportion.csv

Cloning of deep mutational scanning plasmid library

We cloned the deep mutational scanning plasmid libraries following an approach first described in Dadonaite et al. [29]. Barcoding PCR was performed using the Twist library as template to append random 16 nucleotide barcodes downstream of the HA gene stop codon. 5 ng of Twist library (1 µL) was combined with 1.5 µL of ForInd_AddBC_2 primer (10 µM), 1.5 µL of 5'for_lib_bcing primer (10 µM), 21 µL of molecular biology grade water, and 25 µL of KOD Hot Start Master Mix (ThermoFisher, Ref. No. 71842-4). The PCR cycling conditions were:

1. 95°C, 2 min
2. 95°C, 20 sec
3. 55.5°C, 20 sec, cooling at 0.5°C/sec
4. 70°C, 1 min
5. Return to Step 2, 9 cycles
6. 12°C hold

The barcoding was performed in two independent reactions, yielding two barcoded PCR products to serve as biological library replicates (libraries A and B). Therefore, the two libraries contain unique barcodes, and all subsequent cloning and virus generation steps were carried out separately for each library.

The lentiviral backbone was digested from a plasmid containing mCherry in place of the HA insert (3137_pH2rU3_ForInd_mCherry_CMV_ZsGT2APurR) by incubating with XbaI and MluI for 2 hours at 37°C, followed by 20 minutes at 65°C to inactivate XbaI.

Both the barcoded HA libraries and digested lentiviral backbone were run on a 0.8% agarose gel, and bands of the expected size were excised and purified using the NucleoSpin Gel and PCR Clean-up kit (Macherey-Nagel, Cat. No. 740609.5) followed by additional purification with Ampure XP beads (Beckman Coulter, Cat. No. A63881) to ensure high purity. All were eluted in molecular biology grade water.

Barcoded HA libraries were cloned into the lentiviral backbone at a 1:2 insert to vector ratio in a 1 hour Hifi assembly reaction using the NEBuilder HiFi DNA Assembly kit (NEB E5520S). The Hifi reactions were purified with Ampure XP beads and eluted in molecular biology grade water, then transformed into 10-beta electrocompetent cells (NEB, Cat. No. C3020K) using a BioRad MicroPulser Electroporator (Cat. No. 1652100), shocking at 2 kV for 5 milliseconds. 15 electroporation reactions were performed for each library and bacteria were plated on 15 cm LB+ampicillin plates and grown overnight at 37°C. The next day, colonies were scraped with LB+ampicillin and plasmids were extracted using the QIAGEN HiSpeed Plasmid Maxi Kit (Cat. No. 12662). The total number of colonies for Library A and B were 8.4e6 and 7.5e6 CFU's respectively. Large numbers of colonies at this stage are necessary to ensure library diversity does not become bottlenecked.

Based on the Twist quality control report, 35 sites were missing >75% of mutations and 19 mutations at other sites were missing in the library. Therefore, we aimed to clone a "spike-in" plasmid library that contains these missing mutations using a mutagenesis PCR protocol24,69. We designed NNS primers for missing sites with https://github.com/jbloomlab/CodonTilingPrimers and primers for missing mutations with https://github.com/jbloomlab/TargetedTilingPrimers. Forward and reverse primer pools were created by combining either forward or reverse NNS and targeted mutation primers at an equal molar ratio per codon. To prepare a linear HA template for mutagenesis PCR, the lentiviral backbone plasmid encoding the codon-optimized HA was incubated with NotI and NdeI for 2 hours at 37°C, followed by 20 minutes at 65°C to inactivate both enzymes. The digest product was run on a 0.8% agarose gel, and the band corresponding to the linear HA fragment was purified.

The protocol for mutagenesis involves two reactions: a mutagenesis PCR and a joining PCR. Two separate replicates were performed to form biological library replicates (spike-in libraries A and B) as was done for the Twist libraries. The first mutagenesis PCR was divided into forward and reverse reactions. Both forward and reverse reactions shared the following PCR conditions: 4 µL of linear HA template (3 ng/µL), 8 µL of molecular biology grade water, and 15 µL of KOD Hot Start Master Mix. 1.5 µL of the forward primer pool (5 µM) and 1.5 µL of 3'rev_linjoin_KHDC primer (5 µM) were added to the forward reaction. 1.5 µL of the reverse primer pool (5 µM) and 1.5 µL of VEP_Amp_For primer (5 µM) were added to the reverse reaction. The PCR cycling conditions were:

1. 95°C, 2 min
2. 95°C, 20 sec

3. 70°C, 1 sec
4. 54°C, 20 sec, cooling at 0.5°C/sec
5. 70°C, 50 sec
6. Return to Step 2, 9 cycles
7. 4°C hold

The forward and reverse mutagenesis PCR products were diluted 1:4 in molecular biology grade water and 4 µL of each were added to the joining PCR reaction along with the following: 1.5 µL of 3'rev_linjoin_KHDC primer (5 µM), 1.5 µL of VEP_Amp_For primer (5 µM), 4 µL of molecular biology grade water, and 15 µL of KOD Hot Start Master Mix. The PCR cycling conditions were:
1. 95°C, 2 min
2. 95°C, 20 sec
3. 70°C, 1 sec
4. 54°C, 20 sec, cooling at 0.5°C/sec
5. 70°C, 65 sec
6. Return to Step 2, 19 cycles
7. 4°C hold

A DpnI digest was performed afterwards to remove any potential unmutated HA template (which would be methylated) by incubating the joining PCR products with DpnI for 20 minutes at 37°C. DpnI-digested joining PCR products were run on a 0.8% gel and the expected bands were excised and purified as described above. The mutagenized HA fragments were barcoded and cloned into the lentiviral backbone following the same approach described above for the Twist library. However, spike-in plasmids were extracted using the QIAprep Spin Miniprep Kit (Qiagen, cat. no. 27104) instead of via maxipreps.

Corresponding replicates of the Twist plasmid libraries and spike-in plasmid libraries were combined at a 1:4 Twist to spike-in molar ratio per codon, with the spike-in library intentionally added at four times the amount required for an equal per-codon molar ratio because long-read PacBio sequencing of the plasmid libraries revealed this ratio results in the most even distribution of mutants in the combined libraries.

Production of cell-stored deep mutational scanning libraries

Deep mutational scanning requires genotype-phenotype linked pseudoviruses. The rationale for this is described in detail in the caption of **Figure 3.5B**. We generated cell-stored deep mutational scanning libraries where each cell is integrated with a single copy of a barcoded HA mutant to enable rescue of genotype-phenotype linked pseudoviruses [29, 26]. 15cm plates were plated with ~20 million 293T cells. On the next day, each plate was transfected with 12.5 µg of plasmid library en-

coding the lentiviral backbone with barcoded HA mutants, 3.125 µg of each lentiviral helper plasmid (26_HDM_Hgpm2, 27_HDM_tat1b, and 28_pRC_CMV_Rev1b), 3.125 µg of plasmid expressing VSV-G (29_HDM_VSV_G), and 3.125 µg of plasmid expressing a strain-matched codon-optimized neuraminidase gene (4576_HDM_Massachusetts2022NA_Genscript). BioT transfection reagent (Bioland Scientific, Cat. No. B01-02) was used according to manufacturer's instructions. Note the NA is important because the virions produced here will also have HA expressed on their surface from the lentiviral backbone. The NA expression prevents HA from binding to producing cells, as this binding could bias the library since the HA mutants will have different abilities to bind to sialic acids on the producing 293T cells. 48 hours post transfection, the supernatant was filtered through a 0.45 µm syringe filter (Corning, Cat. No. 431220) and stored at -80°C. 4 x 15cm plates were transfected with each library replicate, resulting in ~100 ml of VSV-G pseudotyped library viruses. An aliquot of these viruses was used to infect 293T cells, and the titer in transcription units (TU) per mL was determined by measuring the percentage of zsGreen positive cells via flow cytometry.

The VSV-G pseudotyped library viruses were used to infect 293T-rtTA cells at a multiplicity of infection (MOI) of 0.7% to ensure each cell integrates at most one copy of provirus. The MOI was confirmed by measuring the percentage of zsGreen positive cells via flow cytometry at 48 hours post transduction. Based on the measured MOI and number of cells present during infection, cells were pooled such that each library would contain an estimated 60,000 infected cells. This number was chosen to be high enough to ensure each mutant is associated with multiple barcodes to increase measurement accuracy (for ~10,000 mutants, each mutant would have ~6 barcodes), while also being low enough that it would be possible to measure all variants given our pseudovirus titers in selection experiments. Note the final numbers ended up being close to this target: 64,032 for library A and 70,581 for library B (**Figure 3.5C**). Integrated cells were selected by growing in the presence of 0.75 µg/mL of puromycin for 1 week (fresh media with puromycin was replenished every 48 hours). After selection was complete, integrated cells were expanded in tet-free D10 for 24 hours and then frozen down in liquid nitrogen in 2e7 cell aliquots for long-term storage.

Rescue of HA and VSV-G expressing pseudovirus libraries

To rescue HA expressing pseudoviruses from the integrated cells, 150 million cells were plated in 5-layer flasks in tet-free D10 supplemented with 1 µg/mL of doxycycline to induce HA expression from the integrated genomes. On the next day, each flask was transfected with 43.75 µg of each helper plasmid (26_HDM_Hgpm2, 27_HDM_tat1b, and 28_pRC_CMV_Rev1b), 15 µg of plasmid expressing human airway trypsin-like protease (3781_HDM_HAT) to activate HA for membrane fusion, and 3.75 µg of plasmid expressing NA (4576_HDM_Massachusetts2022NA_Genscript). BioT transfection reagent was

used according to manufacturer's instructions. At 16 hours post transfection, the tet-free D10 in each flask was aspirated and 150 mL of IGM supplemented with 1 µg/mL of doxycycline was added. This swap to low-serum media is absolutely necessary because non-specific inhibitors in FBS can inactivate HA and interfere with pseudovirus infection. At 32 hours post media swap, the supernatant was filtered through a 0.45µm SFCA Nalgene 500 mL Rapid-Flow filter unit (Cat. No. 09-740-44B). Filtered supernatant was then concentrated by adding LentiX Concentrator (Takara, Cat. No. 631232) at a 1:3 virus to concentrator ratio, incubating at 4°C overnight, and spinning at 1500 x g and 4°C for 45 minutes. Following centrifugation, supernatant was discarded and viral pellets resuspended in NAM to an estimated titer of ~2e6 TU/mL. 1 mL aliquots of concentrated HA expressing pseudoviruses were frozen at -80°C for use in downstream selection experiments.

To rescue VSV-G expressing pseudoviruses from integrated cells, 30 million cells were plated in 10 cm plates in tet-free D10. On the next day, each plate was transfected with 7.3125 µg of each helper plasmid (26_HDM_Hgpm2, 27_HDM_tat1b, and 28_pRC_CMV_Rev1b), 0.75 µg of plasmid expressing NA (4576_HDM_Massachusetts2022NA_Genscript), and 7.3125 µg of plasmid expressing VSV-G (29_HDM_VSV_G). At 48 hours post transfection, the supernatant was filtered through a 0.45µm SFCA Nalgene 500 mL Rapid-Flow filter unit and concentrated using LentiX Concentrator but viral pellets were resuspended in D10. Aliquots of concentrated VSV-G expressing pseudoviruses were frozen at -80°C for use in linking mutations to barcodes and cell entry selection experiments.

Long-read sequencing to link mutations to barcodes

1e6 293T cells were plated in each well of 6-well plates coated with poly-L-lysine to help with cell adhesion. On the next day, 15 million TU's of VSV-G expressing pseudoviruses that were rescued from cell-stored deep mutational scanning libraries were used to infect the cells. At 12 hours post infection, the non-integrated reverse-transcribed lentiviral genomes were recovered by miniprepping the 293T cells using the QIAprep Spin Miniprep Kit.

Amplicons for long-read sequencing of the miniprepped genomes were prepared by following an approach described in Dadonaite et al. [29]. Briefly, the eluted minipreps were split into two separate reactions so each could be uniquely tagged for detecting strand exchange events from the PCR. The number of PCR cycles was chosen intentionally to limit the possibility of strand exchange. Both reactions shared the following PCR conditions: 20 µL of KOD Hot Start Master Mix and 18 µL of miniprepped DNA. 1 µL of 5_PacBio_G primer (10 µM) and 1 µL of 3_PacBio_C primer (10 µM) were added to the first reaction. 1 µL of 5_PacBio_C primer (10 µM) and 1 µL of 3_PacBio_G primer (10 µM) were added to the second reaction. The PCR cycling conditions were:

1. 95°C, 2 min

2. 95℃, 20 sec
3. 70℃, 1 sec
4. 60℃, 10 sec, cooling at 0.5℃/sec
5. 70℃, 60 sec
6. Return to Step 2, 7 cycles
7. 70℃, 1 min
8. 4℃ hold

The round 1 PCR products were purified with 50 μL of Ampure XP beads and eluted in 35 μL of elution buffer. For each library, equal volumes of the two separate round 1 PCR reactions were pooled. The round 2 PCR reactions contained: 25 μL of KOD Hot Start Master Mix, 21 μL of pooled round 1 product, 2 μL of 5_PacBio_Rnd2 primer (10 μM) and 2 μL of 3_PacBio_Rnd2 primer (10 μM). The PCR cycling conditions were:

1. 95℃, 2 min
2. 95℃, 20 sec
3. 70℃, 1 sec
4. 60℃, 10 sec, cooling at 0.5℃/sec
5. 70℃, 1 min
6. Return to Step 2, 10 cycles
7. 70℃, 1 min
8. 4℃ hold

The round 2 PCR products were purified with 50 μL of Ampure XP beads and eluted in 40 μL of elution buffer. PCR reactions for each library were combined and amplicon length was verified by TapeStation prior to sequencing. Libraries were sequenced on a single SMRT cell with a movie length of 30 hours on a PacBio Sequel IIe sequencer. For details on computational analysis, see the '**PacBio sequencing analysis**' section.

Mutation effects on cell entry

To measure effects of HA mutations on cell entry, we followed the approach described in Dadonaite et al. [29]. Briefly, we infected MDCK-SIAT1 cells with the HA expressing pseudovirus library and infected 293T cells with the VSV-G expressing pseudovirus library. The VSV-G expressing library is necessary to provide a baseline for infection as VSV-G can mediate cell entry without relying on HA. We used 293T cells for VSV-G infection because titers of VSV-G expressing pseudoviruses are higher when infecting 293T cells compared to MDCK-SIAT1 cells.

1e6 293T cells in D10 or 7e5 MDCK-SIAT1 cells in NAM were plated in each well of 6-well plates.

2.5 μg/mL of amphotericin B was added to the MDCK-SIAT1 cells when plating as this improves HA pseudovirus titers. On the next day, we infected the MDCK-SIAT1 cells with ~1.2e6 TU's of HA pseudovirus library and the 293T cells with ~8e6 TU's of VSV-G pseudovirus library. Prior to infection, the HA pseudovirus library was treated with 500 nM of oseltamivir for 20 minutes on ice to inhibit NA from interfering with cell entry. Note infections with the HA pseudovirus library must be done in NAM, as the serum in D10 contains non-specific inhibitors that inhibit H3 infection.

At 12 hours post infection, the non-integrated reverse-transcribed lentiviral genomes were recovered by miniprepping the 293T and MDCK-SIAT1 cells. To prepare the amplicons for Illumina sequencing, two rounds of PCR were performed: the first round appends the Illumina Truseq Read 1 and Read 2 sequences, and the second round attaches indices for multiplexing. The Round 1 PCR reactions contained: 22 μL of miniprepped DNA, 25 μL of KOD Hot Start Master Mix, 1.5 μL of Illumina_Rnd1_For primer (10 μM), and 1.5 μL of Illumina_Rnd1_Rev3 primer (10 μM). The PCR cycling conditions were:

1. 95°C, 2 min
2. 95°C, 20 sec
3. 70°C, 1 sec
4. 58°C, 10 sec, cooling at 0.5°C/sec 5. 70°C, 20 sec
5. Return to Step 2, 27 cycles
6. 70°C, 1 min
7. 4°C hold

Round 1 PCR products were purified with 150 μL of Ampure XP beads and eluted in 50 μL of elution buffer. Concentrations of each PCR product were determined by Qubit 4 Fluorometer (ThermoFisher, Ref. No. Q33238). The Round 2 PCR reactions contained: 20 ng of Round 1 PCR product, 25 μL of KOD Hot Start Master Mix, 2 μL of each of the Round 2 indexing primers (10 μM each), and up to 25 μL of molecular biology grade water. The same PCR cycling conditions as Round 1 were used, except only 20 cycles were performed. Concentrations of each round 2 PCR product were determined by Qubit 4 Fluorometer. The samples were then pooled in equal DNA amounts and run on a 1% agarose gel. The correct size band (283 bp) was excised, purified with Ampure XP beads, diluted to a concentration of 4 nM, and sequenced on a Illumina NextSeq 2000 (with P2 reagent kit) or NovaSeq X Plus system. For details on how sequencing counts were converted to mutation effects on cell entry, see the '**Illumina sequencing barcode analysis**' section.

Mutation effects on acid stability

To measure effects of HA mutations on acid stability, we followed the approach in Dadonaite et al. [26]. Briefly, we incubated the HA pseudovirus library in different acidic pH buffers prior to infecting MDCK-

SIAT1 cells. We also included a condition where the HA pseudovirus library was incubated with neutral pH media prior to infection.

7e5 MDCK-SIAT1 cells in NAM were plated in each well of 6-well plates. 2.5 µg/mL of amphotericin B was added to the MDCK-SIAT1 cells when plating. On the next day, aliquots containing ~2.4e6 TU/mL of HA pseudovirus library were incubated with citrate-based acidic buffers at pH 6.1, 5.9, 5.7, 5.5, 5.3 or NAM (neutral pH condition) for 60 minutes at 37°C. After incubation, libraries were concentrated with 100k Amicon spin columns (Millipore, UFC910008) by spinning for 15 minutes at 1500 x g, resuspending in 11 mL of PBS to neutralize the acidic buffers, and spun down again for 20 minutes at 1500 x g. The libraries were then resuspended in 2 mL of NAM, treated with 500 nM of oseltamivir for 20 minutes on ice to inhibit NA, and used to infect the plated MDCK-SIAT1 cells.

At 12 hours post infection, the non-integrated reverse-transcribed lentiviral genomes were recovered by miniprepping the MDCK-SIAT1 cells. In the miniprep lysis step where P2 buffer is added, we spiked in a DNA standard at an amount calculated to be approximately 3% of the recovered lentiviral DNA (based on the estimated number of non-integrated lentiviral genomes) under normal infection conditions with no acidic buffer treatment. The rationale for including the DNA spike-in standard is to enable relative sequencing counts to be converted into absolute quantities of each barcoded pseudovirus variant, normalized to the standard, across different acidic buffer conditions. This DNA standard is a plasmid that encodes the lentiviral backbone with a barcoded mCherry gene; the plasmid map is 3068_ForInd_mC_BCs_pool1 and the barcodes are at: https://github.com/dms-vep/Flu_H3_Massachusetts2022_DMS/blob/main/data/neutralization_standard_barcodes.csv. Afterwards, amplicons for Illumina sequencing were prepared as described in the previous section. For details on how sequencing counts were converted to mutation effects on acid stability, see the '**Illumina sequencing barcode analysis**' section.

Mutation effects on sera neutralization

To measure effects of HA mutations on sera neutralization, we followed the approach in Dadonaite et al. [29]. 7e5 MDCK-SIAT1 cells in NAM were plated in each well of 6-well plates. 2.5 µg/mL of amphotericin B was added to the MDCK-SIAT1 cells when plating. On the next day, aliquots containing ~1.2e6 TU/mL of HA pseudovirus library were treated with 500 nM oseltamivir and incubated with three concentrations of sera estimated to span between IC98 and IC98*16. These IC values were determined by a luciferase-based pseudovirus neutralization assay. Multiple dilutions of sera are necessary for improving estimation of mutation effects on sera neutralization. Libraries and sera were incubated for 60 minutes at 37°C. After incubation, libraries were used to infect the plated MDCK-SIAT1 cells. At 12 hours post infection, the non-integrated reverse-transcribed lentiviral genomes were recovered by miniprepping with

the spike-in DNA standard and amplicons for Illumina sequencing were prepared as described in the previous section. For details on how sequencing counts were converted to mutation effects on sera neutralization, see the '**Illumina sequencing barcode analysis**' section.

Production of conditionally replicative influenza viruses

Conditionally replicative influenza viruses that lack the PB1 gene were produced by reverse genetics [68, 38]. The native HA sequence was cloned into a bidirectional pHW2000 influenza reverse genetics plasmid. The plasmid map for A/Massachusetts/18/2022 HA is 5012_pHW_MA22_HA and the plasmid map for A/Perth/16/2009 HA is 1442_pHWPerth09_HA. Mutant HA plasmids were cloned by PCR with partially overlapping primers that contain the mutation of interest, followed by HiFi assembly. All plasmids were sequence confirmed by Plasmidsaurus. To perform the virus rescue, 5e5 293T-CMV-PB1 cells and 4e5 MDCK-SIAT1-CMV-PB1-TMPRSS2 cells were plated in D10 in each well of 6-well plates. On the next day, each well was transfected with 2 µg total of plasmids including: 0.25 µg each of six reverse genetics plasmids expressing genes from A/WSN/1933 (30_pHW181_PB2, 32_pHW183_PA, 34_pHW185_NP, 35_pHW186_NA, 36_pHW187_M, and 37_pHW188_NS), 0.25 µg of plasmid that expresses eGFP in place of PB1 (208_pHH_PB1flank_eGFP), and 0.25 µg of HA reverse genetics plasmid. At 24 hours post transfection, D10 was aspirated and each well was replenished with 2 mL of IGM. At 48 hours post media swap, viral supernatant was spun down for 4 minutes at 845 x g, and aliquots of clarified supernatant were collected and frozen down at -80°C.

Validation of cell entry effects

Conditionally replicative influenza viruses were serially diluted in NAM in 96-well plates. 5e4 MDCK-SIAT1-CMV-PB1 cells in NAM were added to each well. Note these cells do not express TMPRSS2, so the influenza viruses can only undergo a single cycle of infection. At 16 hours post infection, wells with 1-10% percent eGFP-positive cells were selected. Precise measurements of the percent of eGFP-positive cells in these wells were obtained by flow cytometry and viral titers were calculated using a Poisson distribution.

Validation of acid stability effects

1.5e5 MDCK-SIAT1-CMV-PB1 cells in D10 were plated in each well of a 12-well plate. Conditionally replicative influenza viruses were diluted to a target MOI of 0.5 to 1 (~2 to 10 µL of virus) in 100 µL of citrate-based acidic buffers at pH 5.7, 5.5, and 5.3 or NAM (neutral pH condition) and incubated for 60 minutes at 37°C. The pH-treated viruses were then brought back to neutral pH by diluting the 100 µL into 2 mL of NAM. 4 hours after plating the MDCK-SIAT1-CMV-PB1 cells, D10 was aspirated and cells

were washed with 1 mL of 1X PBS before 2 mL of the NAM-diluted viruses were added. At 16 hours post infection, the percent of eGFP-positive cells in each well was determined by flow cytometry. The fraction infectivity retained was calculated as the ratio of percent eGFP-positive cells when virus was treated with acidic pH over the percent eGFP-positive cells when virus was treated with NAM.

Neutralization assays

Sera were serially diluted in NAM in 96-well plates. Conditionally replicative influenza viruses were diluted to a target MOI that falls within a range where the fluorescence signal would change linearly with respect to neutralization. The virus and sera dilutions were incubated for 60 minutes at 37°C. Afterwards, 4e4 MDCK-SIAT1-CMV-PB1 cells were added to each well. At 16 hours post infection, the fluorescence signal was read on a Tecan M1000 plate reader and the fraction infectivity was determined relative to no serum controls.

PacBio sequencing analysis

PacBio circular consensus sequences (CCSs) were aligned to the HA reference sequence using alignparse [24]. Consensus sequences for each barcode were determined by requiring at least 3 CCSs per barcode. See https://github.com/dms-vep/Flu_H3_Massachusetts2022_DMS/blob/main/results/variants/codon_variants.csv for the final barcode-variant table.

For full details on the analysis, see these notebooks for:
- Analyzing the PacBio CCS's: https://dms-vep.org/Flu_H3_Massachusetts2022_DMS/notebooks/analyze_pacbio_ccs.html
- Building PacBio consensus sequences: https://dms-vep.org/Flu_H3_Massachusetts2022_DMS/notebooks/build_pacbio_consensus.html
- Building the final barcode-variant table: https://dms-vep.org/Flu_H3_Massachusetts2022_DMS/notebooks/build_codon_variants.html

Illumina sequencing barcode analysis

From the Illumina short-read sequencing data, barcodes were counted by https://jbloomlab.github.io/dms_variants/dms_variants.illuminabarcodeparser.html and then mutation effects were calculated using approaches described previously [29, 26] and outlined below.

To convert barcode counts into mutation effects on cell entry, we first calculated functional scores. Briefly, a functional score for a variant v was calculated as

$$\log_2\left[\left(n^v_{\text{post}}/n^{wt}_{\text{post}}\right)/\left(n^v_{\text{pre}}/n^{wt}_{\text{pre}}\right)\right]$$

where each n is a count of barcodes that entered cells. Specifically, n^v_{post} is the count of each variant in the HA pseudovirus library, n^v_{pre} is the count of each variant in the VSV-G pseudovirus library, n^{wt}_{post} and n^{wt}_{pre} are counts of the unmutated (wildtype) variants in these libraries. Positive functional scores indicate the variant is better at entering cells relative to the unmutated HA, while negative functional scores indicate the variant is worse at entering cells relative to the unmutated HA. Since some variants contain multiple mutations, we used multidms [62] (https://matsengrp.github.io/multidms) to fit a global epistasis model with a sigmoid function using the functional scores to obtain individual mutation effects on cell entry. For more details on fitting, see the notebooks under 'Functional effects of mutations' at https://dms-vep.org/Flu_H3_Massachusetts2022_DMS/appendix.html. We report the median mutation effect across library replicates and filter for mutations that are seen in at least two different barcoded variants (averaged across libraries). See https://dms-vep.org/Flu_H3_Massachusetts2022_DMS/cell_entry.html for interactive visualizations of mutation effects on cell entry.

To convert barcode counts into mutation effects on acid stability and sera neutralization, we calculated the fraction infectivity of each variant retained at each acidic pH buffer treatment or serum concentration, normalizing to the counts of spike-in standard barcodes in each condition. We then fit a biophysical model to these fractional infectivity data using polyclonal [189] (https://jbloomlab.github.io/polyclonal) to obtain individual mutation effects on acid stability and sera neutralization. For more details on fitting, see the notebooks under 'Antibody/serum escape' and 'Stability' at https://dms-vep.org/Flu_H3_Massachusetts2022_DMS/appendix.html. We report the average mutation effect across library replicates, and filter for mutations that are seen in at least two different barcoded variants (averaged across libraries) and have a cell entry score > -3. See https://dms-vep.org/Flu_H3_Massachusetts2022_DMS/acid_stability.html for interactive visualizations of mutation effects on acid stability, and https://dms-vep.org/Flu_H3_Massachusetts2022_DMS/sera_neutralization.html for interactive visualizations of mutation effects on sera neutralization.

Entropy calculation from natural sequences

The subsampled Nextstrain tree was obtained from Kistler et al. [81]. The subsampling approach accounts for biases through evenly sampling sequences by year and major geographical region. This H3N2/HA/60y build is available at https://nextstrain.org/groups/blab/flu/seasonal/h3n2/ha/60y.

We calculate entropy from the amino acid frequencies at a given position. These frequencies are derived from the number of tips in the Nextstrain tree with a given amino acid, divided by the total number of tips in the Nextstrain tree. For example, consider a site where only two amino acids have been observed, with X tips of amino acid A and Y tips of amino acid B. The total number of tips in the tree is N = X + Y. Then, the entropy can be calculated using `scipy.stats` as: entropy([X/N, Y/N]).

Evolutionary entrenchment analysis

The frequencies of amino acids at different timepoints were obtained from the H3N2/HA/6oy Nextstrain tree. An amino acid was considered fixed if at any timepoint its frequency at a given site was >95%. Sites were considered inside the receptor binding pocket if they were within 4Å of sialic acid or previously reported to affect receptor binding [142, 83, 95]. See (**Figure 3.14**) for the full definition of receptor binding pocket sites. See https://dms-vep.org/Flu_H3_Massachusetts2022_DMS/entrenchment.html for an interactive plot of the analysis.

Structural analysis

UCSF ChimeraX v1.8 [108] was used for structural visualizations. All Protein Data Bank accession IDs used are included in figure legends.

Data availability

Data that have been pre-filtered for quality control criteria are available in CSV format at these links:
- Mutation effects on cell entry and acid stability: https://github.com/dms-vep/Flu_H3_Massachusetts2022_DMS/blob/main/results/summaries/Phenotypes.csv
- Mutation effects on sera neutralization: https://github.com/dms-vep/Flu_H3_Massachusetts2022_DMS/blob/main/results/summaries/Phenotypes_per_antibody_escape.csv

Raw sequencing data is available under BioProject PRJNA1320726 in the NCBI Sequence Read Archive.

Code availability

See https://dms-vep.org/Flu_H3_Massachusetts2022_DMS for a collection of interactive visualizations. Code for reproducing the analysis is at https://github.com/dms-vep/Flu_H3_Massachusetts2022_DMS and output of the analysis is at https://dms-vep.org/Flu_H3_Massachusetts2022_DMS/appendix.html.

Acknowledgements

This work was supported in part by the NIH/NIGMS CMB Training Grant (T32 GM007270) to TCY, NSF Graduate Research Fellowship (DGE-2140004) to TCY, NIH/NIAID under award R01AI165821 to JDB, and NIH/NIAID under contract 75N93021C00015 to JDB. JDB is an investigator of the Howard Hughes Medical Institute. This research was also supported by the Genomics & Bioinformatics Shared Resource (RRID: SCR_022606), the Flow Cytometry Shared Resource (RRID: SCR_022613) of the Fred Hutch/University of Washington/Seattle Children's Cancer Consortium (P30 CA015704), and by Fred Hutch Scientific Computing, NIH grants S10-OD-020069 and S10-OD-028685. We thank the Bedford lab at Fred Hutch for maintaining Nextstrain builds, John Huddleston for technical assistance, and Brendan Larsen for help with data visualization. This manuscript is the result of funding in whole or in part by the National Institutes of Health (NIH). It is subject to the NIH Public Access Policy. Through acceptance of this federal funding, NIH has been given a right to make this manuscript publicly available in PubMed Central upon the Official Date of Publication, as defined by NIH.

Author contributions statement

TCY and JDB conceived the study. TCY and CK performed the experiments. TCY and JDB performed the computational analysis. TCY, CK, BD, ANL, and JDB interpreted the results. TCY and JDB wrote the original draft. JAE provided resources. All authors edited and approved the paper.

Chapter 4

Influenza hemagglutinin subtypes have very different sequence constraints despite sharing extremely similar structures

This chapter presents ongoing work from the following manuscript in preparation:

> Jenny Ahn*, Timothy C. Yu*, Bernadeta Dadonaite, Jesse D. Bloom, **Influenza hemagglutinin subtypes have very different sequence constraints despite sharing extremely similar structures**, *in preparation*.

4.1 Abstract

Hemagglutinins (HA) from different influenza A virus subtypes share as little as ~40% amino acid identity, yet their protein structures and cell entry function are highly conserved. Here we examine the extent that sequence constraints on HA differ across three subtypes. To do this, we first use pseudovirus deep mutational scanning to measure how all mutations to an H7 HA affect its cell entry function. We then compare these new measurements to previously described measurements of how all mutations to H3 and H5 HAs affect cell entry function. We find that ~40-60% of HA sites display substantially diverged preferences for different amino acids across the HA subtypes. The sites with the most divergent amino-acid preferences tend to be buried and have biochemically distinct wildtype amino acids in the different HA subtypes. We provide an example of how rewiring the interactions among contacting residues has dramatically shifted which amino acids are tolerated at specific sites. Overall, our results show how proteins with the same structure and function can become subject to very different site-specific evolutionary constraints as their sequences diverge.

4.2 Results

4.2.1 Phylogenetic and structural comparison of H3, H5, and H7

The HA proteins of influenza A viruses of different subtypes are highly diverged at the sequence level, with amino-acid identities among different subtypes ranging from 36% to 80% (**Figure 4.1A,B**). Here we focus on HAs from three subtypes: H3, H5, and H7 (**Figure 4.1A**). H3 and H7 HAs have 47% amino-acid identity, while the H5 HA is more diverged from these other two, with identities of 40% and 43% to H3 and H7, respectively (**Figure 4.1B**).

Despite their extensive sequence divergence, H3, H5, and H7 HAs have highly conserved structures (**Figure 4.1C**). The root mean square deviations of the structurally aligned backbones of the two HA polypeptide chains (HA1 and HA2) are within 2.5 angstroms across experimentally determined structures of HAs from the three subtypes (**Figure 4.1C**), although there is some modest shift in the relative orientation of HA1 and HA2 (**Figure 4.5A,B**). All three HAs also have conserved biological functions of binding to sialic acid receptors and then mediating membrane fusion at acidic pH [14, 183, 51]. Viruses with H3 HAs have circulated in a variety of avian and mammalian species, including humans, dogs, and horses [123]. While avian H3 HAs preferentially bind α2-3 linked sialic acids, some mammalian-adapted H3 strains (including the H3N2 strains that are currently endemic in humans) preferentially bind to α2-6 linked sialic acids [105]. Viruses with H5 and H7 HAs mostly circulate in avian species, but they have caused sporadic infections of humans and other mammalian species [141], and a H5N1 strain recently became endemic in dairy cattle [6]. Avian H5 and H7 strains preferentially bind α2-3 linked sialic acids, although there are known mutations that can shift this binding preference from α2-3 to α2-6 linked sialic acids [160, 33, 100, 4, 98].

The sequence divergence among H3, H5, and H7 HAs is asymmetrically distributed across the protein (**Figure 4.1D**). The fusion peptide spanning sites 330-350 (throughout this paper, we use mature H3 numbering) is the most conserved region, consistent with its key function in mediating membrane fusion. Sites in HA1 tend to be more variable among the HA subtypes than sites in HA2, reflecting HA1's higher mutational tolerance [162, 65] and positive selection for HA1 mutations that reduce antibody recognition [15, 131].

4.2.2 Comparing amino-acid preferences across H3, H5, and H7 HAs

We next compared the H7 deep mutational scanning dataset to previously published H3 and H5 datasets [26, 188] to assess how the effects of amino-acid mutations on HA's cell entry function differ across these HA subtypes. To make these comparisons, we converted the measured effects of mutations on cell en-

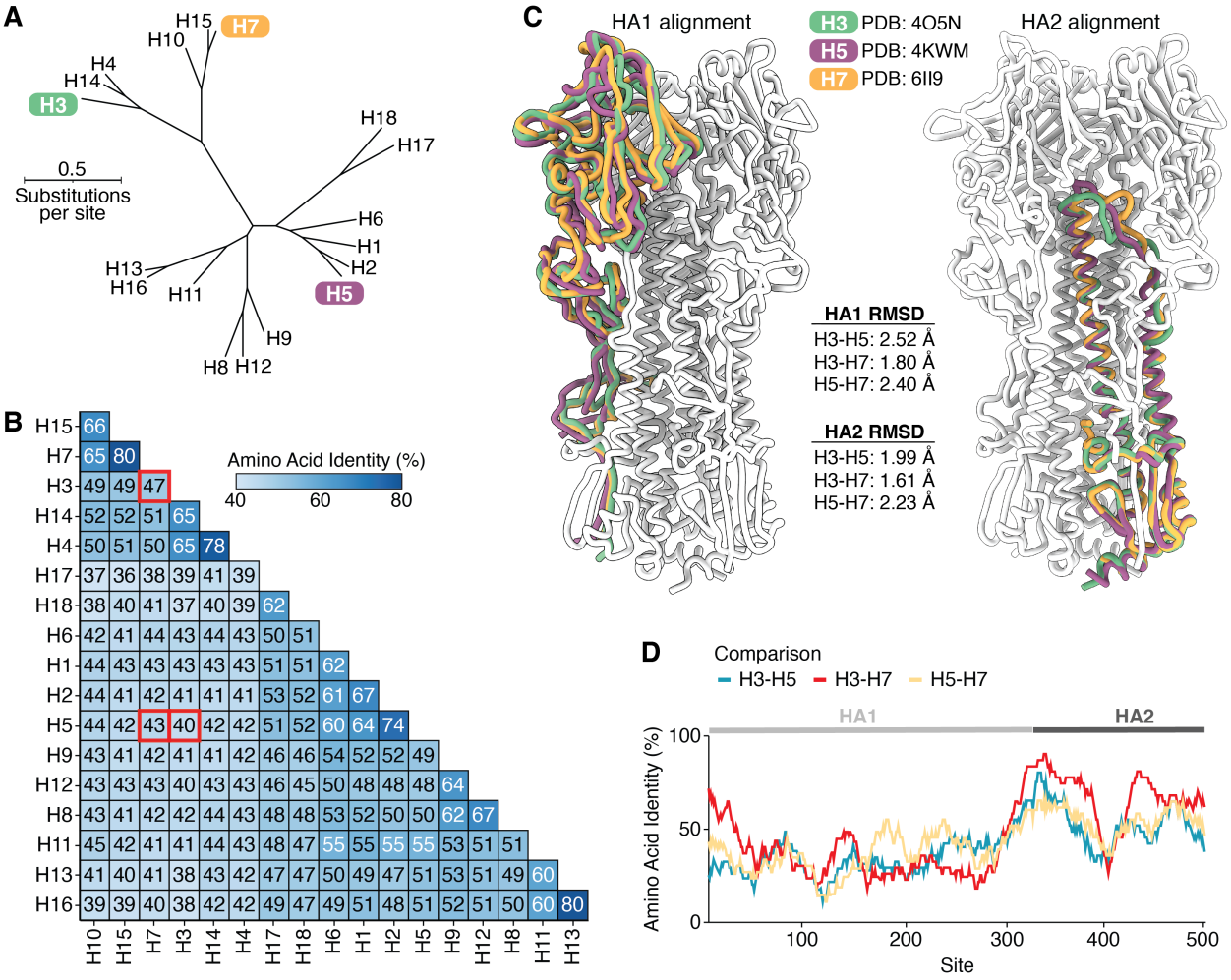

Figure 4.1: **Phylogenetic and structural comparison of H3, H5, and H7 HA.** A) Maximum-likelihood phylogenetic tree of HA protein sequences inferred using IQ-TREE [118] by the Jones-Taylor-Thornton amino-acid substitution model with rate variation. B) Pairwise amino acid identity between the HAs shown in A, with red boxes indicating comparisons between the three subtypes that are the focus of the experimental work in this study. C) Structural alignments of single HA1 or HA2 monomers of H3 (green), H5 (purple), and H7 (orange) HAs. The rest of the H3 HA trimer (white) is included to provide structural context. HA1 and HA2 were aligned separately due to a shift in the relative orientation of these domains (see **Figure 4.5**). The root mean square deviation (RMSD) of carbons between the aligned HA1 and HA2 monomers are also reported. D) Pairwise amino acid identities between the different HA subtypes computed along the length of the primary sequence with a sliding window of 30 residues. The HA structures used in this figure are PDB 6II9 (H7) [69], PDB 4O5N (H3) [92], and PDB 4KWM (H5) [144].

try to normalized values quantifying the preference of each site for each amino acid. Quantitatively, the preference $\pi_{r,a}$ of site r for amino acid a is defined as proportional to the exponential of the effect $x_{r,a}$ of that mutation on cell entry, namely as $\pi_{r,a} = \exp\left(x_{r,a}\right) / \left(\sum_{a'} \exp\left(x_{r,a'}\right)\right)$ where the sum over a is taken over all amino-acid identities. If all amino-acid mutations except the wildtype identity are highly deleterious at a site then only that wildtype amino acid is preferred; when many mutations are well tolerated at a site then many amino acids have similar preferences (**Figure 4.2A**). There are two advantages of converting the measured effects of mutations to amino-acid preferences for comparing across subtypes. First, unlike the mutation effects, the amino-acid preferences at a site are not defined relative to its wildtype amino-acid identity and so facilitate direct comparison across H3, H5, and H7, which often have different amino acids at the same site (**Figure 4.1B**). Second, quantitative comparisons using amino-acid preferences emphasize differences in which amino acids at a site are well tolerated, whereas quantitative comparisons using directly measured mutation effects also emphasize less relevant differences between moderately and strongly deleterious amino acid identities at a site. Given the experimentally measured set of amino-acid preferences at a site in two different HA subtypes, we quantified the difference in evolutionary constraint at the site by the Jensen-Shannon divergence. This divergence is high when mutations at a site have dramatically different effects between HA subtypes, and low when mutations have similar effects in both HA subtypes (**Figure 4.2B**).

Many HA sites display high divergence in amino-acid preferences among subtypes (**Figure 4.2C**). Overall, 63% of sites exhibited significant divergence in amino-acid preferences between H3-H5, 44% of sites between H5-H7, and 44% of sites between H3-H7 (FDR < 0.1, see red points in **Figure 4.2C**). At those significantly diverged sites, HAs of different subtypes often preferred distinct amino acid types (**Figure 4.2A**, left panel), demonstrating how the biochemical determinants of mutational tolerance differs across HA subtypes. Although the experimental measurements of the effects of mutations on cell entry were performed in different target cells (a mix of 293 cells expressing α2-3- and α2-6-linked sialic acids for H7, MDCK-SIAT1 for H3 [188], and 293T for H5 [26]) that express varying ratios of α2-3- and α2-6-linked sialic acids, the use of different target cells is not a major contributor to the divergence in amino-acid preferences across subtypes. This fact is demonstrated by observing that there is very little divergence between the amino-acid preferences of the H7 HA between measurements made using 293-α2-3 versus 293-α2-6 cells (**Figure 4.6A,B**), with only a few sites in the receptor-binding pocket exhibiting modest differences in amino-acid preferences between cell types. Collectively, these results suggest the evolutionary constraints on cell entry are dramatically different across H3, H5, and H7 due to large changes in sequence that alter the preferences for specific amino acids at different sites due to their impacts on fundamental aspects of HA protein folding and function.

We next examined if the sites with high divergence in amino-acid preferences localized to particular

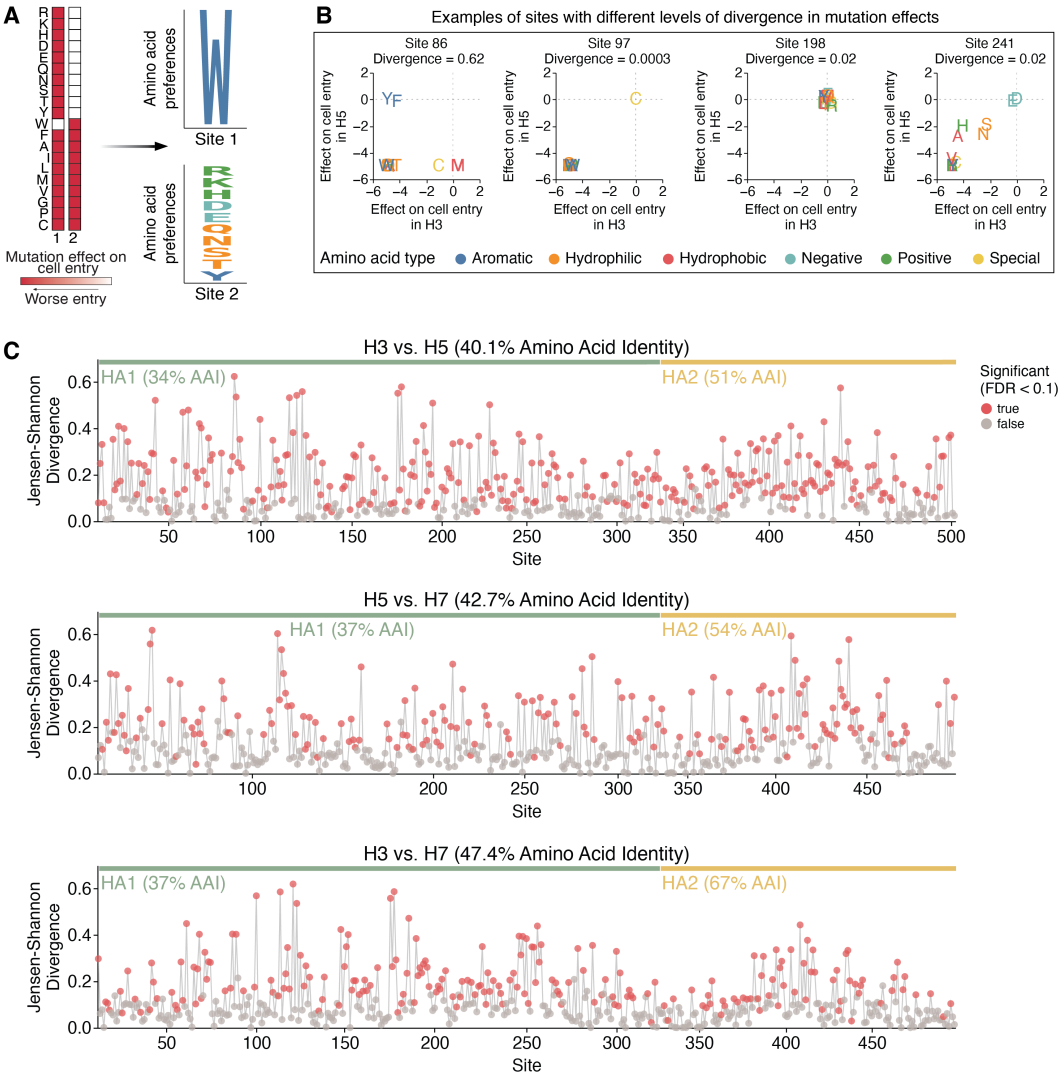

Figure 4.2: **Sequence constraints differ dramatically at many sites among H3, H5, and H7 HAs.** A) Mutation effects on cell entry at a site are converted into amino acid preferences, and the amino-acid preferences are plotted as logo plots where the height of the letter is proportional to the preference of that site for that amino acid. B) Examples of sites with different levels of Jensen-Shannon divergence in amino-acid preferences between HA subtypes. The scatter plot shows the effect of mutating to each amino acid in each of the two subtypes, with the wildtype amino-acid identity assigned an effect of zero. C) Divergence in amino-acid preferences at each site in HA between H3-H5, H5-H7, and H3-H7. Red points indicate sites where amino-acid preferences have significantly diverged (false discovery rate < 0.1) between HA subtypes.

structural or functional regions in HA. For the H3-H7 comparison, sites in HA2 domain showed lower divergence than those in the HA1 domain ($p < 0.001$, two-sided Mann-Whitney-U test, **Figure 4.7A**). In contrast, no significant differences in divergence were observed between HA1 and HA2 for the H3-H5 and H5-H7 comparisons. This pattern reflects the higher amino acid conservation (67%) of HA2 between H3-H7 versus H3-H5 and H5-7 (**Figure 4.2C**). In general, sites where amino acids are conserved between HA subtypes are typically mutationally intolerant in both subtypes (**Figure 4.7B**). Therefore, the network of interacting residues in HA2 is likely more preserved between H3-H7, but has diverged over the broader evolutionary split between group 1 and group 2 HAs.

However, phylogenetic relatedness among HAs does not always underlie divergence. In the 190-helix of the receptor-binding pocket, which overlaps with antigenic epitope B (H3 classification), sites showed the highest median divergence in amino-acid preferences in the H3–H7 comparison relative to the H3–H5 and H5–H7 comparisons (**Figure 4.7C**). In this case, divergence may instead reflect distinct selective pressures in the human and avian reservoirs that drove adaptations in receptor binding and antigenic escape.

4.2.3 Factors associated with divergence in amino-acid preferences among HA subtypes

We sought to determine what specific factors were associated with high divergence in the preferences of the same site for different amino acids across HA subtypes. Sites where the wildtype amino acid identity changed between HAs showed significantly higher divergence compared to conserved sites where the wildtype amino acids are conserved ($p = 0.03$ for H3-H5; $p < 0.001$ for H3-H7; $p < 0.001$ for H5-H7; two-sided Mann-Whitney-U test, **Figure 4.3A**. This difference likely reflects the fact that conserved sites usually cannot tolerate most mutations across HAs (**Figure 4.7B**) and suggests that the constraints imposed by interactions with neighboring residues are better preserved during the evolutionary divergence of HA subtypes. However, even sites with conserved wildtype amino-acid identities often have very different preferences between HA subtypes (**Figure 4.3A**). We therefore examined whether additional structural or biochemical features beyond conservation could help predict a site's divergence.

There is no correlation between the distance of Cα backbone atoms in structurally aligned HAs and divergence (**Figure 4.8**), indicating structural shifts in the backbone residues between HA subtypes is not a major driver of divergence in amino-acid preferences. However, among sites where the wildtype amino-acid identity changed between HAs, sites that are buried (relative solvent accessibility ≤ 0.2) showed significantly higher divergence in amino-acid preferences compared to sites that are surface exposed ($p < 0.001$ for all comparisons, two-sided Mann-Whitney-U test, **Figure 4.3B**). In contrast, among sites where the wildtype identity is conserved between HAs, solvent accessibility does not significantly explain divergence

($p > 0.1$ for all comparisons, two-sided Mann-Whitney-U test, **Figure 4.9B**). These patterns arise because conserved sites tend to be more mutationally intolerant regardless of solvent accessibility (**Figure 4.7B**), whereas variable sites that are exposed tend to be more mutationally tolerant in both HA backgrounds compared to variable sites that are buried (**Figure 4.9C**). For example, the wildtype amino acids at the exposed site 173 (relative solvent accessibility = 0.85) are Q, R, and K in H3, H5, and H7, respectively, and all measured mutations are tolerated in all backgrounds, resulting in low divergence (**Figure 4.9D**). Together, these data suggest that among variable sites where the wildtype amino acid changed, the ones with highly diverged amino-acid preferences are typically buried within the protein.

Yet while the most divergence in amino-acid preferences tends to occur at buried sites with different wildtype amino acids between subtypes, divergence still ranges widely at such sites (**Figure 4.3B**). What accounts for this variation? Again, structural deviation of the protein backbone at these sites is not strongly associated with divergence amino-acid preferences ($r < 0.1$ for all comparisons, **Figure 4.8**). However, buried sites where the wildtype amino-acid identity differs in biochemical type across subtypes show significantly higher divergence compared to sites where the wildtype amino acids are of the same type ($p < 0.01$ across all comparisons, two-sided Mann-Whitney-U test, **Figure 4.3C**). Therefore, the type of amino acid at a buried site where the wildtype identity changed across subtypes is indicative of divergence in amino-acid preferences.

The high divergence of amino-acid preferences at buried sites with different wildtype identities across HA subtypes can arise from fundamental rewiring of how sets of residues interact, even when the backbone structure has not changed. For example, the wildtype amino acids at the buried sites 123/176/178 are E/K/Y in H3, I/L/I in H5, and M/A/I in H7. The amino-acid preferences at these three sites are fairly similar between H5 and H7 HAs, but both are sharply diverged from H3 HA (**Figure 4.4A**). This high divergence of amino-acid preferences is likely because sites 123/176/178 form a hydrogen bond network in H3 HAs, but this network is absent in H5 and H7 HAs, which instead have a more hydrophobic environment in this region (**Figure 4.4B**). Collectively, the amino-acid preferences and protein structure show how contingency has rewired the evolutionary constraints in this region: H3 relies on a highly constrained hydrogen bond network to maintain cell entry function, while H5 and H7 rely on a hydrophobic environment that does not require hydrogen bonds at all.

Author contributions statement

JA, TCY, and JDB conceived the study. JA, TCY, and BD performed the experiments. TCY and JDB performed the computational analysis. JA, TCY, and JDB interpreted the results. JA, TCY, and JDB wrote the original draft.

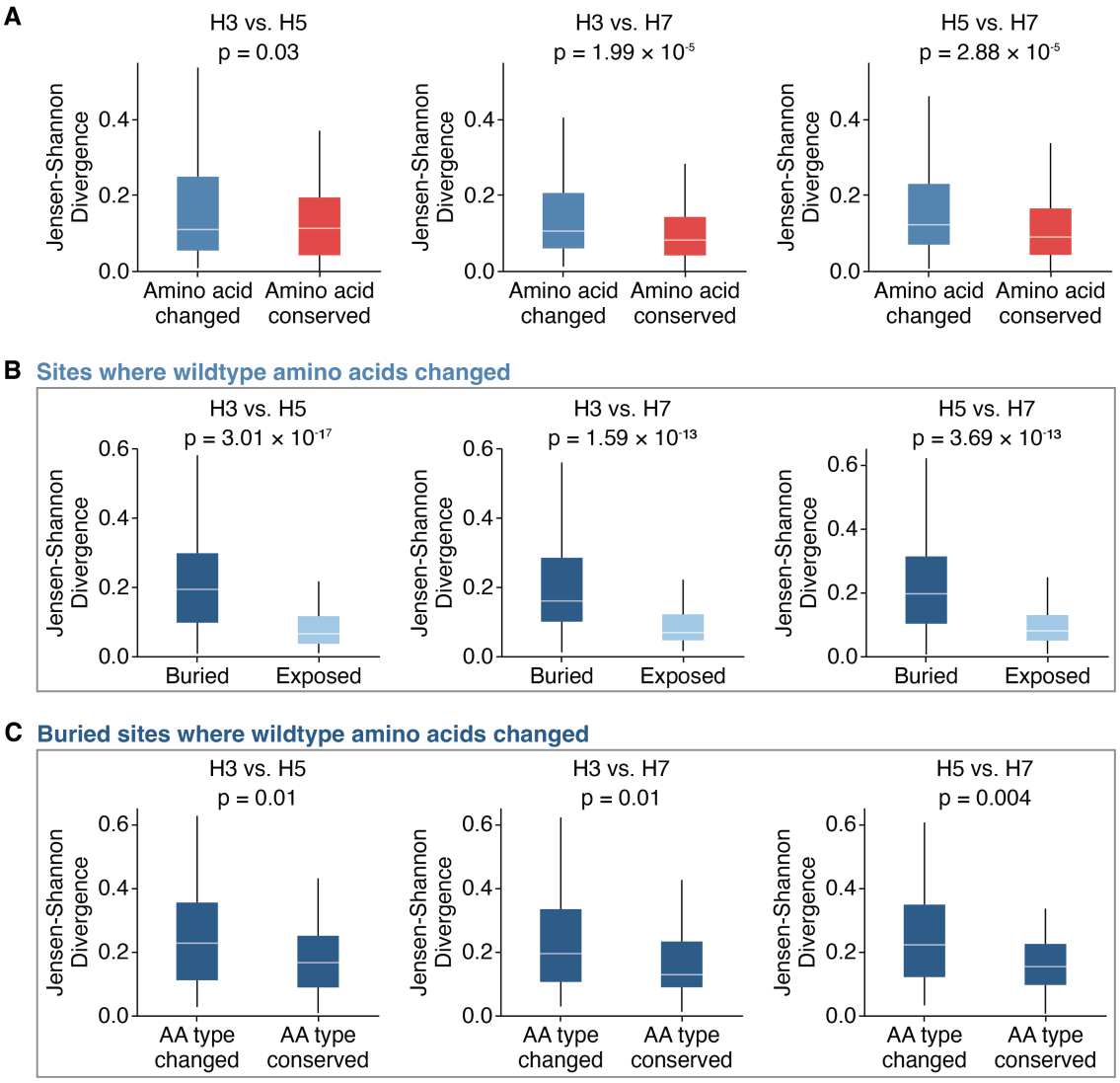

Figure 4.3: **Sites with divergent amino-acid preferences across HAs tend to be buried and have different wildtype amino-acid types.** A) Divergence in amino-acid preferences at sites where the wildtype amino-acid identity is conserved or changed between HA subtypes. B) Among sites where the wildtype identity changed, buried sites show significantly higher divergence in amino-acid preferences compared to exposed sites. Buried sites are defined as having a relative solvent accessibility < 0.2. C) Among buried sites where the wildtype amino-acid identity changed, sites where the wildtype amino-acid type is different (e.g., hydrophobic versus hydrophilic) show significantly higher divergence compared to sites where the amino acid type is conserved. Two-sided Mann-Whitney-U test was used for significance testing.

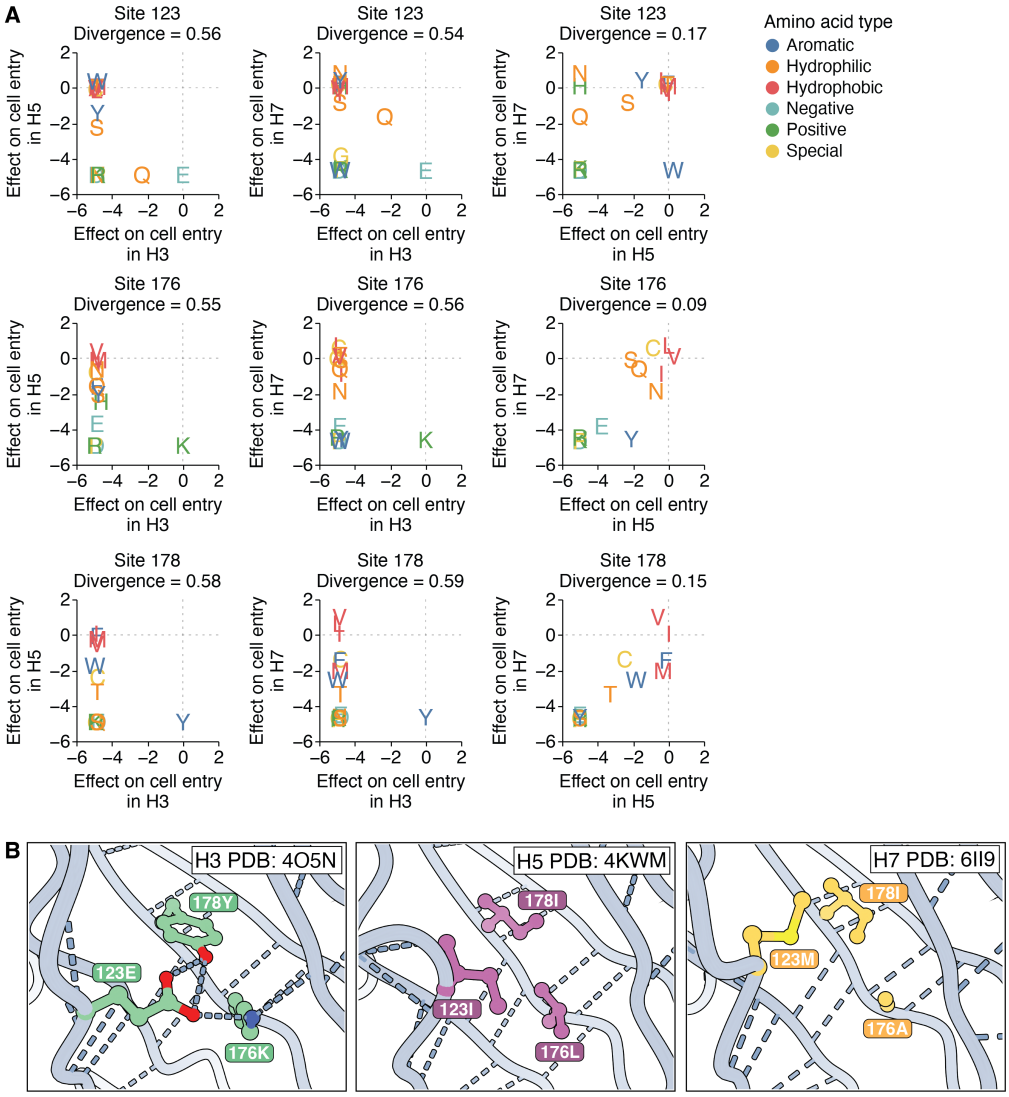

Figure 4.4: **Example of contacting sites where interactions have been rewired from a hydrogen bond network in H3 HA to a hydrophobic environment in H5 and H7 HAs.** A) Effects of mutations on cell entry between pairs of HAs at the buried sites 123, 176, and 178. The amino-acid preferences at these sites are relatively similar between H5 and H7, but both are highly diverged from H3 HA. B) Sites 123, 176, and 178 form a hydrogen bond network in H3, but are part of a hydrophobic environment in H5 and H7 HAs.

4.3 Supplementary Material

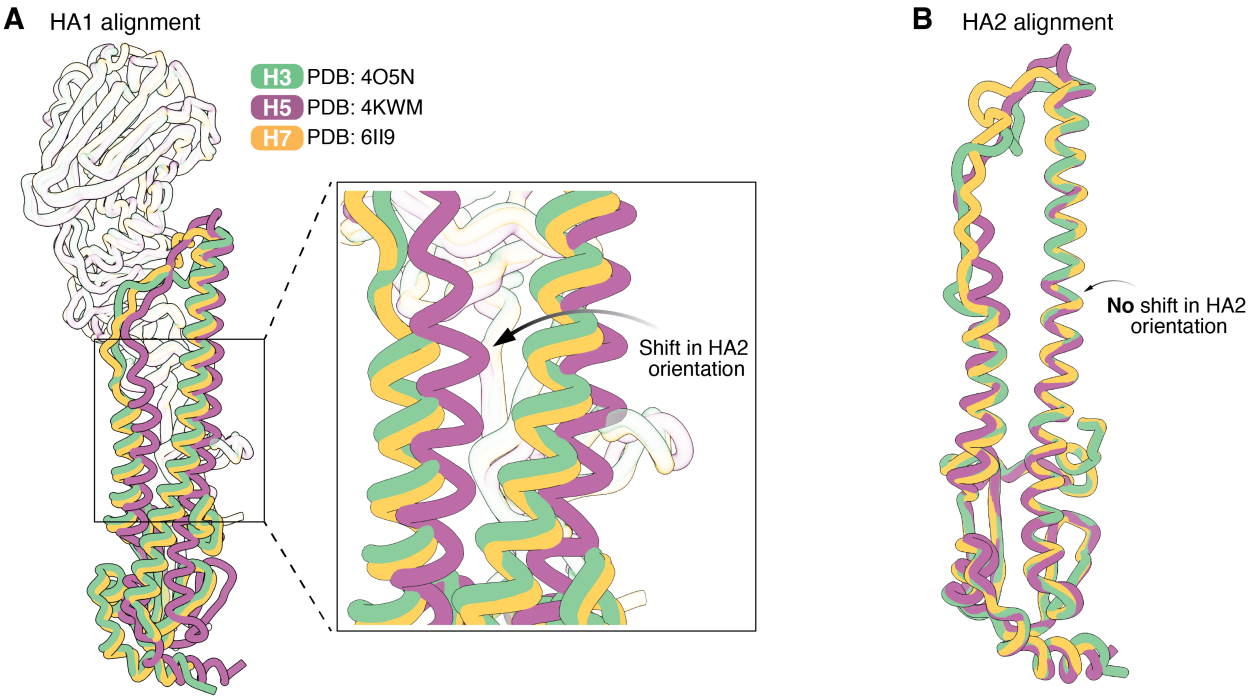

Figure 4.5: **The relative orientations of HA1 and HA2 are shifted in H5 HA relative to H3 and H7 HAs.** A) Structural alignment of the HA1 domain (same as left structure in **Figure 4.1C**) with the HA2 domains from H3 (green), H5 (purple), and H7 (orange) HAs. Due to a tilt in the orientation of the HA1 and HA2 domains, the HA2 domain of H5 becomes shifted relative to where the HA2 domains of H3 and H7 are located. B) Aligning the HA2 domain alone (same as right structure in **Figure 4.1C**) reveals the folds in HA2 are actually highly conserved across H3, H5, and H7.

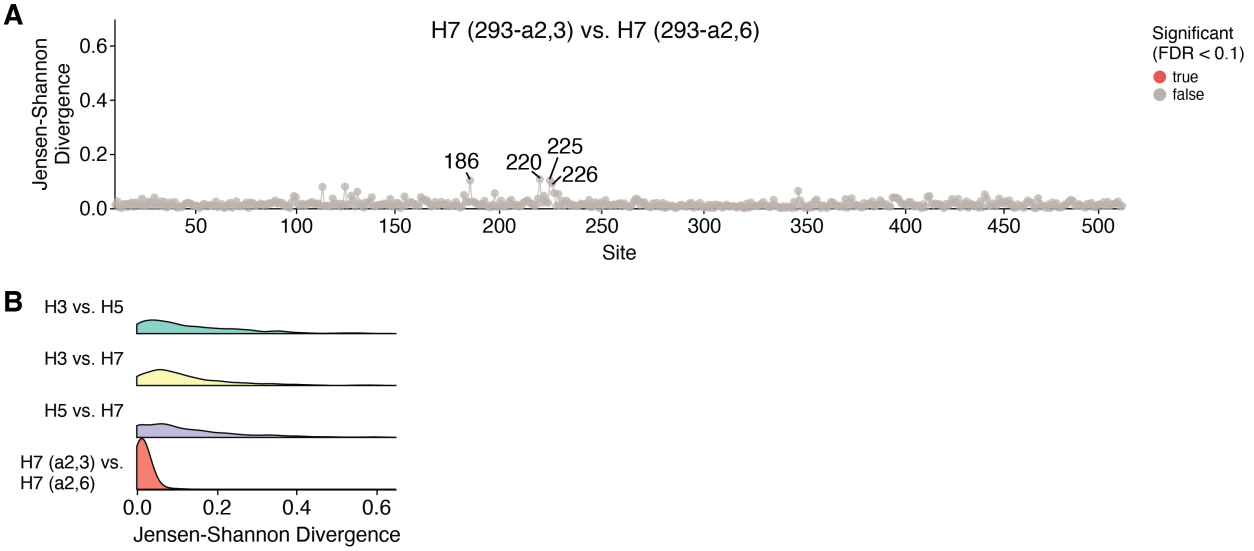

Figure 4.6: **Divergence in H7 HA amino-acid preferences for entry into 293 cells expressing α2-3 versus α2-6 linked sialic acids is minimal compared to the divergence between HA subtypes.** A) Divergence in amino-acid preferences at each site of the H7 HA as measured in 293 cells expressing only α2-3 versus only α2-6 linked sialic acids. Note that the divergence at all sites is low compared to the cross HA-subtype comparisons in **Figure 4.2C**, and no sites are significantly diverged (false discovery rate < 0.1). The largest differences are at sites like 186, 220, 225, and 226, which are important for receptor binding. B) Distributions of divergence in amino-acid preferences for all sites between subtypes compared to the distribution of divergence in H7 HA for measurement made using 293 cells expressing entry only α2-3 versus only α2-6 linked sialic acids.

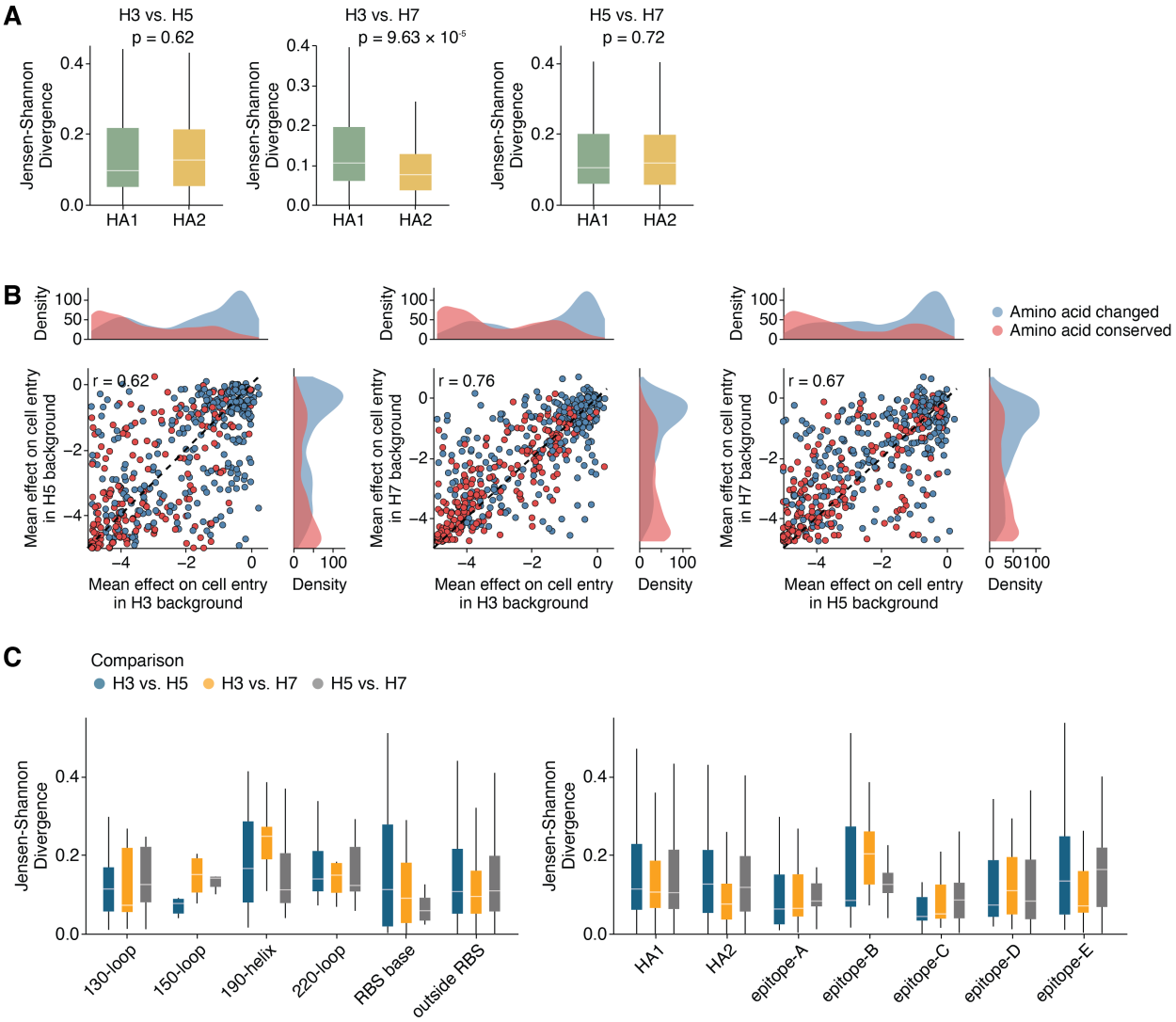

Figure 4.7: **Divergence in amino-acid preferences for different domains or regions of HA.** A) Distributions of divergence in amino-acid preferences between HA subtypes for sites in the HA1 or HA2 domains of HA. In H3-H7, HA2 sites show significantly lower divergence compared to HA1. B) Correlation of the mean effect of mutations at each site between each pair of HA subtypes. Sites where the wildtype amino-acid identity differs between subtypes are colored blue, while sites with conserved wildtype amino-acid identities are red. C) Distributions of divergence in the amino-acid preferences by receptor binding pocket region (left) and antigenic region (right) across each HA comparison.

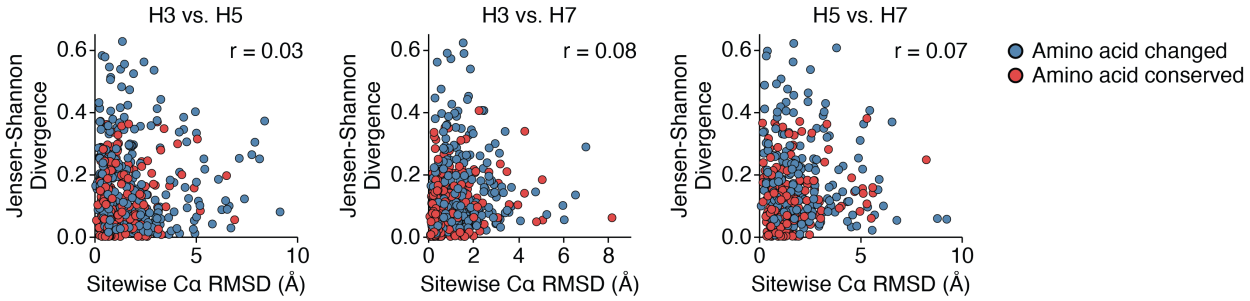

Figure 4.8: **Structural deviation is a poor predictor of divergence in amino-acid preferences at a site.** Correlation between divergence in amino-acid preferences and the Cα root mean square deviation at each site in the structurally aligned backbones of HA1 and HA2 across pairwise HA comparisons. Sites where the wildtype amino acids changed between subtypes are colored blue, while conserved sites are red.

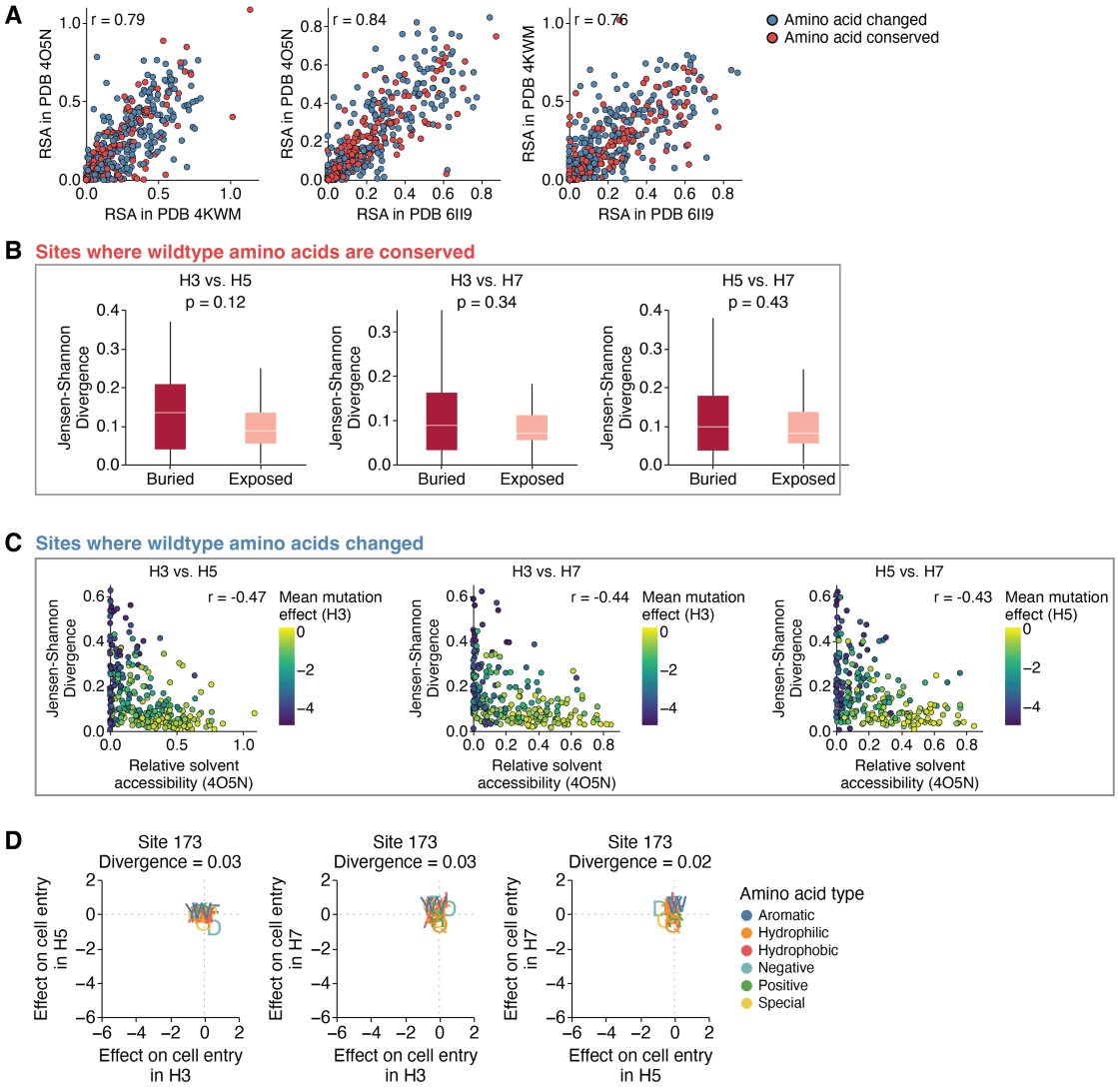

Figure 4.9: **Surface exposed sites are more mutationally tolerant and display less divergent amino acid preferences across HAs.** A) Correlation between relative solvent accessibility values at structurally aligned sites between HAs. These values quantify how exposed or buried a site is, and the correlation is strong ($r > 0.75$) because the HA structures are conserved. PDB accessions are 4O5N (H_3), 4KWM (H_5), 6II9 and (H_7). B) Among sites where the wildtype amino-acid identity is conserved (red boxplots in **Figure 4.3A**), there is no significant difference in divergence in amino-acid preferences at buried versus exposed sites. C) Among sites where the wildtype amino-acid identity changed (blue boxplots in **Figure 4.3A**), there is a negative correlation between divergence in amino-acid preferences and relative solvent accessibility. Sites are colored by mean mutation effect on entry in the indicated HA background, showing that sites that are more exposed tend to tolerate mutations better. D) Correlations of effects of mutations on cell entry between HAs at the exposed site 173, showing how all measured mutations are tolerated across HAs at this site. Two-sided Mann-Whitney-U test was used for all significance testing.

Chapter 5

Conclusion

> 山重水复疑无路，柳暗花明又一村 (Approaching the end of mountains and streams, I suspect I have reached a dead end. Dark willows, bright flowers, and another village come into view.) — Lu You, translated by Isabelle Wald

Viral protein evolution is shaped by epistasis and pleiotropy. In **chapter 2**, we developed an interpretable biophysical model that captures how epistatic interactions among viral mutations determines escape from polyclonal antibodies. In **chapter 3**, we showed how the antigenic evolution of human influenza HA is constrained by pleiotropic conflicts, and the extent to which these conflicts can be alleviated by epistasis depends on the underlying phenotype. In **chapter 4**, we discovered that the amino-acid preferences of a large fraction of sites in HA have diverged across three influenza HA subtypes.

Final publications often present science in a linear fashion, but I have learned the process rarely works that way. I faced countless experimental hurdles and setbacks over the course of graduate school. Each one challenged me to reframe which biological questions mattered and when to pivot. I remember when I first started performing deep mutational scanning experiments, I was determined to map how mutations to influenza HA affect escape from dozens of human sera and use those data to inform surveillance and forecasting efforts. But when I got my first set of data back, the strongest escape mutations weren't in HA's classic antigenic regions. Instead, they were at sites that have never changed during evolution. I was baffled and assumed I'd hit some sort of dead end. Instead of mapping more sera as I originally intended, Jesse suggested I test a different phenotype, HA acid stability. That turned out to be the best thing I could've done. Many of those strong escape mutations at conserved sites I observed earlier actually had destabilizing effects on HA. All of a sudden things started to click and I saw a path to what became **chapter 3**. In that spirit, this conclusion summarizes the applications of my findings, some of the outstanding questions they pose, and where I think the path could lead next.

5.0.1 Applications of the biophysical model of polyclonal antibody escape

In **chapter 2**, we developed a biophysical model that infers mutation effects on antibody escape from deep mutational scanning data. Although the model was originally developed for the purpose of analyzing mutational escape from polyclonal antibodies, it has also proven extremely useful for analyzing mutational escape from monoclonal antibodies. In this case, models are fit with a single epitope rather than multiple epitopes. Across many deep mutational scanning studies of diverse viral entry proteins, inferred antibody escape effects correlate well with changes in antibody neutralization potency measured in independent assays [29, 86, 19, 1].

The model has also been useful for deconvolving polyclonal sera. Radford et al. used deep mutational scanning to map how mutations to the HIV envelope escape sera collected from individuals living with HIV [133]. One of those sera was found to possess neutralizing antibodies targeting two distinct epitopes on the envelope. Since the deep mutational scanning library contained HIV envelope variants containing multiple mutations, the model inferred that some combinations of mutations could have redundant or synergistic effects on escape. These predictions were validated using independent neutralization assays, demonstrating how complex interactions among mutations can be explained by a simple biophysical model.

However, in other cases, it has been difficult to deconvolve polyclonal sera into distinct epitopes. For instance, Welsh et al. used deep mutational scanning to map how mutations to the influenza H3 HA escape human sera, but the model could only fit mutation effects to a single epitope [174]. There are a few compelling reasons for why this could be the case. First, neutralizing antibody responses to influenza may be especially narrow and genuinely target a single epitope. In fact, there is evidence that the influenza-specific serum antibody repertoire is oligoclonal [89]. On the other hand, the variants in the library may be uninformative. Although the library contained around 30,000 functional HA variants with an average of 3 mutations per gene, this is a vanishingly small fraction of the number of possible variants that are a handful of mutations away from the reference strain. In order for the model to deconvolve epitopes, it must observe the correct combinations of mutations at the particular sites targeted by antibodies in the sera. The chance of that happening is low. Unfortunately, we remain restricted by the size of deep mutational scanning libraries, which is limited by the cost of DNA synthesis, the cost of DNA sequencing, and viral library titers. Lastly, the biological assumptions of our model could be unideal or wrong. Our model assumes antibodies can target distinct epitopes without competition, but it could be that many epitopes are overlapping. Our model also assumes that antibody binding at one epitope does not influence the binding affinity of antibodies at other epitopes. Future work is needed to clarify the accuracy of these assumptions. While it was not possible to deconvolve sera into distinct epitopes in Welsh et al., the escape effects inferred by the single epitope model still correlated very well with changes in sera neutral-

ization potency, and the study overall showed how antigenic pressure varies across different age groups [174]. Another work that performed deep mutational scanning of SARS-CoV-2 Spike also could not deconvolve human sera, but likewise the inferred escape effects still correlated very well with independent neutralization assays and proved useful for predicting the evolution of SARS-CoV-2 clades [28].

5.0.2 Can beneficial mutations that pleiotropically decrease HA acid stability be alleviated by epistasis?

In **chapter 3**, we found that some human sera contain neutralizing antibodies targeting conserved sites in H3 HA. Mutations at those sites can escape the antibodies, but pleiotropically reduce HA acid stability. Why have these beneficial antigenic mutations never fixed in nature? Our hypothesis is that when a mutation destabilizes HA, there does not exist a set of permissive mutations within the local genotypic neighborhood that can alleviate the destabilizing effect. Therefore, while the mutation would be beneficial from an antigenic perspective, there is no solution in accessible sequence space to introduce it. If this is true, it also indicates that mutation effects on acid stability may be more consistent across genetic backgrounds, a view that is supported by our analysis of evolutionary entrenchment. An experiment that directly tests this idea could involve using deep mutational scanning to measure the effects of mutations in the background of multiple historical H3 HAs. The expectation then would be that mutation effects on acid stability are the same across backgrounds, whereas many mutation effects on cell entry differ due to epistasis.

Another reason why these antigenic mutations never fix in nature might stem from the extent of immune pressure. Two of the four serum samples in **chapter 3** possessed neutralizing antibodies against these conserved sites, but what fraction of the population actually has these antibodies? If these antibodies are rare, then the fitness gain from escaping them would be marginal. On the other hand, if these antibodies are prevalent, then it would strengthen our conclusion that acid stability is a difficult pleiotropic constraint to overcome. Future serological work involving large cohorts of individuals will be needed to figure this out. From a therapeutics standpoint, it will also be interesting to test if these antibodies are protective in humans. In the end, monoclonal antibody therapeutics or vaccines designed to elicit antibodies targeting these conserved sites could be more resistant to viral evolution and antigenic drift.

5.0.3 What are other pleiotropic constraints on HA evolution?

In **chapter 3**, we explored how cell entry, acid stability, and neutralization by human sera constrain HA evolution, but what other hidden dimensions in phenotypic space play a role? One relevant phenotype is mucin evasion. Mucins are sialylated macromolecules and act as decoy receptors. As influenza viruses

enter the respiratory tract, the HA is under selection to balance binding to host cell sialic acid receptors while minimizing interaction with the surrounding mucus layer [190]. Importantly, NA also plays a role in this trade-off, as it can help to cleave mucins. Using deep mutational scanning to map how well mutations escape mucins is a promising future direction that will likely reveal pleiotropic conflicts (e.g., a mutation that escapes mucins, but at the cost of receptor binding).

The most relevant phenotype for predicting HA evolution is immune escape. Yet, each person's antibodies are their own unique snowflake. While the antibody repertoires of individuals can be collapsed onto fewer axes by factors like age, these cohort-level repertoires still represent many independent phenotypes. A key unanswered question is how HA evolves in this heterogeneous immune landscape. Does HA prefer selecting for 'generalist' mutations that modestly escape a broad spectrum of antibodies in the population, or does it select for 'specialist' mutations that strongly escape a small subset of antibodies in the population? Where evolution is optimized on this wavelength could depend on the diversity of antibodies in the population. A less diverse immune landscape could favor more pleiotropic mutations that escape many antibodies. However, as diversity in the immune landscape increases, mutations that escape many antibodies could become rare or costly (i.e., much smaller shift in neutralization). In this regime, evolution may instead select for modular mutations that have a large shift in neutralization from specific antibodies, while having no effect on neutralization from most other antibodies.

Bibliography

[1] Arjun K Aditham, Caelan E Radford, Caleb R Carr, Naveen Jasti, Neil P King, and Jesse D Bloom. Deep mutational scanning of rabies glycoprotein defines mutational constraint and antibody-escape mutations. *Cell Host Microbe*, 33(6):988–1003.e10, June 2025.

[2] Sarah F Andrews, Yunping Huang, Kaval Kaur, Lyubov I Popova, Irvin Y Ho, Noel T Pauli, Carole J Henry Dunand, William M Taylor, Samuel Lim, Min Huang, Xinyan Qu, Jane-Hwei Lee, Marlene Salgado-Ferrer, Florian Krammer, Peter Palese, Jens Wrammert, Rafi Ahmed, and Patrick C Wilson. Immune history profoundly affects broadly protective B cell responses to influenza. *Sci. Transl. Med.*, 7(316):316ra192, December 2015.

[3] Philip Arevalo, Huong Q McLean, Edward A Belongia, and Sarah Cobey. Earliest infections predict the age distribution of seasonal influenza a cases. *Elife*, 9(e50060), July 2020.

[4] Guadalupe Ayora-Talavera, Holly Shelton, Margaret A Scull, Junyuan Ren, Ian M Jones, Raymond J Pickles, and Wendy S Barclay. Mutations in H5N1 influenza virus hemagglutinin that confer binding to human tracheal airway epithelium. *PLoS One*, 4(11):e7836, November 2009.

[5] Prasith Baccam, Catherine Beauchemin, Catherine A Macken, Frederick G Hayden, and Alan S Perelson. Kinetics of influenza a virus infection in humans. *J. Virol.*, 80(15):7590–7599, August 2006.

[6] Amy L Baker, Bailey Arruda, Mitchell V Palmer, Paola Boggiatto, Kaitlyn Sarlo Davila, Alexandra Buckley, Giovana Ciacci Zanella, Celeste A Snyder, Tavis K Anderson, Carl R Hutter, Thao-Quyen Nguyen, Alexey Markin, Kristina Lantz, Erin A Posey, Mia Kim Torchetti, Suelee Robbe-Austerman, Drew R Magstadt, and Patrick J Gorden. Dairy cows inoculated with highly pathogenic avian influenza virus H5N1. *Nature*, 637(8047):913–920, January 2025.

[7] Sandhya Bangaru, Shanshan Lang, Michael Schotsaert, Hillary A Vanderven, Xueyong Zhu, Nurgun Kose, Robin Bombardi, Jessica A Finn, Stephen J Kent, Pavlo Gilchuk, Iuliia Gilchuk, Hannah L Turner, Adolfo García-Sastre, Sheng Li, Andrew B Ward, Ian A Wilson, and James E Crowe,

Jr. A site of vulnerability on the influenza virus hemagglutinin head domain trimer interface. *Cell*, 177(5):1136–1152.e18, May 2019.

[8] Christopher O Barnes, Claudia A Jette, Morgan E Abernathy, Kim-Marie A Dam, Shannon R Esswein, Harry B Gristick, Andrey G Malyutin, Naima G Sharaf, Kathryn E Huey-Tubman, Yu E Lee, Davide F Robbiani, Michel C Nussenzweig, Anthony P West, Jr, and Pamela J Bjorkman. SARS-CoV-2 neutralizing antibody structures inform therapeutic strategies. *Nature*, 588(7839):682–687, December 2020.

[9] Trevor Bedford, Marc A Suchard, Philippe Lemey, Gytis Dudas, Victoria Gregory, Alan J Hay, John W McCauley, Colin A Russell, Derek J Smith, and Andrew Rambaut. Integrating influenza antigenic dynamics with molecular evolution. *Elife*, 3:e01914, February 2014.

[10] Donald J Benton, Steven J Gamblin, Peter B Rosenthal, and John J Skehel. Structural transitions in influenza haemagglutinin at membrane fusion pH. *Nature*, 583(7814):150–153, July 2020.

[11] Jesse D Bloom, Lizhi Ian Gong, and David Baltimore. Permissive secondary mutations enable the evolution of influenza oseltamivir resistance. *Science*, 328(5983):1272–1275, June 2010.

[12] Jesse D Bloom, Sy T Labthavikul, Christopher R Otey, and Frances H Arnold. Protein stability promotes evolvability. *Proc. Natl. Acad. Sci. U. S. A.*, 103(15):5869–5874, April 2006.

[13] Marcus J Bolton, Jordan T Ort, Ryan McBride, Nicholas J Swanson, Jo Wilson, Moses Awofolaju, Colleen Furey, Allison R Greenplate, Elizabeth M Drapeau, Andrew Pekosz, James C Paulson, and Scott E Hensley. Antigenic and virological properties of an H3N2 variant that continues to dominate the 2021-22 northern hemisphere influenza season. *Cell Rep.*, 39(9):110897, May 2022.

[14] Nicole M Bouvier and Peter Palese. The biology of influenza viruses. *Vaccine*, 26 Suppl 4(Suppl 4):D49–53, September 2008.

[15] Felix Broecker, Sean T H Liu, Weina Sun, Florian Krammer, Viviana Simon, and Peter Palese. Immunodominance of antigenic site B in the hemagglutinin of the current H3N2 influenza virus in humans and mice. *J. Virol.*, 92(20), October 2018.

[16] P A Bullough, F M Hughson, J J Skehel, and D C Wiley. Structure of influenza haemagglutinin at the pH of membrane fusion. *Nature*, 371(6492):37–43, September 1994.

[17] Yunlong Cao, Jing Wang, Fanchong Jian, Tianhe Xiao, Weiliang Song, Ayijiang Yisimayi, Weijin Huang, Qianqian Li, Peng Wang, Ran An, Jing Wang, Yao Wang, Xiao Niu, Sijie Yang, Hui Liang,

Haiyan Sun, Tao Li, Yuanling Yu, Qianqian Cui, Shuo Liu, Xiaodong Yang, Shuo Du, Zhiying Zhang, Xiaohua Hao, Fei Shao, Ronghua Jin, Xiangxi Wang, Junyu Xiao, Youchun Wang, and Xiaoliang Sunney Xie. Omicron escapes the majority of existing SARS-CoV-2 neutralizing antibodies. *Nature*, 602(7898):657–663, February 2022.

[18] C M Carr and P S Kim. A spring-loaded mechanism for the conformational change of influenza hemagglutinin. *Cell*, 73(4):823–832, May 1993.

[19] Caleb R Carr, Katharine H D Crawford, Michael Murphy, Jared G Galloway, Hugh K Haddox, Frederick A Matsen, 4th, Kristian G Andersen, Neil P King, and Jesse D Bloom. Deep mutational scanning reveals functional constraints and antibody-escape potential of lassa virus glycoprotein complex. *Immunity*, 57(9):2061–2076.e11, September 2024.

[20] Ning Chai, Lee R Swem, Mike Reichelt, Haiyin Chen-Harris, Elizabeth Luis, Summer Park, Ashley Fouts, Patrick Lupardus, Thomas D Wu, Olga Li, Jacqueline McBride, Michael Lawrence, Min Xu, and Man-Wah Tan. Two escape mechanisms of influenza a virus to a broadly neutralizing stalk-binding antibody. *PLoS Pathog.*, 12(6):e1005702, June 2016.

[21] Benjamin S Chambers, Kaela Parkhouse, Ted M Ross, Kevin Alby, and Scott E Hensley. Identification of hemagglutinin residues responsible for H3N2 antigenic drift during the 2014-2015 influenza season. *Cell Rep.*, 12(1):1–6, July 2015.

[22] C M Chu, I M Dawson, and W J Elford. Filamentous forms associated with newly isolated influenza virus. *Lancet*, 1(6554):602, April 1949.

[23] R B Couch and J A Kasel. Immunity to influenza in man. *Annu. Rev. Microbiol.*, 37(1):529–549, 1983.

[24] Katharine H D Crawford and Jesse D Bloom. alignparse: A python package for parsing complex features from high-throughput long-read sequencing. *J. Open Source Softw.*, 4(44), December 2019.

[25] Jerome F Cros and Peter Palese. Trafficking of viral genomic RNA into and out of the nucleus: influenza, thogoto and borna disease viruses. *Virus Res.*, 95(1-2):3–12, September 2003.

[26] Bernadeta Dadonaite, Jenny J Ahn, Jordan T Ort, Jin Yu, Colleen Furey, Annie Dosey, William W Hannon, Amy L Vincent Baker, Richard J Webby, Neil P King, Yan Liu, Scott E Hensley, Thomas P Peacock, Louise H Moncla, and Jesse D Bloom. Deep mutational scanning of H5 hemagglutinin to inform influenza virus surveillance. *PLoS Biol.*, 22(11):e3002916, November 2024.

[27] Bernadeta Dadonaite, Jack Brown, Teagan E McMahon, Ariana G Farrell, Daniel Asarnow, Cameron Stewart, Jenni Logue, Ben Murrell, Helen Y Chu, David Veesler, and Jesse D Bloom. Full-spike deep mutational scanning helps predict the evolutionary success of SARS-CoV-2 clades. *bioRxivorg*, page 2023.11.13.566961, November 2023.

[28] Bernadeta Dadonaite, Jack Brown, Teagan E McMahon, Ariana G Farrell, Marlin D Figgins, Daniel Asarnow, Cameron Stewart, Jimin Lee, Jenni Logue, Trevor Bedford, Ben Murrell, Helen Y Chu, David Veesler, and Jesse D Bloom. Spike deep mutational scanning helps predict success of SARS-CoV-2 clades. *Nature*, 631(8021):617–626, July 2024.

[29] Bernadeta Dadonaite, Katharine H D Crawford, Caelan E Radford, Ariana G Farrell, Timothy C Yu, William W Hannon, Panpan Zhou, Raiees Andrabi, Dennis R Burton, Lihong Liu, David D Ho, Helen Y Chu, Richard A Neher, and Jesse D Bloom. A pseudovirus system enables deep mutational scanning of the full SARS-CoV-2 spike. *Cell*, 186(6):1263–1278.e20, March 2023.

[30] Suman R Das, Scott E Hensley, Alexandre David, Loren Schmidt, James S Gibbs, Pere Puigbò, William L Ince, Jack R Bennink, and Jonathan W Yewdell. Fitness costs limit influenza a virus hemagglutinin glycosylation as an immune evasion strategy. *Proc. Natl. Acad. Sci. U. S. A.*, 108(51):E1417–22, December 2011.

[31] Suman R Das, Scott E Hensley, William L Ince, Christopher B Brooke, Anju Subba, Mark G Delboy, Gustav Russ, James S Gibbs, Jack R Bennink, and Jonathan W Yewdell. Defining influenza a virus hemagglutinin antigenic drift by sequential monoclonal antibody selection. *Cell Host Microbe*, 13(3):314–323, March 2013.

[32] F M Davenport, A V Hennessy, and T Francis, Jr. Epidemiologic and immunologic significance of age distribution of antibody to antigenic variants of influenza virus. *J. Exp. Med.*, 98(6):641–656, December 1953.

[33] Robert P de Vries, Wenjie Peng, Oliver C Grant, Andrew J Thompson, Xueyong Zhu, Kim M Bouwman, Alba T Torrents de la Pena, Marielle J van Breemen, Iresha N Ambepitiya Wickramasinghe, Cornelis A M de Haan, Wenli Yu, Ryan McBride, Rogier W Sanders, Robert J Woods, Monique H Verheije, Ian A Wilson, and James C Paulson. Three mutations switch H7N9 influenza to human-type receptor specificity. *PLoS Pathog.*, 13(6):e1006390, June 2017.

[34] Marciela M DeGrace, Elodie Ghedin, Matthew B Frieman, Florian Krammer, Alba Grifoni, Arghavan Alisoltani, Galit Alter, Rama R Amara, Ralph S Baric, Dan H Barouch, Jesse D Bloom, Louis-Marie Bloyet, Gaston Bonenfant, Adrianus C M Boon, Eli A Boritz, Debbie L

Bratt, Traci L Bricker, Liliana Brown, William J Buchser, Juan Manuel Carreño, Liel Cohen-Lavi, Tamarand L Darling, Meredith E Davis-Gardner, Bethany L Dearlove, Han Di, Meike Dittmann, Nicole A Doria-Rose, Daniel C Douek, Christian Drosten, Venkata-Viswanadh Edara, Ali Ellebedy, Thomas P Fabrizio, Guido Ferrari, Will M Fischer, William C Florence, Ron A M Fouchier, John Franks, Adolfo García-Sastre, Adam Godzik, Ana Silvia Gonzalez-Reiche, Aubree Gordon, Bart L Haagmans, Peter J Halfmann, David D Ho, Michael R Holbrook, Yaoxing Huang, Sarah L James, Lukasz Jaroszewski, Trushar Jeevan, Robert M Johnson, Terry C Jones, Astha Joshi, Yoshihiro Kawaoka, Lisa Kercher, Marion P G Koopmans, Bette Korber, Eilay Koren, Richard A Koup, Eric B LeGresley, Jacob E Lemieux, Mariel J Liebeskind, Zhuoming Liu, Brandi Livingston, James P Logue, Yang Luo, Adrian B McDermott, Margaret J McElrath, Victoria A Meliopoulos, Vineet D Menachery, David C Montefiori, Barbara Mühlemann, Vincent J Munster, Jenny E Munt, Manoj S Nair, Antonia Netzl, Anna M Niewiadomska, Sijy O'Dell, Andrew Pekosz, Stanley Perlman, Marjorie C Pontelli, Barry Rockx, Morgane Rolland, Paul W Rothlauf, Sinai Sacharen, Richard H Scheuermann, Stephen D Schmidt, Michael Schotsaert, Stacey Schultz-Cherry, Robert A Seder, Mayya Sedova, Alessandro Sette, Reed S Shabman, Xiaoying Shen, Pei-Yong Shi, Maulik Shukla, Viviana Simon, Spencer Stumpf, Nancy J Sullivan, Larissa B Thackray, James Theiler, Paul G Thomas, Sanja Trifkovic, Sina Türeli, Samuel A Turner, Maria A Vakaki, Harm van Bakel, Laura A VanBlargan, Leah R Vincent, Zachary S Wallace, Li Wang, Maple Wang, Pengfei Wang, Wei Wang, Scott C Weaver, Richard J Webby, Carol D Weiss, David E Wentworth, Stuart M Weston, Sean P J Whelan, Bradley M Whitener, Samuel H Wilks, Xuping Xie, Baoling Ying, Hyejin Yoon, Bin Zhou, Tomer Hertz, Derek J Smith, Michael S Diamond, Diane J Post, and Mehul S Suthar. Defining the risk of SARS-CoV-2 variants on immune protection. *Nature*, 605(7911):640–652, May 2022.

[35] A S Dingens, H K Haddox, J Overbaugh, and J D Bloom. Comprehensive mapping of HIV-1 escape from a broadly neutralizing antibody. *Cell host & microbe*, 21(6):777–787, 2017.

[36] Michael B Doud and J Bloom. Accurate measurement of the effects of all amino-acid mutations on influenza hemagglutinin. *Viruses*, 8(6):155, June 2016.

[37] Michael B Doud, Scott E Hensley, and Jesse D Bloom. Complete mapping of viral escape from neutralizing antibodies. *PLoS Pathog.*, 13(3):e1006271, March 2017.

[38] Michael B Doud, Juhye M Lee, and J Bloom. How single mutations affect viral escape from broad and narrow antibodies to H1 influenza hemagglutinin. *Nat. Commun.*, 9(1):1386, April 2018.

[39] Rachel T Eguia, Katharine H D Crawford, Terry Stevens-Ayers, Laurel Kelnhofer-Millevolte,

Alexander L Greninger, Janet A Englund, Michael J Boeckh, and Jesse D Bloom. A human coronavirus evolves antigenically to escape antibody immunity. *PLoS Pathog.*, 17(4):e1009453, April 2021.

[40] Tal Einav and Jesse D Bloom. When two are better than one: Modeling the mechanisms of antibody mixtures. *PLoS Comput. Biol.*, 16(5):e1007830, May 2020.

[41] Stefan Elbe and Gemma Buckland-Merrett. Data, disease and diplomacy: GISAID's innovative contribution to global health: Data, disease and diplomacy. *Global Chall.*, 1(1):33–46, January 2017.

[42] Ronald Aylmer Fisher. *The genetical theory of natural selection*. Clarendon Press, Oxford, 1930.

[43] W M Fitch, R M Bush, C A Bender, and N J Cox. Long term trends in the evolution of H(3) HA1 human influenza type a. *Proc. Natl. Acad. Sci. U. S. A.*, 94(15):7712–7718, July 1997.

[44] J M Fonville, S H Wilks, S L James, A Fox, M Ventresca, M Aban, L Xue, T C Jones, N M H Le, Q T Pham, N D Tran, Y Wong, A Mosterin, L C Katzelnick, D Labonte, T T Le, G van der Net, E Skepner, C A Russell, T D Kaplan, G F Rimmelzwaan, N Masurel, J C de Jong, A Palache, W E P Beyer, Q M Le, T H Nguyen, H F L Wertheim, A C Hurt, A D M E Osterhaus, I G Barr, R A M Fouchier, P W Horby, and D J Smith. Antibody landscapes after influenza virus infection or vaccination. *Science*, 346(6212):996–1000, November 2014.

[45] Douglas M Fowler, Carlos L Araya, Sarel J Fleishman, Elizabeth H Kellogg, Jason J Stephany, David Baker, and Stanley Fields. High-resolution mapping of protein sequence-function relationships. *Nat. Methods*, 7(9):741–746, September 2010.

[46] Thomas Francis. On the doctrine of original antigenic sin. *Proc. Am. Philos. Soc.*, 104(6):572–578, 1960.

[47] Aaron M Frutos, Seana Cleary, Emily L Reeves, Haris M Ahmad, Ashley M Price, Wesley H Self, Yuwei Zhu, Basmah Safdar, Ithan D Peltan, Kevin W Gibbs, Matthew C Exline, Adam S Lauring, Sarah W Ball, Malini DeSilva, Sara Y Tartof, Kristin Dascomb, Stephanie A Irving, Nicola P Klein, Brian E Dixon, Toan C Ong, Ivana A Vaughn, Stacey L House, Kiran A Faryar, Mary Patricia Nowalk, Manjusha Gaglani, Karen J Wernli, Vel Murugan, Olivia L Williams, Rangaraj Selvarangan, Geoffrey A Weinberg, Mary A Staat, Natasha B Halasa, Leila C Sahni, Marian G Michaels, Janet A Englund, Marie K Kirby, Diya Surie, Fatimah S Dawood, Benjamin R Clopper, Heidi L Moline, Ruth Link-Gelles, Amanda B Payne, Elizabeth Harker, Kristina Wielgosz,

Zachary A Weber, Duck-Hye Yang, Nathaniel M Lewis, Jennifer DeCuir, Samantha M Olson, Jessie R Chung, Brendan Flannery, Lisa A Grohskopf, Carrie Reed, Shikha Garg, Sascha Ellington, and CDC Influenza Vaccine Effectiveness Collaborators. Interim estimates of 2024-2025 seasonal influenza vaccine effectiveness - four vaccine effectiveness networks, united states, october 2024-february 2025. *MMWR Morb. Mortal. Wkly. Rep.*, 74(6):83–90, February 2025.

[48] Alain Gagnon, Enrique Acosta, Stacey Hallman, Robert Bourbeau, Lisa Y Dillon, Nadine Ouellette, David J D Earn, D Ann Herring, Kris Inwood, Joaquin Madrenas, and Matthew S Miller. Pandemic paradox: Early life H2N2 pandemic influenza infection enhanced susceptibility to death during the 2009 H1N1 pandemic. *MBio*, 9(1), January 2018.

[49] Alain Gagnon, Matthew S Miller, Stacey A Hallman, Robert Bourbeau, D Ann Herring, David J D Earn, and Joaquín Madrenas. Age-specific mortality during the 1918 influenza pandemic: unravelling the mystery of high young adult mortality. *PLoS One*, 8(8):e69586, August 2013.

[50] Summer E Galloway, Mark L Reed, Charles J Russell, and David A Steinhauer. Influenza HA subtypes demonstrate divergent phenotypes for cleavage activation and pH of fusion: implications for host range and adaptation. *PLoS Pathog.*, 9(2):e1003151, February 2013.

[51] Steven J Gamblin, Sébastien G Vachieri, Xiaoli Xiong, Jie Zhang, Stephen R Martin, and John J Skehel. Hemagglutinin structure and activities. *Cold Spring Harb. Perspect. Med.*, 11(10):a038638, October 2021.

[52] Efstathios S Giotis, George Carnell, Erik F Young, Saleena Ghanny, Patricia Soteropoulos, Lin-Fa Wang, Wendy S Barclay, Michael A Skinner, and Nigel Temperton. Entry of the bat influenza H17N10 virus into mammalian cells is enabled by the MHC class II HLA-DR receptor. *Nat. Microbiol.*, 4(12):2035–2038, December 2019.

[53] L Godley, J Pfeifer, D Steinhauer, B Ely, G Shaw, R Kaufmann, E Suchanek, C Pabo, J J Skehel, and D C Wiley. Introduction of intersubunit disulfide bonds in the membrane-distal region of the influenza hemagglutinin abolishes membrane fusion activity. *Cell*, 68(4):635–645, February 1992.

[54] Lizhi Ian Gong, Marc A Suchard, and Jesse D Bloom. Stability-mediated epistasis constrains the evolution of an influenza protein. *Elife*, 2:e00631, May 2013.

[55] Katelyn M Gostic, Monique Ambrose, Michael Worobey, and James O Lloyd-Smith. Potent protection against H5N1 and H7N9 influenza via childhood hemagglutinin imprinting. *Science*, 354(6313):722–726, November 2016.

[56] Katelyn M Gostic, Rebecca Bridge, Shane Brady, Cécile Viboud, Michael Worobey, and James O Lloyd-Smith. Childhood immune imprinting to influenza a shapes birth year-specific risk during seasonal H1N1 and H3N2 epidemics. *PLoS Pathog.*, 15(12):e1008109, December 2019.

[57] Sigrid Gouma, Kangchon Kim, Madison E Weirick, Megan E Gumina, Angela Branche, David J Topham, Emily T Martin, Arnold S Monto, Sarah Cobey, and Scott E Hensley. Middle-aged individuals may be in a perpetual state of H3N2 influenza virus susceptibility. *Nat. Commun.*, 11(1):4566, September 2020.

[58] A J Greaney, A N Loes, K H Crawford, T N Starr, K D Malone, H Y Chu, and J D Bloom. Comprehensive mapping of mutations in the SARS-CoV-2 receptor-binding domain that affect recognition by polyclonal human plasma antibodies. *Cell host & microbe*, 29(3):463–476, 2021.

[59] A J Greaney, T N Starr, P Gilchuk, S J Zost, E Binshtein, A N Loes, and Bloom J. Complete mapping of mutations to the SARS-CoV-2 spike receptor-binding domain that escape antibody recognition. *Cell host & microbe*, 29(1):44–57, 2021.

[60] Allison J Greaney, Tyler N Starr, Christopher O Barnes, Yiska Weisblum, Fabian Schmidt, Marina Caskey, Christian Gaebler, Alice Cho, Marianna Agudelo, Shlomo Finkin, Zijun Wang, Daniel Poston, Frauke Muecksch, Theodora Hatziioannou, Paul D Bieniasz, Davide F Robbiani, Michel C Nussenzweig, Pamela J Bjorkman, and Jesse D Bloom. Mapping mutations to the SARS-CoV-2 RBD that escape binding by different classes of antibodies. *Nat. Commun.*, 12(1):4196, July 2021.

[61] Allison J Greaney, Tyler N Starr, and Jesse D Bloom. An antibody-escape estimator for mutations to the SARS-CoV-2 receptor-binding domain. *Virus Evol.*, 8(1):veac021, May 2022.

[62] Hugh K Haddox, Jared G Galloway, Bernadeta Dadonaite, Jesse D Bloom, Frederick A Matsen, Iv, and William S DeWitt. Jointly modeling deep mutational scans identifies shifted mutational effects among SARS-CoV-2 spike homologs. *bioRxivorg*, page 2023.07.31.551037, August 2023.

[63] Kathy Hancock, Vic Veguilla, Xiuhua Lu, Weimin Zhong, Eboneé N Butler, Hong Sun, Feng Liu, Libo Dong, Joshua R DeVos, Paul M Gargiullo, T Lynnette Brammer, Nancy J Cox, Terrence M Tumpey, and Jacqueline M Katz. Cross-reactive antibody responses to the 2009 pandemic H1N1 influenza virus. *N. Engl. J. Med.*, 361(20):1945–1952, November 2009.

[64] William T Harvey, Donald J Benton, Victoria Gregory, James P J Hall, Rodney S Daniels, Trevor Bedford, Daniel T Haydon, Alan J Hay, John W McCauley, and Richard Reeve. Identification

of low- and high-impact hemagglutinin amino acid substitutions that drive antigenic drift of influenza a(H1N1) viruses. *PLoS Pathog.*, 12(4):e1005526, April 2016.

[65] Nicholas S Heaton, David Sachs, Chi-Jene Chen, Rong Hai, and Peter Palese. Genome-wide mutagenesis of influenza virus reveals unique plasticity of the hemagglutinin and NS1 proteins. *Proc. Natl. Acad. Sci. U. S. A.*, 110(50):20248–20253, December 2013.

[66] Scott E Hensley, Suman R Das, Adam L Bailey, Loren M Schmidt, Heather D Hickman, Akila Jayaraman, Karthik Viswanathan, Rahul Raman, Ram Sasisekharan, Jack R Bennink, and Jonathan W Yewdell. Hemagglutinin receptor binding avidity drives influenza a virus antigenic drift. *Science*, 326(5953):734–736, October 2009.

[67] Brian Hie, Ellen D Zhong, Bonnie Berger, and Bryan Bryson. Learning the language of viral evolution and escape. *Science*, 371(6526):284–288, January 2021.

[68] Kathryn A Hooper and Jesse D Bloom. A mutant influenza virus that uses an N1 neuraminidase as the receptor-binding protein. *J. Virol.*, 87(23):12531–12540, December 2013.

[69] Kuan-Ying A Huang, Pramila Rijal, Haihai Jiang, Beibei Wang, Lisa Schimanski, Tao Dong, Yo-Min Liu, Pengxiang Chang, Munir Iqbal, Mu-Chun Wang, Zhihai Chen, Rui Song, Chung-Chi Huang, Jeng-How Yang, Jianxun Qi, Tzou-Yien Lin, Ang Li, Timothy J Powell, Jia-Tsrong Jan, Che Ma, George F Gao, Yi Shi, and Alain R Townsend. Structure-function analysis of neutralizing antibodies to H7N9 influenza from naturally infected humans. *Nat. Microbiol.*, 4(2):306–315, February 2019.

[70] Yoshitaka Iba, Yoshifumi Fujii, Nobuko Ohshima, Tomomi Sumida, Ritsuko Kubota-Koketsu, Mariko Ikeda, Motoaki Wakiyama, Mikako Shirouzu, Jun Okada, Yoshinobu Okuno, Yoshikazu Kurosawa, and Shigeyuki Yokoyama. Conserved neutralizing epitope at globular head of hemagglutinin in H3N2 influenza viruses. *J. Virol.*, 88(13):7130–7144, July 2014.

[71] A Danielle Iuliano, Katherine M Roguski, Howard H Chang, David J Muscatello, Rakhee Palekar, Stefano Tempia, Cheryl Cohen, Jon Michael Gran, Dena Schanzer, Benjamin J Cowling, Peng Wu, Jan Kyncl, Li Wei Ang, Minah Park, Monika Redlberger-Fritz, Hongjie Yu, Laura Espenhain, Anand Krishnan, Gideon Emukule, Liselotte van Asten, Susana Pereira da Silva, Suchunya Aungkulanon, Udo Buchholz, Marc-Alain Widdowson, Joseph S Bresee, and Global Seasonal Influenza-associated Mortality Collaborator Network. Estimates of global seasonal influenza-associated respiratory mortality: a modelling study. *Lancet*, 391(10127):1285–1300, March 2018.

[72] Xiaohui Ju, William W Hannon, Tomasz Kaszuba, Caelan E Radford, Brendan B Larsen, Samantha S Nelson, Christopher A Nelson, Israel Baltazar-Perez, Ofer Zimmerman, Daved H Fremont, Michael S Diamond, and Jesse D Bloom. Determinants of human versus mosquito cell entry by the chikungunya virus envelope proteins. *bioRxivorg*, page 2025.08.25.672233, August 2025.

[73] Umut Karakus, Ignacio Mena, Jithesh Kottur, Sara S El Zahed, Rocío Seoane, Soner Yildiz, Leanne Chen, Magdalena Plancarte, Leann Lindsay, Rebecca Halpin, Timothy B Stockwell, David E Wentworth, Geert-Jan Boons, Florian Krammer, Silke Stertz, Walter Boyce, Robert P de Vries, Aneel K Aggarwal, and Adolfo García-Sastre. H19 influenza a virus exhibits species-specific MHC class II receptor usage. *Cell Host Microbe*, 32(7):1089–1102.e10, July 2024.

[74] Umut Karakus, Milagros Sempere Borau, Patricia Martínez-Barragán, Josephine von Kempis, Soner Yildiz, Laura M Arroyo-Fernández, Marie O Pohl, Julia A Steiger, Irina Glas, Annika Hunziker, Adolfo García-Sastre, and Silke Stertz. MHC class II proteins mediate sialic acid independent entry of human and avian H2N2 influenza a viruses. *Nat. Microbiol.*, 9(10):2626–2641, October 2024.

[75] Umut Karakus, Thiprampai Thamamongood, Kevin Ciminski, Wei Ran, Sira C Günther, Marie O Pohl, Davide Eletto, Csaba Jeney, Donata Hoffmann, Sven Reiche, Jan Schinköthe, Reiner Ulrich, Julius Wiener, Michael G B Hayes, Max W Chang, Annika Hunziker, Emilio Yángüez, Teresa Aydillo, Florian Krammer, Josua Oderbolz, Matthias Meier, Annette Oxenius, Anne Halenius, Gert Zimmer, Christopher Benner, Benjamin G Hale, Adolfo García-Sastre, Martin Beer, Martin Schwemmle, and Silke Stertz. MHC class II proteins mediate cross-species entry of bat influenza viruses. *Nature*, 567(7746):109–112, March 2019.

[76] G W Kemble, D L Bodian, J Rosé, I A Wilson, and J M White. Intermonomer disulfide bonds impair the fusion activity of influenza virus hemagglutinin. *J. Virol.*, 66(8):4940–4950, August 1992.

[77] Caroline Kikawa, John Huddleston, Andrea N Loes, Sam A Turner, Jover Lee, Ian G Barr, Benjamin J Cowling, Janet A Englund, Alexander L Greninger, Ruth Harvey, Hideki Hasegawa, Faith Ho, Kirsten Lacombe, Nancy H L Leung, Nicola S Lewis, Heidi Peck, Shinji Watanabe, Derek J Smith, Trevor Bedford, and Jesse D Bloom. Near real-time data on the human neutralizing antibody landscape to influenza virus to inform vaccine-strain selection in september 2025. *bioRxivorg*, page 2025.09.06.674661, September 2025.

[78] Caroline Kikawa, Andrea N Loes, John Huddleston, Marlin D Figgins, Philippa Steinberg, Tachianna Griffiths, Elizabeth M Drapeau, Heidi Peck, Ian G Barr, Janet A Englund, Scott E Hens-

ley, Trevor Bedford, and Jesse D Bloom. High-throughput neutralization measurements correlate strongly with evolutionary success of human influenza strains. *bioRxiv*, page 2025.03.04.641544, March 2025.

[79] Justin B Kinney, Anand Murugan, Curtis G Callan, Jr, and Edward C Cox. Using deep sequencing to characterize the biophysical mechanism of a transcriptional regulatory sequence. *Proc. Natl. Acad. Sci. U. S. A.*, 107(20):9158–9163, May 2010.

[80] Grant Kinsler, Yuping Li, Gavin Sherlock, and Dmitri A Petrov. A high-resolution two-step evolution experiment in yeast reveals a shift from pleiotropic to modular adaptation. *PLoS Biol.*, 22(12):e3002848, December 2024.

[81] Kathryn E Kistler and Trevor Bedford. An atlas of continuous adaptive evolution in endemic human viruses. *Cell Host Microbe*, 31(11):1898–1909.e3, November 2023.

[82] Björn F Koel, David F Burke, Theo M Bestebroer, Stefan van der Vliet, Gerben C M Zondag, Gaby Vervaet, Eugene Skepner, Nicola S Lewis, Monique I J Spronken, Colin A Russell, Mikhail Y Eropkin, Aeron C Hurt, Ian G Barr, Jan C de Jong, Guus F Rimmelzwaan, Albert D M E Osterhaus, Ron A M Fouchier, and Derek J Smith. Substitutions near the receptor binding site determine major antigenic change during influenza virus evolution. *Science*, 342(6161):976–979, November 2013.

[83] Huihui Kong, Shufang Fan, Kosuke Takada, Masaki Imai, Gabriele Neumann, and Yoshihiro Kawaoka. H3N2 influenza viruses with 12- or 16-amino acid deletions in the receptor-binding region of their hemagglutinin protein. *MBio*, 12(6):e0151221, December 2021.

[84] Florian Krammer. The human antibody response to influenza a virus infection and vaccination. *Nat. Rev. Immunol.*, 19(6):383–397, June 2019.

[85] A Kuzmina, Y Khalaila, O Voloshin, A Keren-Naus, L Boehm-Cohen, Y Raviv, and Taube. SARS-CoV-2 spike variants exhibit differential infectivity and neutralization resistance to convalescent or post-vaccination sera. *Cell host & microbe*, 29(4):522–528, 2021.

[86] Brendan B Larsen, Teagan McMahon, Jack T Brown, Zhaoqian Wang, Caelan E Radford, James E Crowe, Jr, David Veesler, and Jesse D Bloom. Functional and antigenic landscape of the nipah virus receptor-binding protein. *Cell*, 188(9):2480–2494.e22, May 2025.

[87] W G Laver, G M Air, R G Webster, W Gerhard, C W Ward, and T A Dopheide. Antigenic drift in type a influenza virus: sequence differences in the hemagglutinin of hong kong (H3N2) variants selected with monoclonal hybridoma antibodies. *Virology*, 98(1):226–237, October 1979.

[88] Chung-Young Lee, Vedhika Raghunathan, C Joaquin Caceres, Ginger Geiger, Brittany Seibert, Flavio Cargnin Faccin, L Claire Gay, Lucas M Ferreri, Drishti Kaul, Jens Wrammert, Gene S Tan, Daniel R Perez, and Anice C Lowen. Epistasis reduces fitness costs of influenza a virus escape from stem-binding antibodies. *Proc. Natl. Acad. Sci. U. S. A.*, 120(17):e2208718120, April 2023.

[89] Jiwon Lee, Daniel R Boutz, Veronika Chromikova, M Gordon Joyce, Christopher Vollmers, Kwanyee Leung, Andrew P Horton, Brandon J DeKosky, Chang-Han Lee, Jason J Lavinder, Ellen M Murrin, Constantine Chrysostomou, Kam Hon Hoi, Yaroslav Tsybovsky, Paul V Thomas, Aliaksandr Druz, Baoshan Zhang, Yi Zhang, Lingshu Wang, Wing-Pui Kong, Daechan Park, Lyubov I Popova, Cornelia L Dekker, Mark M Davis, Chalise E Carter, Ted M Ross, Andrew D Ellington, Patrick C Wilson, Edward M Marcotte, John R Mascola, Gregory C Ippolito, Florian Krammer, Stephen R Quake, Peter D Kwong, and George Georgiou. Molecular-level analysis of the serum antibody repertoire in young adults before and after seasonal influenza vaccination. *Nat. Med.*, 22(12):1456–1464, December 2016.

[90] Juhye M Lee, Rachel Eguia, Seth J Zost, Saket Choudhary, Patrick C Wilson, Trevor Bedford, Terry Stevens-Ayers, Michael Boeckh, Aeron C Hurt, Seema S Lakdawala, Scott E Hensley, and Jesse D Bloom. Mapping person-to-person variation in viral mutations that escape polyclonal serum targeting influenza hemagglutinin. *Elife*, 8, August 2019.

[91] Juhye M Lee, John Huddleston, Michael B Doud, Kathryn A Hooper, Nicholas C Wu, Trevor Bedford, and Jesse D Bloom. Deep mutational scanning of hemagglutinin helps predict evolutionary fates of human H3N2 influenza variants. *Proc. Natl. Acad. Sci. U. S. A.*, 115(35):E8276–E8285, August 2018.

[92] Peter S Lee, Nobuko Ohshima, Robyn L Stanfield, Wenli Yu, Yoshitaka Iba, Yoshinobu Okuno, Yoshikazu Kurosawa, and Ian A Wilson. Receptor mimicry by antibody F045-092 facilitates universal binding to the H3 subtype of influenza virus. *Nat. Commun.*, 5(1):3614, April 2014.

[93] Ruipeng Lei, Weiwen Liang, Wenhao O Ouyang, Andrea Hernandez Garcia, Chika Kikuchi, Shengyang Wang, Ryan McBride, Timothy J C Tan, Yuanxin Sun, Chunke Chen, Claire S Graham, Lucia A Rodriguez, Ivana R Shen, Danbi Choi, Roberto Bruzzone, James C Paulson, Satish K Nair, Chris K P Mok, and Nicholas C Wu. Epistasis mediates the evolution of the receptor binding mode in recent human H3N2 hemagglutinin. *Nat. Commun.*, 15(1):5175, June 2024.

[94] Justin Lessler, Steven Riley, Jonathan M Read, Shuying Wang, Huachen Zhu, Gavin J D Smith, Yi Guan, Chao Qiang Jiang, and Derek A T Cummings. Evidence for antigenic seniority in influenza a (H_3N_2) antibody responses in southern china. *PLoS Pathog.*, 8(7):e1002802, July 2012.

[95] Yang Li, David L Bostick, Colleen B Sullivan, Jaclyn L Myers, Sara B Griesemer, Kirsten Stgeorge, Joshua B Plotkin, and Scott E Hensley. Single hemagglutinin mutations that alter both antigenicity and receptor binding avidity influence influenza virus antigenic clustering. *J. Virol.*, 87(17):9904–9910, September 2013.

[96] Yang Li, Jaclyn L Myers, David L Bostick, Colleen B Sullivan, Jonathan Madara, Susanne L Linderman, Qin Liu, Donald M Carter, Jens Wrammert, Susanna Esposito, Nicola Principi, Joshua B Plotkin, Ted M Ross, Rafi Ahmed, Patrick C Wilson, and Scott E Hensley. Immune history shapes specificity of pandemic H_1N_1 influenza antibody responses. *J. Exp. Med.*, 210(8):1493–1500, July 2013.

[97] Ruonan Liang, Francesca Peccati, Niels L D Ponse, Elif Uslu, Geert-Jan Boons, Luca Unione, and Robert P de Vries. Epistasis in the receptor binding domain of contemporary H_3N_2 viruses that reverted to bind sialylated diLacNAc repeats. *bioRxiv*, (biorxiv;2024.11.26.625384v1), November 2024.

[98] Ting-Hui Lin, Xueyong Zhu, Shengyang Wang, Ding Zhang, Ryan McBride, Wenli Yu, Simeon Babarinde, James C Paulson, and Ian A Wilson. A single mutation in bovine influenza H_5N_1 hemagglutinin switches specificity to human receptors. *Science*, 386(6726):1128–1134, December 2024.

[99] Susanne L Linderman, Benjamin S Chambers, Seth J Zost, Kaela Parkhouse, Yang Li, Christin Herrmann, Ali H Ellebedy, Donald M Carter, Sarah F Andrews, Nai-Ying Zheng, Min Huang, Yunping Huang, Donna Strauss, Beth H Shaz, Richard L Hodinka, Gustavo Reyes-Terán, Ted M Ross, Patrick C Wilson, Rafi Ahmed, Jesse D Bloom, and Scott E Hensley. Potential antigenic explanation for atypical H_1N_1 infections among middle-aged adults during the 2013-2014 influenza season. *Proc. Natl. Acad. Sci. U. S. A.*, 111(44):15798–15803, November 2014.

[100] Martin Linster, Sander van Boheemen, Miranda de Graaf, Eefje J A Schrauwen, Pascal Lexmond, Benjamin Mänz, Theo M Bestebroer, Jan Baumann, Debby van Riel, Guus F Rimmelzwaan, Albert D M E Osterhaus, Mikhail Matrosovich, Ron A M Fouchier, and Sander Herfst. Identification, characterization, and natural selection of mutations driving airborne transmission of a/H_5N_1 virus. *Cell*, 157(2):329–339, April 2014.

[101] Andrea N Loes, Rosario Araceli L Tarabi, John Huddleston, Lisa Touyon, Sook San Wong, Samuel M S Cheng, Nancy H L Leung, William W Hannon, Trevor Bedford, Sarah Cobey, Benjamin J Cowling, and Jesse D Bloom. High-throughput sequencing-based neutralization assay reveals how repeated vaccinations impact titers to recent human H1N1 influenza strains. *J. Virol.*, 98(10):e00068924, October 2024.

[102] Mark Lunzer, Stephen P Miller, Roderick Felsheim, and Antony M Dean. The biochemical architecture of an ancient adaptive landscape. *Science*, 310(5747):499–501, October 2005.

[103] Daniel M Lyons and Adam S Lauring. Mutation and epistasis in influenza virus evolution. *Viruses*, 10(8):407, August 2018.

[104] Caroline M Mair, Kai Ludwig, Andreas Herrmann, and Christian Sieben. Receptor binding and pH stability - how influenza a virus hemagglutinin affects host-specific virus infection. *Biochim. Biophys. Acta*, 1838(4):1153–1168, April 2014.

[105] M Matrosovich, A Tuzikov, N Bovin, A Gambaryan, A Klimov, M R Castrucci, I Donatelli, and Y Kawaoka. Early alterations of the receptor-binding properties of H1, H2, and H3 avian influenza virus hemagglutinins after their introduction into mammals. *J. Virol.*, 74(18):8502–8512, September 2000.

[106] Mikhail Matrosovich, Tatyana Matrosovich, Jackie Carr, Noel A Roberts, and Hans-Dieter Klenk. Overexpression of the alpha-2,6-sialyltransferase in MDCK cells increases influenza virus sensitivity to neuraminidase inhibitors. *J. Virol.*, 77(15):8418–8425, August 2003.

[107] Mikhail N Matrosovich, Tatyana Y Matrosovich, Thomas Gray, Noel A Roberts, and Hans-Dieter Klenk. Human and avian influenza viruses target different cell types in cultures of human airway epithelium. *Proc. Natl. Acad. Sci. U. S. A.*, 101(13):4620–4624, March 2004.

[108] Elaine C Meng, Thomas D Goddard, Eric F Pettersen, Greg S Couch, Zach J Pearson, John H Morris, and Thomas E Ferrin. UCSF ChimeraX: Tools for structure building and analysis. *Protein Sci.*, 32(11):e4792, November 2023.

[109] Dylan H Morris, Katelyn M Gostic, Simone Pompei, Trevor Bedford, Marta Łuksza, Richard A Neher, Bryan T Grenfell, Michael Lässig, and John W McCauley. Predictive modeling of influenza shows the promise of applied evolutionary biology. *Trends Microbiol.*, 26(2):102–118, February 2018.

[110] Anneliese J Morrison, Daria R Wonderlick, and Michael J Harms. Ensemble epistasis: thermodynamic origins of nonadditivity between mutations. *Genetics*, 219(1), August 2021.

[111] V M Mosley and R W G Wyckoff. Electron micrography of the virus of influenza. *Nature*, 157(3983):263, March 1946.

[112] Alief Moulana, T Dupic, Angela M Phillips, Jeffrey Chang, Serafina Nieves, Anne A Roffler, Allison J Greaney, Tyler N Starr, J Bloom, and Michael M Desai. Compensatory epistasis maintains ACE2 affinity in SARS-CoV-2 omicron BA.1. *Nature Communications*, 13:7011, June 2022.

[113] Alief Moulana, T Dupic, Angela M Phillips, Jeffrey Chang, Anne A Roffler, Allison J Greaney, Tyler N Starr, Jesse D Bloom, and Michael M Desai. The landscape of antibody binding affinity in SARS-CoV-2 omicron BA.1 evolution. *eLife*, 12:e83442, September 2022.

[114] Jaclyn L Myers, Katherine S Wetzel, Susanne L Linderman, Yang Li, Colleen B Sullivan, and Scott E Hensley. Compensatory hemagglutinin mutations alter antigenic properties of influenza viruses. *J. Virol.*, 87(20):11168–11172, October 2013.

[115] Katsuhisa Nakajima, Eri Nobusawa, Alexander Nagy, and Setsuko Nakajima. Accumulation of amino acid substitutions promotes irreversible structural changes in the hemagglutinin of human influenza AH3 virus during evolution. *J. Virol.*, 79(10):6472–6477, May 2005.

[116] Richard A Neher, Trevor Bedford, Rodney S Daniels, Colin A Russell, and Boris I Shraiman. Prediction, dynamics, and visualization of antigenic phenotypes of seasonal influenza viruses. *Proc. Natl. Acad. Sci. U. S. A.*, 113(12):E1701–9, March 2016.

[117] Gabriele Neumann and Yoshihiro Kawaoka. Transmission of influenza a viruses. *Virology*, 479-480:234–246, May 2015.

[118] Lam-Tung Nguyen, Heiko A Schmidt, Arndt von Haeseler, and Bui Quang Minh. IQ-TREE: a fast and effective stochastic algorithm for estimating maximum-likelihood phylogenies. *Mol. Biol. Evol.*, 32(1):268–274, January 2015.

[119] H A Orr. Adaptation and the cost of complexity. *Evolution*, 54(1):13–20, February 2000.

[120] Jakub Otwinowski. Biophysical inference of epistasis and the effects of mutations on protein stability and function. *Mol. Biol. Evol.*, 35(10):2345–2354, October 2018.

[121] Jakub Otwinowski, David M McCandlish, and Joshua B Plotkin. Inferring the shape of global epistasis. *Proc. Natl. Acad. Sci. U. S. A.*, 115(32):E7550–E7558, August 2018.

[122] Yeonwoo Park, Brian P H Metzger, and Joseph W Thornton. The simplicity of protein sequence-function relationships. *Nat. Commun.*, 15(1):7953, September 2024.

[123] Colin R Parrish, Pablo R Murcia, and Edward C Holmes. Influenza virus reservoirs and intermediate hosts: dogs, horses, and new possibilities for influenza virus exposure of humans. *J. Virol.*, 89(6):2990–2994, March 2015.

[124] Lisa M Parsons, Yanming An, Robert P de Vries, Cornelis A M de Haan, and John F Cipollo. Glycosylation characterization of an influenza H5N7 hemagglutinin series with engineered glycosylation patterns: Implications for structure-function relationships. *J. Proteome Res.*, 16(2):398–412, February 2017.

[125] Velislava N Petrova and Colin A Russell. The evolution of seasonal influenza viruses. *Nat. Rev. Microbiol.*, 16(1):47–60, January 2018.

[126] Angela M Phillips, Katherine R Lawrence, Alief Moulana, T Dupic, Jeffrey H Chang, Milo S Johnson, I Cvijović, T Mora, A Walczak, and Michael M Desai. Binding affinity landscapes constrain the evolution of broadly neutralizing anti-influenza antibodies. *eLife*, 10:e71393, May 2021.

[127] Angela M Phillips, Daniel P Maurer, Caelan Brooks, T Dupic, A Schmidt, and Michael M Desai. Hierarchical sequence-affinity landscapes shape the evolution of breadth in an anti-influenza receptor binding site antibody. *eLife*, 12:e83628, September 2022.

[128] L Piccoli, Y J Park, M A Tortorici, N Czudnochowski, A C Walls, M Beltramello, and Veesler. Mapping neutralizing and immunodominant sites on the SARS-CoV-2 spike receptor-binding domain by structure-guided high-resolution serology. *Cell*, 183(4):1024–1042, 2020.

[129] Frank J Poelwijk, Michael Socolich, and Rama Ranganathan. Learning the pattern of epistasis linking genotype and phenotype in a protein. *Nat. Commun.*, 10(1):4213, September 2019.

[130] David D Pollock, Grant Thiltgen, and Richard A Goldstein. Amino acid coevolution induces an evolutionary stokes shift. *Proc. Natl. Acad. Sci. U. S. A.*, 109(21):E1352–9, May 2012.

[131] Lyubov Popova, Kenneth Smith, Ann H West, Patrick C Wilson, Judith A James, Linda F Thompson, and Gillian M Air. Immunodominance of antigenic site B over site a of hemagglutinin of recent H3N2 influenza viruses. *PLoS One*, 7(7):e41895, July 2012.

[132] P Sivaramakrishna Rachakonda, Michael Veit, Thomas Korte, Kai Ludwig, Christoph Böttcher, Qiang Huang, Michael F G Schmidt, and Andreas Herrmann. The relevance of salt bridges for the stability of the influenza virus hemagglutinin. *FASEB J.*, 21(4):995–1002, April 2007.

[133] Caelan E Radford, Philipp Schommers, Lutz Gieselmann, Katharine H D Crawford, Bernadeta Dadonaite, Timothy C Yu, Adam S Dingens, Julie Overbaugh, Florian Klein, and Jesse D Bloom. Mapping the neutralizing specificity of human anti-HIV serum by deep mutational scanning. *Cell Host Microbe*, 31(7):1200–1215.e9, July 2023.

[134] Andrew Rambaut, Edward C Holmes, Áine O'Toole, Verity Hill, John T McCrone, Christopher Ruis, Louis du Plessis, and Oliver G Pybus. A dynamic nomenclature proposal for SARS-CoV-2 lineages to assist genomic epidemiology. *Nat. Microbiol.*, 5(11):1403–1407, November 2020.

[135] Sylvia Ranjeva, Rahul Subramanian, Vicky J Fang, Gabriel M Leung, Dennis K M Ip, Ranawaka A P M Perera, J S Malik Peiris, Benjamin J Cowling, and Sarah Cobey. Age-specific differences in the dynamics of protective immunity to influenza. *Nat. Commun.*, 10(1):1660, April 2019.

[136] Marion Russier, Guohua Yang, Jerold E Rehg, Sook-San Wong, Heba H Mostafa, Thomas P Fabrizio, Subrata Barman, Scott Krauss, Robert G Webster, Richard J Webby, and Charles J Russell. Molecular requirements for a pandemic influenza virus: An acid-stable hemagglutinin protein. *Proc. Natl. Acad. Sci. U. S. A.*, 113(6):1636–1641, February 2016.

[137] Zachary R Sailer and Michael J Harms. Detecting high-order epistasis in nonlinear genotype-phenotype maps. *Genetics*, 205(3):1079–1088, March 2017.

[138] Zachary R Sailer and Michael J Harms. High-order epistasis shapes evolutionary trajectories. *PLoS Comput. Biol.*, 13(5):e1005541, May 2017.

[139] Jake Scott, Michael S Abers, Harleen K Marwah, Nicole C McCann, Eric A Meyerowitz, Aaron Richterman, Derek F Fleming, Elise J Holmes, Leah E Moat, Sydney G Redepenning, Emily A Smith, Clare J Stoddart, Maria E Sundaram, Angela K Ulrich, Christopher Alba, Cory J Anderson, Meredith K Arpey, Ethan Borre, Joseph Ladines-Lim, Angela J Mehr, Katherine Rich, Corey Watts, Nicole E Basta, Jana Jarolimova, Rochelle P Walensky, and Caitlin M Dugdale. Updated evidence for covid-19, RSV, and influenza vaccines for 2025-2026. *N. Engl. J. Med.*, (NEJMsa2514268), October 2025.

[140] Premal Shah, David M McCandlish, and Joshua B Plotkin. Contingency and entrenchment in protein evolution under purifying selection. *Proc. Natl. Acad. Sci. U. S. A.*, 112(25):E3226–35, June 2015.

[141] Jianzhong Shi, Xianying Zeng, Pengfei Cui, Cheng Yan, and Hualan Chen. Alarming situation of emerging H5 and H7 avian influenza and effective control strategies. *Emerg. Microbes Infect.*, 12(1):2155072, December 2023.

[142] Yi Shi, Ying Wu, Wei Zhang, Jianxun Qi, and George F Gao. Enabling the 'host jump': structural determinants of receptor-binding specificity in influenza a viruses. *Nat. Rev. Microbiol.*, 12(12):822–831, December 2014.

[143] Arthur Chun-Chieh Shih, Tzu-Chang Hsiao, Mei-Shang Ho, and Wen-Hsiung Li. Simultaneous amino acid substitutions at antigenic sites drive influenza a hemagglutinin evolution. *Proc. Natl. Acad. Sci. U. S. A.*, 104(15):6283–6288, April 2007.

[144] David A Shore, Hua Yang, Amanda L Balish, Samuel S Shepard, Paul J Carney, Jessie C Chang, Charles T Davis, Ruben O Donis, Julie M Villanueva, Alexander I Klimov, and James Stevens. Structural and antigenic variation among diverse clade 2 H5N1 viruses. *PLoS One*, 8(9):e75209, September 2013.

[145] Kirsty R Short, Mathilde Richard, Josanne H Verhagen, Debby van Riel, Eefje J A Schrauwen, Judith M A van den Brand, Benjamin Mänz, Rogier Bodewes, and Sander Herfst. One health, multiple challenges: The inter-species transmission of influenza a virus. *One Health*, 1:1–13, December 2015.

[146] J J Skehel, D J Stevens, R S Daniels, A R Douglas, M Knossow, I A Wilson, and D C Wiley. A carbohydrate side chain on hemagglutinins of hong kong influenza viruses inhibits recognition by a monoclonal antibody. *Proc. Natl. Acad. Sci. U. S. A.*, 81(6):1779–1783, March 1984.

[147] J J Skehel and D C Wiley. Receptor binding and membrane fusion in virus entry: the influenza hemagglutinin. *Annu. Rev. Biochem.*, 69(1):531–569, 2000.

[148] Derek J Smith, Alan S Lapedes, Jan C de Jong, Theo M Bestebroer, Guus F Rimmelzwaan, Albert D M E Osterhaus, and Ron A M Fouchier. Mapping the antigenic and genetic evolution of influenza virus. *Science*, 305(5682):371–376, July 2004.

[149] Tyler N Starr, Nadine Czudnochowski, Zhuoming Liu, Fabrizia Zatta, Young-Jun Park, Amin Addetia, Dora Pinto, Martina Beltramello, Patrick Hernandez, Allison J Greaney, Roberta Marzi, William G Glass, Ivy Zhang, Adam S Dingens, John E Bowen, M Alejandra Tortorici, Alexandra C Walls, Jason A Wojcechowskyj, Anna De Marco, Laura E Rosen, Jiayi Zhou, Martin Montiel-Ruiz, Hannah Kaiser, Josh R Dillen, Heather Tucker, Jessica Bassi, Chiara Silacci-Fregni, Michael P Housley, Julia di Iulio, Gloria Lombardo, Maria Agostini, Nicole Sprugasci, Katja Culap, Stefano Jaconi, Marcel Meury, Exequiel Dellota, Jr, Rana Abdelnabi, Shi-Yan Caroline Foo, Elisabetta Cameroni, Spencer Stumpf, Tristan I Croll, Jay C Nix, Colin Havenar-Daughton, Luca Piccoli, Fabio Benigni, Johan Neyts, Amalio Telenti, Florian A Lempp, Matteo S Pizzuto, John D Chodera,

Christy M Hebner, Herbert W Virgin, Sean P J Whelan, David Veesler, Davide Corti, Jesse D Bloom, and Gyorgy Snell. SARS-CoV-2 RBD antibodies that maximize breadth and resistance to escape. *Nature*, 597(7874):97–102, September 2021.

[150] Tyler N Starr, Allison J Greaney, Amin Addetia, William W Hannon, Manish C Choudhary, Adam S Dingens, Jonathan Z Li, and Jesse D Bloom. Prospective mapping of viral mutations that escape antibodies used to treat COVID-19. *Science*, 371(6531):850–854, February 2021.

[151] Tyler N Starr, Allison J Greaney, Adam S Dingens, and Jesse D Bloom. Complete map of SARS-CoV-2 RBD mutations that escape the monoclonal antibody LY-CoV555 and its cocktail with LY-CoV016. *Cell Rep. Med.*, 2(4):100255, April 2021.

[152] Tyler N Starr, Allison J Greaney, William W Hannon, Andrea N Loes, Kevin Hauser, Josh R Dillen, Elena Ferri, Ariana Ghez Farrell, Bernadeta Dadonaite, Matthew McCallum, Kenneth A Matreyek, Davide Corti, David Veesler, Gyorgy Snell, and Jesse D Bloom. Shifting mutational constraints in the SARS-CoV-2 receptor-binding domain during viral evolution. *Science*, 377(6604):420–424, July 2022.

[153] Tyler N Starr, Allison J Greaney, Sarah K Hilton, Daniel Ellis, Katharine H D Crawford, Adam S Dingens, Mary Jane Navarro, John E Bowen, M Alejandra Tortorici, Alexandra C Walls, Neil P King, David Veesler, and Jesse D Bloom. Deep mutational scanning of SARS-CoV-2 receptor binding domain reveals constraints on folding and ACE2 binding. *Cell*, 182(5):1295–1310.e20, September 2020.

[154] Tyler N Starr and Joseph W Thornton. Epistasis in protein evolution: Epistasis in protein evolution. *Protein Sci.*, 25(7):1204–1218, July 2016.

[155] Frank W Stearns. One hundred years of pleiotropy: a retrospective. *Genetics*, 186(3):767–773, November 2010.

[156] H Sun, J Yang, T Zhang, L P Long, K Jia, G Yang, and others. Using sequence data to infer the antigenicity of influenza virus. mBio 4: e00230-13. 2013.

[157] J M Taft, C R Weber, B Gao, R A Ehling, J Han, L Frei, and Reddy S. Deep mutational learning predicts ACE2 binding and antibody escape to combinatorial mutations in the SARS-CoV-2 receptor-binding domain. *Cell*, 185(21):4008–4022, 2022.

[158] Ammar Tareen, Mahdi Kooshkbaghi, Anna Posfai, William T Ireland, David M McCandlish, and Justin B Kinney. MAVE-NN: learning genotype-phenotype maps from multiplex assays of variant effect. *Genome Biol.*, 23(1):98, April 2022.

[159] Nicole N Thadani, Sarah Gurev, Pascal Notin, Noor Youssef, Nathan J Rollins, Daniel Ritter, Chris Sander, Yarin Gal, and Debora S Marks. Learning from prepandemic data to forecast viral escape. *Nature*, 622(7984):818–825, October 2023.

[160] Kannan Tharakaraman, Akila Jayaraman, Rahul Raman, Karthik Viswanathan, Nathan W Stebbins, David Johnson, Zachary Shriver, V Sasisekharan, and Ram Sasisekharan. Glycan receptor binding of the influenza a virus H7N9 hemagglutinin. *Cell*, 153(7):1486–1493, June 2013.

[161] Andrew J Thompson, Nicholas C Wu, Angeles Canales, Chika Kikuchi, Xueyong Zhu, Beatriz Fernández de Toro, Francisco J Cañada, Charli Worth, Shengyang Wang, Ryan McBride, Wenjie Peng, Corwin M Nycholat, Jesús Jiménez-Barbero, Ian A Wilson, and James C Paulson. Evolution of human H3N2 influenza virus receptor specificity has substantially expanded the receptor-binding domain site. *Cell Host Microbe*, 32(2):261–275.e4, February 2024.

[162] Bargavi Thyagarajan and Jesse D Bloom. The inherent mutational tolerance and antigenic evolvability of influenza hemagglutinin. *Elife*, 3, July 2014.

[163] Ilona I Tosheva, Kain S Saygan, Suzanne Ma Mijnhardt, Charles J Russell, Pieter L A Fraaij, and Sander Herfst. Hemagglutinin stability as a key determinant of influenza a virus transmission via air. *Curr. Opin. Virol.*, 61(101335):101335, August 2023.

[164] Hannah L Turner, Jesper Pallesen, Shanshan Lang, Sandhya Bangaru, Sarah Urata, Sheng Li, Christopher A Cottrell, Charles A Bowman, James E Crowe, Jr, Ian A Wilson, and Andrew B Ward. Potent anti-influenza H7 human monoclonal antibody induces separation of hemagglutinin receptor-binding head domains. *PLoS Biol.*, 17(2):e3000139, February 2019.

[165] Timothy M Uyeki, David S Hui, Maria Zambon, David E Wentworth, and Arnold S Monto. Influenza. *Lancet*, 400(10353):693–706, August 2022.

[166] Raquel Viana, Sikhulile Moyo, Daniel G Amoako, Houriiyah Tegally, Cathrine Scheepers, Christian L Althaus, Ugochukwu J Anyaneji, Phillip A Bester, Maciej F Boni, Mohammed Chand, Wonderful T Choga, Rachel Colquhoun, Michaela Davids, Koen Deforche, Deelan Doolabh, Louis du Plessis, Susan Engelbrecht, Josie Everatt, Jennifer Giandhari, Marta Giovanetti, Diana Hardie, Verity Hill, Nei-Yuan Hsiao, Arash Iranzadeh, Arshad Ismail, Charity Joseph, Rageema

Joseph, Legodile Koopile, Sergei L Kosakovsky Pond, Moritz U G Kraemer, Lesego Kuate-Lere, Oluwakemi Laguda-Akingba, Onalethatha Lesetedi-Mafoko, Richard J Lessells, Shahin Lockman, Alexander G Lucaci, Arisha Maharaj, Boitshoko Mahlangu, Tongai Maponga, Kamela Mahlakwane, Zinhle Makatini, Gert Marais, Dorcas Maruapula, Kereng Masupu, Mogomotsi Matshaba, Simnikiwe Mayaphi, Nokuzola Mbhele, Mpaphi B Mbulawa, Adriano Mendes, Koleka Mlisana, Anele Mnguni, Thabo Mohale, Monika Moir, Kgomotso Moruisi, Mosepele Mosepele, Gerald Motsatsi, Modisa S Motswaledi, Thongbotho Mphoyakgosi, Nokukhanya Msomi, Peter N Mwangi, Yeshnee Naidoo, Noxolo Ntuli, Martin Nyaga, Lucier Olubayo, Sureshnee Pillay, Botshelo Radibe, Yajna Ramphal, Upasana Ramphal, James E San, Lesley Scott, Roger Shapiro, Lavanya Singh, Pamela Smith-Lawrence, Wendy Stevens, Amy Strydom, Kathleen Subramoney, Naume Tebeila, Derek Tshiabuila, Joseph Tsui, Stephanie van Wyk, Steven Weaver, Constantinos K Wibmer, Eduan Wilkinson, Nicole Wolter, Alexander E Zarebski, Boitumelo Zuze, Dominique Goedhals, Wolfgang Preiser, Florette Treurnicht, Marietje Venter, Carolyn Williamson, Oliver G Pybus, Jinal Bhiman, Allison Glass, Darren P Martin, Andrew Rambaut, Simani Gaseitsiwe, Anne von Gottberg, and Tulio de Oliveira. Rapid epidemic expansion of the SARS-CoV-2 omicron variant in southern africa. *Nature*, 603(7902):679–686, March 2022.

[167] Günter P Wagner, Jane P Kenney-Hunt, Mihaela Pavlicev, Joel R Peck, David Waxman, and James M Cheverud. Pleiotropic scaling of gene effects and the 'cost of complexity'. *Nature*, 452(7186):470–472, March 2008.

[168] Günter P Wagner and Jianzhi Zhang. The pleiotropic structure of the genotype-phenotype map: the evolvability of complex organisms. *Nat. Rev. Genet.*, 12(3):204–213, March 2011.

[169] Shira Warszawski, Ravit Netzer, Dan S Tawfik, and Sarel J Fleishman. A "fuzzy"-logic language for encoding multiple physical traits in biomolecules. *J. Mol. Biol.*, 426(24):4125–4138, December 2014.

[170] Akiko Watanabe, Kevin R McCarthy, Masayuki Kuraoka, Aaron G Schmidt, Yu Adachi, Taishi Onodera, Keisuke Tonouchi, Timothy M Caradonna, Goran Bajic, Shengli Song, Charles E McGee, Gregory D Sempowski, Feng Feng, Patricia Urick, Thomas B Kepler, Yoshimasa Takahashi, Stephen C Harrison, and Garnett Kelsoe. Antibodies to a conserved influenza head interface epitope protect by an IgG subtype-dependent mechanism. *Cell*, 177(5):1124–1135.e16, May 2019.

[171] R G Webster and W G Laver. Determination of the number of nonoverlapping antigenic areas on hong kong (H_3N_2) influenza virus hemagglutinin with monoclonal antibodies and the selection of variants with potential epidemiological significance. *Virology*, 104(1):139–148, 1980.

[172] Daniel M Weinreich, Nigel F Delaney, Mark A Depristo, and Daniel L Hartl. Darwinian evolution can follow only very few mutational paths to fitter proteins. *Science*, 312(5770):111–114, April 2006.

[173] J A Wells. Additivity of mutational effects in proteins. *Biochemistry*, 29(37):8509–8517, September 1990.

[174] Frances C Welsh, Rachel T Eguia, Juhye M Lee, Hugh K Haddox, Jared Galloway, Nguyen Van Vinh Chau, Andrea N Loes, John Huddleston, Timothy C Yu, Mai Quynh Le, Nguyen T D Nhat, Nguyen Thi Le Thanh, Alexander L Greninger, Helen Y Chu, Janet A Englund, Trevor Bedford, Frederick A Matsen, 4th, Maciej F Boni, and Jesse D Bloom. Age-dependent heterogeneity in the antigenic effects of mutations to influenza hemagglutinin. *Cell Host Microbe*, 32(8):1397–1411.e11, August 2024.

[175] Kim B Westgeest, Miranda de Graaf, Mathieu Fourment, Theo M Bestebroer, Ruud van Beek, Monique I J Spronken, Jan C de Jong, Guus F Rimmelzwaan, Colin A Russell, Albert D M E Osterhaus, Gavin J D Smith, Derek J Smith, and Ron A M Fouchier. Genetic evolution of the neuraminidase of influenza a (H3N2) viruses from 1968 to 2009 and its correspondence to haemagglutinin evolution. *J. Gen. Virol.*, 93(Pt 9):1996–2007, September 2012.

[176] D C Wiley, I A Wilson, and J J Skehel. Structural identification of the antibody-binding sites of hong kong influenza haemagglutinin and their involvement in antigenic variation. *Nature*, 289(5796):373–378, January 1981.

[177] Michael Worobey, Guan-Zhu Han, and Andrew Rambaut. Genesis and pathogenesis of the 1918 pandemic H1N1 influenza a virus. *Proc. Natl. Acad. Sci. U. S. A.*, 111(22):8107–8112, June 2014.

[178] Sewall Wright. The roles of mutation, inbreeding, crossbreeding and selection in evolution. *Proceedings of the XI International Congress of Genetics*, 8:209–222, 1932.

[179] Nicholas C Wu, Jakub Otwinowski, Andrew J Thompson, Corwin M Nycholat, Armita Nourmohammad, and Ian A Wilson. Major antigenic site B of human influenza H3N2 viruses has an evolving local fitness landscape. *Nat. Commun.*, 11(1):1233, March 2020.

[180] Nicholas C Wu, Andrew J Thompson, Juhye M Lee, Wen Su, Britni M Arlian, Jia Xie, Richard A Lerner, Hui-Ling Yen, Jesse D Bloom, and Ian A Wilson. Different genetic barriers for resistance to HA stem antibodies in influenza H3 and H1 viruses. *Science*, 368(6497):1335–1340, June 2020.

[181] Nicholas C Wu, Andrew J Thompson, Jia Xie, Chih-Wei Lin, Corwin M Nycholat, Xueyong Zhu, Richard A Lerner, James C Paulson, and Ian A Wilson. A complex epistatic network limits

the mutational reversibility in the influenza hemagglutinin receptor-binding site. *Nat. Commun.*, 9(1):1264, March 2018.

[182] Nicholas C Wu, Andrew J Thompson, Jia Xie, Chih-Wei Lin, Corwin M Nycholat, Xueyong Zhu, Richard A Lerner, James C Paulson, and Ian A Wilson. A complex epistatic network limits the mutational reversibility in the influenza hemagglutinin receptor-binding site. *Nat. Commun.*, 9(1):1264, March 2018.

[183] Nicholas C Wu and Ian A Wilson. Structural biology of influenza hemagglutinin: An amaranthine adventure. *Viruses*, 12(9):1053, September 2020.

[184] Nicholas C Wu, Jia Xie, Tianqing Zheng, Corwin M Nycholat, Geramie Grande, James C Paulson, Richard A Lerner, and Ian A Wilson. Diversity of functionally permissive sequences in the receptor-binding site of influenza hemagglutinin. *Cell Host Microbe*, 21(6):742–753.e8, June 2017.

[185] Nicholas C Wu, Arthur P Young, Laith Q Al-Mawsawi, C Anders Olson, Jun Feng, Hangfei Qi, Shu-Hwa Chen, I-Hsuan Lu, Chung-Yen Lin, Robert G Chin, Harding H Luan, Nguyen Nguyen, Stanley F Nelson, Xinmin Li, Ting-Ting Wu, and Ren Sun. High-throughput profiling of influenza a virus hemagglutinin gene at single-nucleotide resolution. *Sci. Rep.*, 4(1):4942, May 2014.

[186] Rui Xu, Damian C Ekiert, Jens C Krause, Rong Hai, James E Crowe, Jr, and Ian A Wilson. Structural basis of preexisting immunity to the 2009 H1N1 pandemic influenza virus. *Science*, 328(5976):357–360, April 2010.

[187] J W Yewdell, R G Webster, and W U Gerhard. Antigenic variation in three distinct determinants of an influenza type a haemagglutinin molecule. *Nature*, 279(5710):246–248, May 1979.

[188] Timothy C Yu, Caroline Kikawa, Bernadeta Dadonaite, Andrea N Loes, Janet A Englund, and Jesse D Bloom. Pleiotropic mutational effects on function and stability constrain the antigenic evolution of influenza haemagglutinin. *Nat. Ecol. Evol.*, pages 1–15, December 2025.

[189] Timothy C Yu, Zorian Thornton, William W Hannon, William S DeWitt, Caelan E Radford, Frederick Albert Matsen, IV, and Jesse D Bloom. A biophysical model of viral escape from polyclonal antibodies. *Virus Evolution*, 8(2):veac110, September 2022.

[190] Mark Zanin, Pradyumna Baviskar, Robert Webster, and Richard Webby. The interaction between respiratory pathogens and mucus. *Cell Host Microbe*, 19(2):159–168, February 2016.

[191] X J Zhang, W A Baase, B K Shoichet, K P Wilson, and B W Matthews. Enhancement of protein stability by the combination of point mutations in T4 lysozyme is additive. *Protein Eng.*, 8(10):1017–1022, October 1995.

[192] Seth J Zost, Jinhui Dong, Iuliia M Gilchuk, Pavlo Gilchuk, Natalie J Thornburg, Sandhya Bangaru, Nurgun Kose, Jessica A Finn, Robin Bombardi, Cinque Soto, Elaine C Chen, Rachel S Nargi, Rachel E Sutton, Ryan P Irving, Naveenchandra Suryadevara, Jonna B Westover, Robert H Carnahan, Hannah L Turner, Sheng Li, Andrew B Ward, and James E Crowe, Jr. Canonical features of human antibodies recognizing the influenza hemagglutinin trimer interface. *J. Clin. Invest.*, 131(15), August 2021.